ENHANCED GAS SENSING PERFORMANCE INDUCED BY CuO-ZnO HETEROSTRUCTURE TOWARDS NO_2 GAS

BY

LEKGOLO MALESELA MAEBANA

A DISSERTATION SUBMITTED IN PARTIAL FULFILMENT OF THE REQUIREMENTS FOR THE DEGREE OF MASTER OF SCIENCE IN PHYSICS IN THE DEPARTMENT OF PHYSICS, SCHOOL OF PHYSICAL AND MINERALS SCIENCES, FACULTY OF SCIENCE AND AGRICULTURE, UNIVERSITY OF LIMPOPO, SOUTH AFRICA.

SUPERVISOR: PROF D.E MOTAUNG

CO-SUPERVISOR: PROF T.E MOSUANG

JANUARY 2023

DECLARATION

I declare that the dissertation hereby submitted to the University of Limpopo for a Master of Science degree in physics has not been submitted as an exercise for any other university, that is entirely my own research in both design and execution, and that all the material contained therein has been duly recognized.

Maebana L.M  On the 24 day of January 2023

Candidate

ACKNOWLEDGEMENTS

I would like to thank the following for their contribution and support during this research project.

- First, I would like to thank the almighty Lord Jesus Christ for giving me such wonderful ability and strength Furthermore.
- I would like to express my appreciation to my excellent supervisor, Prof. D.E. Motaung for his insights shared, encouragement, and contribution to this research.
- I appreciate Prof. T.E. Mosuang's guidance and his continuous meeting regarding the discussion on the progress of my master's work.
- The support and mentoring from Dr. Z.P. Tshabalala and Dr. R.G. Motsoeneng have been very useful throughout this project, and I am very much thankful.
- Sincere gratitude and special appreciation to my whole family and colleague (Mr. M.S. Mamabolo) for their complete support and discussions throughout.
- I would like to express my gratitude to the National Research Foundation (NRF) for providing me with financial assistance throughout my research and the University of Free State (UFS) for granting access to their equipment, as well as the University of Limpopo (UL).

LIST OF CONFERENCES AND ARTICLES DERIVED FROM THIS DISSERTATION

Conferences contribution

1. Lekgolo Maebana, Zamaswazi Tshabalala, David Motaung, Enhanced Gas Sensing Selectivity Towards Benzene Vapour Using ZnO Based Sensor, FSA 11th Postgraduate Research Day, 06-08 October 2021.

Articles

1. Lekgolo M. Maebana, Zamaswazi P. Tshabalala, Hendrik C. Swart, Nompumelelo Leshabane, Lucas Erasmus, David E. Motaung, Comparison study on ZnO and CuO gas sensing characteristics: Temperature modulated-dual selectivity towards benzene and xylene vapours, **Materials Chemistry and Physics, Volume 297, 1 March 2023, 127352.**https://doi.org/10.1016/j.matchemphys.2023.127352.

2. Low-operational temperature for selective detection of xylene gas using a p-n CuO-ZnO heterostructure-based sensor **(Revised for Publication), Journal of Alloys and Compounds.**

DEDICATIONS

For His fruitful aid in completing this dissertation, I devote this work to God the Lord Jesus Christ and My Mother Gloria Maebana, and Siblings: Mantsha Maebana, Kegaogetswe Maebana, and Phenyo Maebana.

ABSTRACT

The selective detection of gaseous benzene, toluene, ethylbenzene, and xylene (BTEX) is challenging due to their similar molecular structures. In addition, BTEX vapours are extremely hazardous and carcinogenic. Thus, in the current study, n-type ZnO and p-type CuO nanostructures were synthesized utilizing various bases by a simple hydrothermal method. Among the tested sensors, the ZnO-NaOH-based sensor displayed a temperature dual-mode selectivity toward benzene with responses (R_a/R_g) of 2.5 and 24 at 5 and 100 ppm, respectively at 75 °C, and $R_a/R_g \approx 142$ toward xylene vapour at 100 ppm at an operating temperature of 150 °C. While the CuO-based sensors showed a poor response, sensitivity, and selectivity towards tested analytes. Moreover, the ZnO-NaOH based sensor revealed enormous sensitivity of 1.21 ppm^{-1} and a low limit of detection (LoD) of 0.018 ppm (i.e., 18 ppb) toward xylene. The ultra-sensitivity, selectivity, and low LoD of ZnO-NaOH-based sensor toward benzene and xylene are associated with the improved V_O observed in the *in-situ* photoluminescence and electron paramagnetic resonance studies, as well as the x-ray photoelectron spectroscopy analyses. The ZnO-NaOH-based sensor, which was stored for roughly 18 months (547 days), demonstrated reliable repeatability and long-time operation stability for 22 hours of exposure to xylene. The superior sensitivity, stability, and selectivity indicate openly that the strategy of using various bases is a striking method for fabricating a temperature dual-mode selectivity for the detection of benzene and xylene vapours.

Xylene is not just considered detrimental to the environment; it is also hazardous to humans. Herein we report on xylene vapour detection using CuO-ZnO

heterostructures containing various concentrations (0.1-1.0 wt. %) of ZnO, prepared via hydrothermal synthesis. X-ray diffraction, scanning, and transmission electron microscopy, as well as x-ray photoelectron spectroscopy, validated the formation of the CuO-ZnO heterostructure. Gas detection, sensitivity, selectivity and stability tests of nine different gases, namely benzene, toluene, ethylbenzene, xylene, ethanol, methane, SO_2, NO_2, and CO_2 at various operational temperatures were subsequently investigated. It was found that a CuO-ZnO heterostructure with 1.0 wt. % ZnO showed excellent selectivity towards 100 ppm of xylene at 100 °C. The sensor further demonstrated an insignificant cross-sensitivity ($S_{xylene}/S_{toluene}$= 2.7) and ($S_{xylene}/S_{benzene}$ = 8.5) towards toluene and benzene vapour. Additionally, the ultra-low limit of detection of 9.5 ppb and sensitivity of 0.063 ppm^{-1} were observed towards xylene vapour, which indicated that the CuO-ZnO (1.0 wt. %) heterostructure-based sensor can produce sub-ppb-level xylene concentration. The sensor disclosed excellent long-term stability in dry air and 40% relative humidity.

Finally, at room temperature, the CuO-ZnO (0.5 wt. %) based sensor disclosed a superior selectivity towards NO_2. Additionally, concerning other gases, the sensors showed poor responses at room temperature. While at higher temperatures, the sensors showed better selectivity towards xylene. Thus, these findings showed that while the sensors could detect xylene at high temperatures, nonetheless, the room temperature sensitivity of the CuO-ZnO (0.5 wt. %) based sensor towards NO_2 denoted that the sensor could be used for low power consumption. The superior gas sensing characteristics could be ascribed to the creation of p-n heterojunction, the robust chemical affinity, and the catalytic performance of p-type CuO on xylene and NO_2 gases.

TABLE OF CONTENTS

Section **Page**

LIST OF FIGURES

LIST OF TABLES

CHAPTER ONE

1. INTRODUCTION

1.1. OVERVIEW

A gas sensor is a reversible analyser that converts an input chemical quantity into a meaningful analytical signal, from the concentration of specimen components to the analysis of the entire composition. Gas sensors are frequently used in industries and firefighting to expose flammable, toxic, and combustible gases that can harm property and human well-being **[1]**, **[2]**. The semiconductor metal oxides (SMOs) gas sensors have provided a new opportunity to monitor air quality utilizing (e.g., TiO_2, V_2O_5, CuO, ZnO, and SnO_2) as they have a great potential where they intend to depend on the operating temperature that has shown good stability, better response, high sensitivity and cost efficiency **[3]**. The SMOs gas sensors have become more widespread, suggesting a sustainable future in airborne disease monitoring, indoor air surveying and food freshness analysis **[4]**,**[5]**. Because of the expanding population and industrial expansion in cities, the advancement of complimentary performance gas sensors has gotten a lot of attention around the world, many harmful and toxic gases, including combustible carbon dioxide (CO_2), nitrogen oxide (NO_2), ammonia (NH_3), carbon monoxide (CO), nitrogen oxide (NO), methane (CH_4), sulphur dioxide (SO_2), hydrogen sulphide (H_2S), and others, are ignitable. Different wellsprings of air contamination originate from unpredictable natural mixes (VOCs) which include formaldehyde, dichlorobenzene, tetrachloroethylene, butanal, toluene and ethanol **[6]**, **[7]**, **[8]**, **[9]**, **[10]**.

Nitrogen dioxide (NO_2) is a sharp, pink, earthy gas that is produced when a nitrogen-containing fuel is burned. For example, exposure to NO_2 can damage lung tissue and lead to bronchiolitis obliterans (BO), also known as obliterative bronchiolitis, and silo-filler's disease **[11]**, **[12]**, **[13]**. Nitrogen oxides react with the air's volatile organic molecules in the presence of sunlight to form photochemical smog. Nitrogen oxides are partly due to the nitrogen compounds in the fuel but are formed during the combustion process, primarily due to the direct interaction between nitrogen, air, and oxygen in the flame. Nitrogen oxides are naturally produced in other situations, such as microbiological processes in soil and, to a lesser extent, lightning **[14]**. Methane (CH_4) is an essential component of gaseous petrol and is used to generate heat and power all over the world. Even though methane isn't generally regarded as a dangerous gas, a high concentration can cause manifestations such as rapid heart rate, clumsiness, and fatigue **[15]**. Sulphur dioxide (SO_2), which can be emitted directly by volcanoes or ocean showers, is another chemical that has an impact on human health. Sulphur dioxide in the environment can cause neuronal activity in the airways, resulting in a reflex cough, discomfort, and chest tightness **[16]**.

Hydrogen Sulphide (H_2S) is a gas that is frequently discovered during the penetration and fabrication of raw petroleum and flammable gas, as well as in wastewater operation treatment and utility resources and sewers , where long-term exposure to high enough levels of H2S gas to induce unconsciousness, can result in headaches, decreased attention span, and motor functioning. Ammonia (NH_3) is the preferred nitrogen-containing supplement for plant development; nevertheless, exposure to high alkali concentrations in the air promotes rapid consumption of the nose, throat, and

respiratory tract; additionally, it is included in the list of gases that have a destructive impact on the surroundings **[17]**, **[18]**, **[19]**.

Carbon monoxide (CO) and carbon dioxide (CO_2) are the items of combustion responses, such as the burning of coal, wood, and common gas, or the utilizing of present-day combustion motors. Carbon monoxide is regularly the item of fragmented combustion responses whereas when a hydrocarbon is burned in the air, it produces carbon dioxide and water vapour. They both postures a great risk to human well-being the environment; they are exceedingly poisonous and tall presentation can cause deadly harm. Both CO and CO_2 can prevent oxygen from reaching bodily tissues, resulting in convulsions and death **[20-22]**.

1.2. PROBLEM STATEMENT

Since globally the consideration of the Fourth Industrial Revolution (4IR) innovation has evolved, the demand for electricity and fuels is high, and Anglo Coal, Eskom, and Sasol are strained to use more coal, which result in the emission of toxic gases like NO_2, thus contributing to air pollution. The World Health Organization (WHO) and World Bank reports have shown that approximately five million deaths occur yearly. This cost the world economy roughly R70 trillion because of air pollution. And, in South Africa (SA) roughly 20 000 bereavements happen yearly, and result in a cost of R300 million to the economy **[23-24]**. According to the South African Air Quality Regulator (AQR), i.e., Department of Environmental Affairs (DEA), and WHO surplus 80% of residents residing in urban areas are exposed to air quality levels that surpass the WHO limit. As a result, increasing demands for air quality control and concerns about

occupational health and safety regulations by the government have increased the demand for the fabrication of low-cost portable gas sensors **[25-26]**. These affordable sensors will alleviate the current costs paid by DEA to international companies for buying expensive sensors and as well to maintain them. Currently, the DEA spent R 241 million/year to maintain 143 monitoring stations across the country, which serve as National Air Quality Indicators. While about 90 stations are not in operation due to limited maintenance induced by high costs. Furthermore, air pollution across the world has reduced due to the lockdown as indicated in **Figure 1.1 [27]**. Nonetheless, recent reports have shown that long-term exposure to air pollution can contribute to higher numbers of COVID-19 fatalities, thus confirming a clear correlation between COVID-19 deaths with air pollution, notably in the most polluted countries such as India, Italy, SA, etc. **[28]**. Thus, studies have shown that innovative gas sensor technology based been on semiconductor metal oxides (SMO) due to their low cost portability could be the solution to the current problem. Thus, the present project attempts to use SMO, such as CuO-ZnO heterostructure for the detection of NO_2 gas at lower ppm levels.

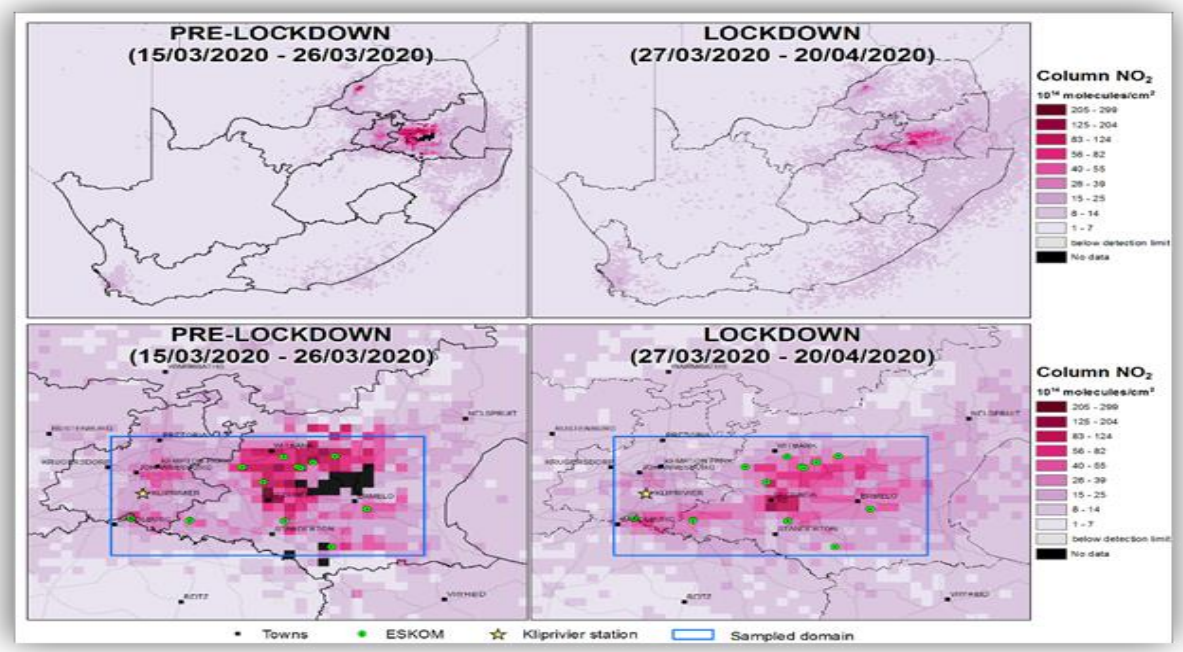

Figure 1.1: Summary of air pollution related to NO_2 during pre-lockdown and lockdown in SA **[27]**.

1.3. AIM AND OBJECTIVES

1.3.1. AIM:

The aim of the study is to fabricate the CuO-ZnO heterostructure-based sensor prototype for detection of low ppm NO_2 gas at low operating temperature.

1.3.2. THE OBJECTIVES ARE AS FOLLOWS

I. Synthesis of the pure ZnO, CuO and CuO – ZnO heterostructure (i.e., 1:1 wt. ratio) using hydrothermal method.

II. Investigate the morphology, structure and optical properties of the materials.

III. Fabricate the gas sensing and test the materials towards NO_2 and xylene in the existence of other gases (e.g., Sulphur dioxide, carbon monoxide, methane, volatile organic compounds (e.g., benzene, toluene, propanol xylene, etc.).

IV. Study the electrical resistivity and gas response mechanism of CuO-ZnO sensors at various operating temperatures and gas concentrations.

V. Study the association between the gas sensing features and magnetic properties.

VI. Study other sensing characteristics (i.e., the long-term stability (> 6 months), the limit of detection, repeatability, and sensitivity) in the presence of different relative humidity levels (10-60%).

1.4. DISSERTATION OUTLINE

Chapter One: This chapter focuses on the overview and the problem statement associated with detection of NO_2 and provides the outline of the chapter.

Chapter Two: This chapter focuses on the literature review around the detection of toxic gases (such as NO_2, xylene, etc.) and the background around the gas sensing.

Chapter Three: This chapter deals with the characterization techniques used to characterize various nanostructures prepared in this work.

Chapter Four: Focuses on the comparison study on ZnO and CuO Gas Sensing Characteristics: temperature modulated-dual selectivity towards benzene and xylene Vapours.

Chapter Five: This chapter deals with the low-operational temperature for selective detection of xylene and NO_2 gases using a p-n CuO-ZnO heterostructure-based sensor.

Chapter Six: The final chapter provides the summary and the future work.

REFERENCES

1. S.M. Kanan, O.M. El-Kadri, I.A. Abu-Yousef, M.C. Kanan Semiconducting metal oxide-based sensors for selective gas pollutant detection Sensors (Basel), 9 (2009), pp. 8158-8196.
2. P.-R. Chung, C.-T. Tzeng, M.-T. Ke, C.-Y. Lee Formaldehyde gas sensors: a review Sensors (Basel), 13 (2013), p. 4468.
3. S.J. Kim, S.J. Choi, J.S. Jang, H.J. Cho, W.T. Koo, H.L. Tuller, I.D. Kim, Exceptional high performance of Pt-based bimetallic catalysts foe exclusive detection of exhaled biomarkers, Adv mater. 29 (2017) 1700737.
4. Yamazoe, N. New Approaches for Improving Semiconductor Gas Sensors. Sens. Actuators, B 1991, 5, 7-19.
5. Yoon, J.-W.; Lee, J.-H. Toward Breath Analysis on a Chip for Disease Diagnosis Using Semiconductors-Based Chemiresistors: Recent Progress and Future Perspectives. Lab Chip 2017, 17, 3537-3557.
6. P. Ivanov, E. Llobet, X. Vilanova, J. Brezmes, J. Hubalek, X. Correig, Response of a Zn2TiO4 Gas Sensor to Propanol at Room Temperature, J.Sens. Actuators B: Chem. 99 (2004) 201–206.
7. G. Neri, Fifty Years of Chemoresistive Gas Sensors, Chemosensors 3 (2015) 1-20.
8. A. Schutze, T. Baur, M. Leidinger, W. Reimringer, R. Jung, T. Conrad, T. Sauerwald, highly sensitive and selective VOC sensor system based on semiconductor gas sensors: How to? Environments 4, 20 (2017) 1-13.
9. S.S. Varghese, S. H. Varghese, S. Swaminathan, K. K. Singh, V. Mittal, Two Dimensional Materials for Sensing: Graphene and Beyond, Electronics 4 (2015) 651-687.

10. V. Palmisano, E. Weidner, L. Boon-Brett, C. Bonato, F. Harskamp, P. Moretto, M.B. Post, R. Burgess, C. Rivkin, W.J. Buttner, Selectivity and resistance to poisons of commercial hydrogen sensors. Int. J. Hyd. Ener. 40 (2015) 11740-11747.
11. Global Burden of Disease project, BBC Science and Environment http://www.bbc.com/news/science-environment-35568249. (13-02-2016).
12. Eco Watch https://www.ecowatch.com. (06-03-2017).
13. G. Neri, Fifty Years of Chemoresistive Gas Sensors, Chemosensors. 3 (2015) 1-20.
14. K. Watchakun, T. Samerjai, N. Tamaekong, C. Liewhiran, C. Siriwong, V. Kruefu, A. Wisitsoraat, A. Tuantranont, and S. Phanichphant, Semiconducting metal oxides as sensor for environmentally hazardous gases, Sen. Act. B. 160 (2011) 580-591.
15. https://www.britannica.com/science/methane.
16. Sulfur Oxides: Sources, Exposures and Health Effects X. Pan, in Encyclopedia of Environmental Health, 2011.
17. Burnett WW, King EG, Grace M, et al. Hydrogen sulfide poisoning: review of 5 years' experience Canad. Med. Assoc. J., 177 (1977), pp. 1277-1280.
18. Glass DCA review of the health effects of hydrogen sulfide exposure Ann. Occup. Hyg, 34 (1990), pp. 323-327.
19. Millea TP, Kucan JO, Smoot EC Anhydrous ammonia injuries J. Burn. Care Rehabil, 10 (1989), pp. 448-453.
20. A. Ruiz, J. Arbiol, A. Cornet, J.R. Morante, Mater. Sci. Eng., C 19 (2002), pp. 105-109.
21. M. Gorguner, M. Akgun, EAJM 42 (2010) pp. 28-35.

22. http://global.britannica.com/EBchecked/topic/279097/hydroxide.
23. N. Yamazoe, J. Fuchigami, M. Kishikawa, T. Seiyama Interactions of tin oxide surface with O_2, H_2O and H_2, Surface Sci., 86 (1979), pp. 335-344.
24. https://www.environment.gov.za/sites/default/files/reports/environmentoutlook_chapter10.pdf (assessed 27-07-2020).
25. http://www.grandviewresearch.com/industry-analysis/gas-sensors-market (accessed 27-07-2020).
26. M. Matooane, R. Diab, Department of Environmental Affairs, Environmental Quality and Protection, Chief Directorate: Air Quality Management and Climate Change, publication series a: book 4 why we need to manage air quality, http://www.airqualitylekgotla.co.za/assets/why_do_we_need_to_manage_air.pdf (accessed 27-07-2020).
27. https://www.csir.co.za/air-pollution-decrease-south-africa-during-national-lockdown (assessed 28-09-2020).
28. https://blogs.worldbank.org/endpovertyinsouthasia/air-pollution-aggravating-covid-19-south-asia (assessed 27-09-2020).

CHAPTER TWO

2.1. LITERATURE REVIEW

After identifying the effects of dangerous gas on human health, gas leak detection tactics became an issue. Prior to the introduction of contemporary electronic sensors, early attempts on finding depended on less precise identifiers. From the early 19th century to the 20th century, coal miners carried canaries into passageways and acted as an early warning system for dangerous gases similarly as methane, carbon monoxide, nitrogen and carbon dioxide **[1]**. In 1815 Humphry Davy invented the "flame safety lamp (or Davy lamp)" to discover the existence of dangerous gas (explosive gas) in underground coal mines. The modern era of gas sensing began with the evolution of catalytic combustion sensors (CFLs) by Dr. Oliver Johnson in 1926-1927, and the introduction of semiconductor metal oxide sensors (SMOs) in the 1990s. In 1990, G. Sberveglieri, G. Faglia, S. Groppelli, P. Nelli, and A. Camanzi validated the first known semiconductor metal oxide gas sensor. Since then, SMO sensors have become essential environmental fuel-oil detectors **[2]**. Semiconductor metal oxide sensors (SMOs) with quick recovery/reaction, flammable, and convey ability can screen and manage harmful, prohibitive affectability, and hazardous gases transmitted from human existence gradually and industry, which has been widely used in open well-being and natural assurance **[3-5]**. Because of its abundant resources, the non-toxicity, good stability, high conductivity, and low cost, ZnO a well-known n-type semiconductor with a wide bandgap of 3.37 eV, has been extensively studied for use in the detection of flammable and hazardous reduction gases.

[6-7].

However, due to the high working temperature **[8-9]**, a massive detection limit **[10-11]**, and delayed response/recovery **[12-13]** of reported ZnO sensing materials, hetero-structures constructed of metal oxides are extra appealing due to the ability to integrate chemical and physical properties. As a p-type metal oxide semiconductor material, CuO has a broad bandgap of 1.2 eV. Because of their non-toxicity, large specific surface area, high stability, and extraordinary electrochemical activity CuO nanoparticles have garnered a lot of attention in gas detection **[14]**. In addition, ZnO is a common n-type semiconductor material and can be combined with CuO, a p-type semiconductor material to form a complex heterostructure material. CuO/ZnO hetero-junction nanostructures can significantly improve the response of gas sensors by utilizing the bonding impact of specific types of nanomaterials and the conductivity modulation impact due to the non-uniform interface **[15]**, and Several research groups have recently reported that ZnO/CuO-NC based gas sensors have excellent gas detection properties for a variety of VOC gases.

2.2. GLOBAL DEMAND FOR GAS SENSORS

The worldwide gas sensor market was worth at US $ 2.19 billion in 2019 and is projected to expand at a compound yearly growth rate (CAGR) of 8.3% from 2020 to 2027 **[16]**. These sensors are equipped with high-sensitivity sensor elements and are expected to be used in processes and manufacturing to detect various types of toxic substances, including nitrogen dioxide and hydrogen sulfide, among others. The use of the world-related health and security rules is becoming mandatory in many countries; this act will have a consequential impact on the demand for gas sensors. Gas sensors are popularly used in respiratory scanning systems, patient scanning

systems, lung function diagnostics ventilation monitoring systems etc., so manufacturers are focusing on proven sensor innovations for more accurate and up-to-date test systems **[17]**.

2.3. CHEMORESISTIVE GAS SENSORS

The chemical resistance sensor is built on sensitive tissue, either in bulk or with the appropriate carrier, where the atomic identification handle is located. The analyte identification process occurs on the surface of the detector or most of the material, resulting in concentration-dependent properties that can be converted into electrical signals using appropriate transducers. Chemically resistant gas sensors are classified into three types: **(a)** micro-machined gas sensors **(b)** planar gas sensors, and **(c)** flexible gas sensors.

Planar gas sensors consist of wide/narrow detection layers deposited on a ceramic substrate using chemical or physical techniques with alternating electrodes **(Figure 2.1: a)**. The sensing layer can also be placed on a plastic foundation, allowing for the development of bendy chemo-resistive gas sensors **(Figure 2.1: b)**. These methods allow micro fabricated chemical resistance sensors to be manufactured on chip substrates, allowing for easy interface with standard silicon microelectronics **(Figure 2.1: c)**.

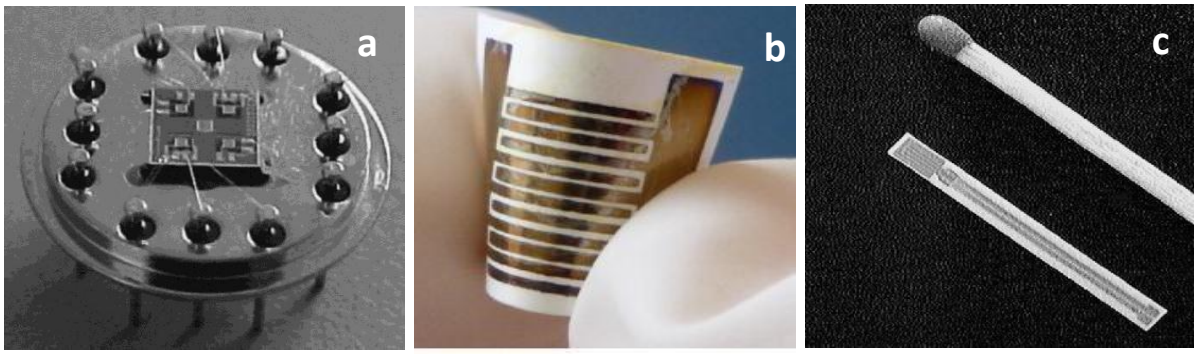

(a) Micro-machined gas sensor **(b)** Flexible gas sensor **(c)** Planar type gas sensor

Figure 2.1: Chemo-resistive gas sensors with different formations **[18]**.

2.4. SEMICONDUCTOR METAL OXIDE GAS SENSORS

Over time, the demand for high performance solid semiconductor metal oxide gas sensors is increasing. Chemical resistant gas sensors were introduced about 50 years ago in the early 1960s. Mr. Seyama demonstrated a gas sensor equipped with a simple electrical device that uses a ZnO thin film as the detection layer **[19]**. He employed a simple chemically resistant gadget based on a thin ZnO membrane that ran at 485 °C. The detector system's sensitivity to propane was approximately 100 times that of the thermal conductivity detector utilized at the time. However, Bratten and Bardeen, two scientists who worked at Bell Labs in the early 1950s, first changed the resistivity depending on the atmosphere in which some semiconductor materials, for example Ge, came into contact **[20]**.

Heiland later explained that metal oxides like ZnO alter the characteristics of semiconductors in response to variations in the partial pressures of oxygen and other gases in the surrounding atmosphere. However, these discoveries were not pursued

further **[21]**. **Figure 2.2** highlights the study findings for semiconductor metal oxides utilized as sensor materials for chemical resistant gas sensors, as well as p-type and n-type oxides.

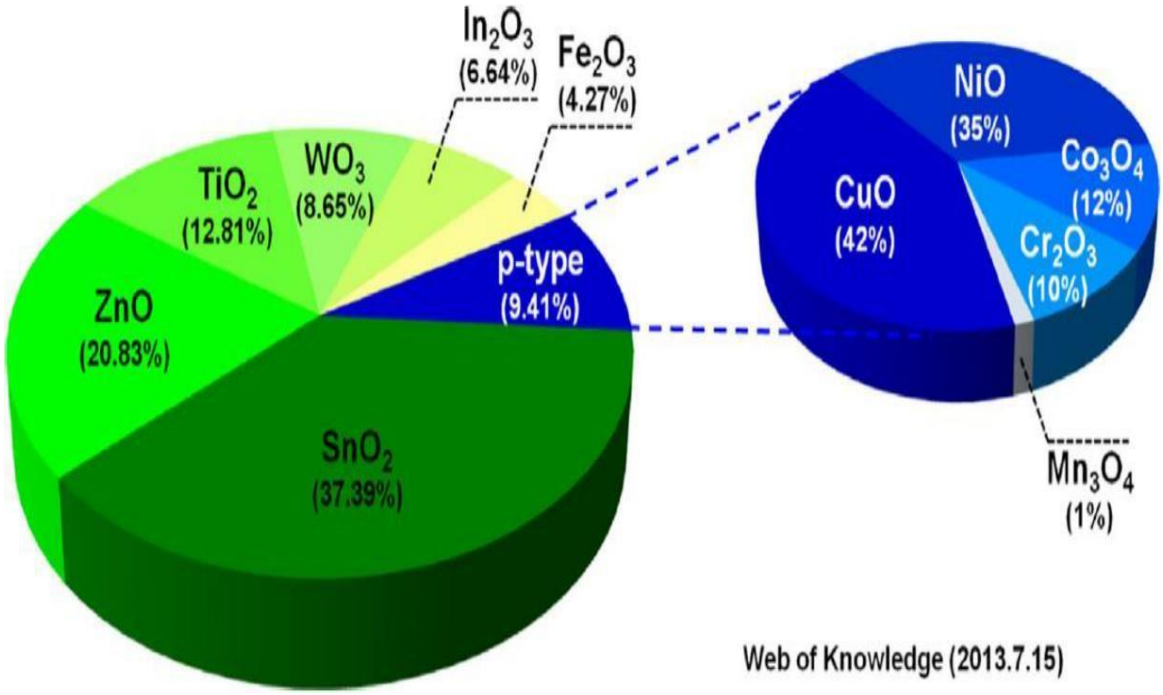

Figure 2.2: Research on p-type and n-type metal oxide-based semiconductor gas sensors (2002-2013) **[22]**.

Because of their numerous fundamental, chemical, and physical features and functions, metal oxides stand out as one of the most familiar, unusual, and potentially most important classes of materials. As illustrated in **Figure 2.2**, SMOs are spitted into n-type and p-type materials, which interact with various types of gases in catalytic chemistry but are not commonly utilized for gas sensing. The most used are n-type metal oxide (SnO_2, ZnO, TiO_2, WO_3, In_2O_3, Fe_2O_3) gas sensing, because the strength of major carries electrons is greater than holes in p-type metal oxide (CuO, NiO, Co_3O_4, Cr_2O_3, Mn_3O_4) gas sensing. ZnO is used also as one of the n-type family due to its higher sensitivity to target gases, as shown in **Figure 2.2**.

Because there is a high demand for the enhanced performance semiconductor metal oxides gas sensors, the following characteristics determine the sensing device's performance: response, selectivity, sensitivity, fast recovery time and response time, stability, low operational temperature, Load of detection (LoD), the lifetime, and reproducibility.

1. A sensor's **response** is explained as the correlation of the transpose in resistance in the air to that of the target gas. When exposed to reducing analyte gas, the detecting resistance of the n-type SMO material lowers, whereas when exposed to an oxidizing gas, the sensor resistance increases **[23]**.

In a reducing gas the response is defined as:

$$\mathrm{R} = \frac{\mathrm{R}_{air}}{\mathrm{R}_{gas}} \qquad \textbf{[24]}$$

And oxidising gas

$$\mathrm{R} = \frac{\mathrm{R}_{gas}}{\mathrm{R}_{air}} \qquad \textbf{[24]}$$

Where R_{air} signifies sensor resistance in the absence of an analyte gas and R_{gas} denotes sensor resistance in the existence of an analyte gas.

2. **Sensitivity** is defined as the lowest concentration of target gas that can be detected. In general, sensitivity is calculated as the ratio of the absolute difference between the device's stabilized resistances. **[25]**.

Where R_a is the value of the initial equilibrium resistance in dry air and R_g is the resistance in the presence of an analyte gas. Furthermore, in some cases, it is also

expressed as the ratio of the resistance on air over the resistance on the gas for reducing gases: the Ra/Rg and resistance on the gas over the resistance in air for oxidizing gases: Rg/Ra **[26]**.

3. **Selectivity** is defined as the sensor's ability to respond to a specific target gas or one specific gas in the presence of other gases **[27]**.

4. The time it takes for a sensor to be exposed to the target gas from the first reaction when the signal reaches 90% of the response limit to the stable end is referred to as the **fast response time**. In addition, the short response time improves the detection characteristics of the gas sensor **[28-31]**.

5. The **fast recovery time** of the sensor is the time it takes to return to its original state after the target gas has been removed **[32-35]**.

6. **Low operational temperature** is the minimum temperature required to warm the sensor and achieve maximum responsiveness **[36]**.

7. **Stability** is the sensor's capacity to withstand changes in phase caused by heat or segregation of dopants, as well as chemical changes caused by poisoning during reactions **[37]**.

8. The **detection limit (LoD)** is defined as the shallow concentration of analyte that the sensor can detect under certain conditions, primarily at a particular temperature. The detection limit, according to the IUPAC definition, is computed as: **[38]**

$$\mathrm{LoD} = 3\left(\mathrm{Noise}_{\mathrm{rms}} / \mathrm{S}\right)$$

[39-40]

Where **S** is the sensitivity (i.e., the slope) and $Noise_{rms}$ points taken when the sensor is exposed to air, i.e., before gas exposure (usually 30 points).

9. The sensor's **lifetime** is the amount of time it will be operating **[41]**.

10. **Reproducibility** is the requirement that all gas detectors provide a steady and reproducible signal **[42]**.

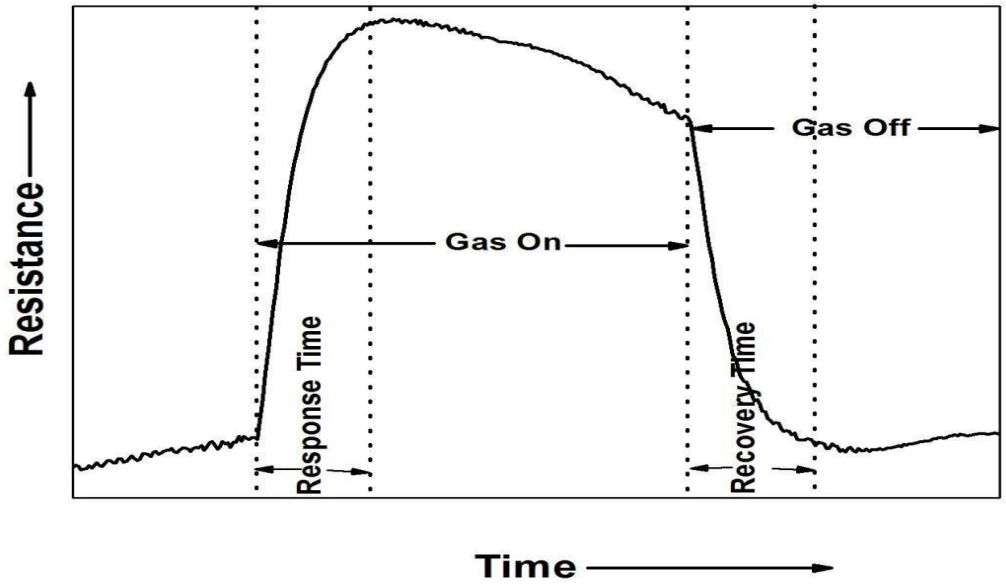

Figure 2.3: Typical resistance of gas sensing a material-time curve **[41]**.

2.5. PROPERTIES OF CuO AND ZnO

The metal copper (II) CuO is the formula for oxide, an inorganic substance. It is a black solid and has two stable copper oxides (Cu_2O or the other is copper (I) oxide) (copper oxide)). Tenorite is an alloy extracted as an outcome of copper mining that serves as a precursor to a variety of copper-based raw materials and compounds. It is a based

gas sensor that has been carefully tested and proven to have various good qualities such as non-toxicity, antibacterial activity, economic availability, and optoelectronic functioning **[43-44]**. It has a relatively narrow bandgap energy of 1.2 - 2.1 eV and typically displays p-type conductivity due to copper vacancies in the lattice and interstitial oxygen used as a gas sensor for the distinguishing of various gases such as Nitrogen dioxide (NO_2), hydrogen gas (H_2), Hydrogen sulphide (H_2S) gas, and Carbon monoxide (CO) etc. **[45-46]**.

Pure copper (II) oxide is more easily made in the laboratory by raising the temperature by either basic copper (II) carbonate, copper (II) hydroxide, or copper (II) nitrate, Copper (II) oxide belongs to the monoclinic crystal system where in an almost square planar arrangement, four oxygen atoms coordinate the copper atom. Copper (II) oxide is used in several wood preservatives and as a ceramic pigment to produce green glazes, blue and red, as well as grey, pink, and black glazes and when welding with copper alloys.

However, because of its low bioactivity, it is wrongly employed as a food supplement in animal feed. In various publications, it has been used as a sensitizer to improve the detection capability of SMO sensors. We found that the sensor is made of $CuOSnO_2$ nanowires, and that CuO functionalization improves the recovery and response time of H_2S detection compared to the bare SnO_2 sensor. Using electrospinning technology and heat treatment to produce $CuO/CuCo_2O_4$ nanotubes with p-p heterojunctions, the $CuO/CuCo_2O_4$ sensor showed an excellent detection capability for n-propanol at the ambient temperature **[47]**. CuO is a functional and affordable material for gas sensors which has two types of habits such: chemical conversion and adsorption-induced surface depletion where they happen by changing the electrical potential which stands as promising and superlative p-type semiconductors, where it is nontoxic and “eco-

friendly" which makes it to be extensively studied in numerous departments **[48]**. The crystal structure of CuO, which is represented in **Figure 2.4**, is found in the monoclinic space group C2/c;A = 4.6837 Å, b = 3.4226 Å, c = 5.1288 Å, and β = 99.54° are the lattice constants.

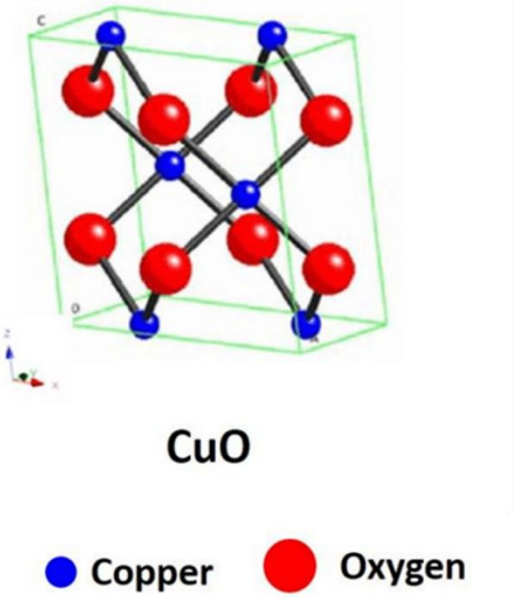

Figure 2.4: Unit cell structure of CuO **[49].**

Among these SMOs, ZnO is a white powder belonging to the IIVI semiconductor group and has a large bandgap of 3.37 eV, making it appropriate for short wavelength optoelectronic applications. This suggests that the native doping of semiconductors is n-type caused by oxygen holes or zinc gaps. The discovery of flammable and dangerous gases has been widely concentrated due to, good transparency, non-harmfulness, high and great security, low cost, high electron mobility/conductivity, strong room-temperature luminescence, and a broad band gap.

However, there are a few drawbacks to the announced ZnO detecting materials, such as a high operating temperature, a large detection limit, and a delayed response/recovery time **[50-51]**. When heated in the air, crystalline zinc oxide turns

yellow, then returns to white when cooled. At high temperatures, a little amount of oxygen is lost to the air, resulting in the creation of non-stoichiometric Zn1+xO at 800 ° C with x = 0.00007 **[52]**. Although zinc oxide is an amphoteric oxide, it will dissolve in most bases, including alkalis, to generate soluble zincates: $ZnO+2NaOH+H_2O \rightarrow Na_2[Zn(OH)_4]$. There are two types of zinc oxide crystals: cubic zincblende and hexagonal wurtzite, but with wurtzite being the most stable structure in ambient circumstances. The centre of zinc and oxide in both cases is a tetrahedron, which is the most frequent form of Zn (II), and the hexagonal structure is 6 mm (Hermann-Mauguin notation) or C6v point group (Schoenflies notation), and the space group is $P6_3mc$ or C_{6v}.

The lattice constants are a = 3.25 Å and c = 5.2 Å, respectively, and their ratio c/a ~1.60 is near to the ideal value for hexagonal cells, c/a = 1.633. The bonding in ZnO is predominantly ionic (Zn^{2+}–O^{2-}), as in other group II-VI materials, with radii of 0.074 nm for Zn^{2+} and 0.140 nm for O^{2-} **[53-55]**. ZnO is a somewhat pale substance with a Mohs firmness of about 4.5. It has lesser elastic constants than other III-V semiconductors, for instance GaN. Ceramics exploit from ZnO's high level of heat capacity and heat conductivity, as well as its high melting temperature and low thermal expansion. At 10 K, the E2 optical phonon in ZnO has a lifespan of 133ps, which is unusually long **[56-58]**. Three major methods produce 105 tons of ZnO per year for industrial use which are indirect process, direct process and wet chemical process. Nanobelts, nanoflowers, nanorods, nanoparticles, nanowires, tetrapods, and other morphologies of ZnO nanostructures can be created from the above-mentioned techniques at specific conditions.

By altering the precursor composition, the morphology of the resultant nanostructures can be altered. (e.g., zinc content and pH values) or heat treatment (e.g., temperature

and heating rate) **[59]**. Early people used zinc compounds as a paint or therapeutic ointment, in both processed and raw forms, but their composition is unknown. Charaka Samhita, Indian medical literature, probably dates back to 500 BC. Prior to BC, it mentions the use of pushpanjan, probably zinc oxide, as an eye and open wound ointment. Greek doctor Dioscrides also mentions a zinc oxide ointment (the 1st century AD). In his Canon of Medicine, Avicenna recommended a remedy for ulcerating tumours with zinc oxide, same as did Galen. It's in baby powder and diaper rash cream, as well as anti-dandruff shampoos, calamine cream, and antibacterial ointments **[60-64]**. Zinc oxide powder has a variety of applications, the most popular of which are given below. In the majority of applications, the oxide's reactivity is exploited as a precursor to other zinc compounds. Zinc oxide has an antibacterial, UV-protection properties, binding, high refractive index and high heat conductivity for material science applications. As a result, it is found in a variety of products and minerals, including fire retardants, ointments, ceramics, plastics, rubber, cement, paints, sealants, glass, adhesives, concrete manufacturing, lubricants, meals, pigments, batteries, and ferrites **[65-67]**.

All octahedral positions are empty, so ZnO has enough positions to accommodate a variety of surfaces. Defects and exogenous impurities **[68]**. On **figure 2.5** shows the hexagonal structure of ZnO. The structure is made up of compound levels with alternating levels. O^{2-} and Zn^{2+} ions are alternately packed in a tetrahedron along the C axis. Its tetrahedral coordination leads to piezoelectricity and pyroelectricity property.

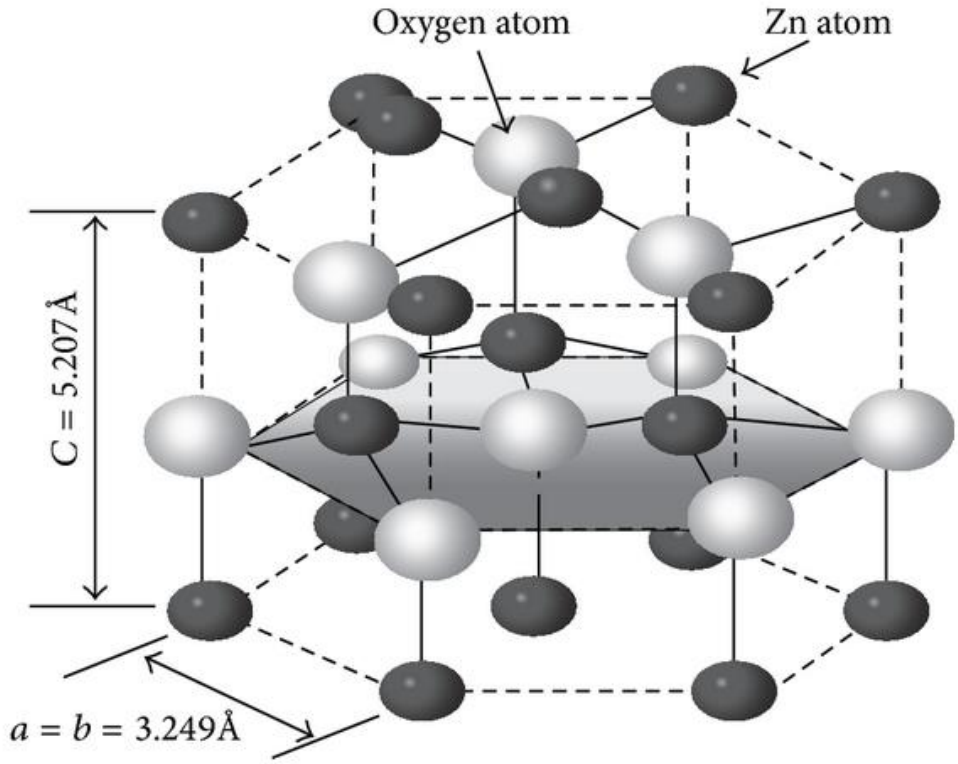

Figure 2.5: ZnO hexagonal wurtzite structure **[69]**.

The structural orientation, amorphous condition, and phase structure of the material may all be determined by examining the XRD pattern. When ZnO nanoparticles are doped with metal oxides/transition metals, In their studies Norton et al. and Gandhi et al. display that ZnO changes from diamagnetic to ferromagnetic habit **[70-71]**, and this has also been predicted theoretically **[72]**. According to Karak et al., the X-ray diffraction patterns of undoped ZnO and ZnO-doped metal/transition metal oxides show an individual form of wurtzite hexagonal structure **[73]**, indicating that the transition metal ions were effectively doped across the ZnO lattice. Under normal pressures, the hexagonal WZ ZnO is seen **[74]**. It is transparent in visible light, and dopants such as (In, Ga, B, and Al) in group III and (Sn, Pb) in group IV have been found to improve its conductivity **[75]**. ZnO is an n-type semiconductor under Zn enrichment conditions **[76]**. Studies have shown that n-type ZnO doping is more

adaptable than p-type doping. The polar surface of ZnO is a significant property, with the common polar surface being the basal plane (0001). Zn^{2+} and O^{2} are two interconnected sub lattices found in the crystal structure of ZnO. Each Zn^{2+} ion is surrounded by a tetrahedron of O2 ions along the c-axis and vice versa. This indicates that one end is partially a zinc lattice site that is positive. Zn-(0001) and the other end are partially negative oxygen lattice sites; O-$(000\bar{1})$ is a partially negative oxygen lattice site. The most common ZnO planes are $(2\bar{1}\bar{1}0)$ and $(01\bar{1}0)$, which are non-polar and have a decreasing energy than the 0001 plane **[77-79]**.

Interstitial and substitutional defects such as O_{Zn} (Oxygen anti-site), Zinc anti-site (Zn_O), Interstitial Oxygen (O_i), and Interstitial Zinc (Z_{ni}) are classified as external-level defects in ZnO nanostructures, and ZnO has many factors that affect thermal conductivity. Number point defect. Because they operate as n-type donors, intrinsic imperfections influence the electrical conductivity of ZnO. When ZnO is doped with a group III element, its electrical resistance decreases. Wang et al. reported on ZnO nanoparticles synthesized by colloidal chemistry that UV radiation increases due to a decrease in oxygen vacancies with increasing crystallite size. When Cu^{2+} ions are doped into ZnO nanoparticles, the crystal structure does not change; instead, the energy band gap increases to 3.93 eV. According to Tong et al., the bandgap of ZnO nanoparticles increases with increasing Mn^{2+} impurity concentration. This is because Mn2+ ions are replaced by Zn^{2+} ions in the ZnO lattice. The thickness of the ZnO thin film has a significant impact on its optical and electrical characteristics and structure **[80-82]**.

Heat treatment enhances the electrical conductivity of ZnO thin films, according to Prasada et al. However, it should be borne in mind that as the temperature increases, the concentration of charge carriers increases and the Debye length decreases.

According to Mizzsei **[83-84]**, temperature affects the material of the semiconductor sensor, which changes the physical properties of the material. Transition metal oxides (TMOs) are solid materials commonly studied in gas sensing applications. Among other sensors recently reported by Gurlo that ZnO, SnO_2, In_2O_3, and WO_3 are the most investigated sensor sets **[85]**. These TMOs have a 3-4 eV broad bandgap and are predicted to be largely inert at ambient temperature.

They are transparent in the visible electromagnetic range from 400 to 700 nm and have outstanding electrical and optical qualities. These are amorphous materials, also known as highly conductive in their amorphous form **[86-88]**. Due to its advantageous features such as a broad bandgap of roughly 3 eV, effective catalysis, and low resistivity, In_2O_3 is being investigated as a possible chemical sensor among semiconductor materials. However crystal defects in the ZnO structure, such as shallow donors or oxygen vacancies, are significant for defining gas detection characteristics because they function as absorption sites for gas molecules and along the surface of ZnO nanostructures **[89-90]**.

2.6. FACTORS AFFECTING SMOS-BASED GAS SENSORS

2.6.1. SHAPE EFFECT AND GRAIN SIZE

By lowering the particle size to nanoscale, the properties of gas sensors form on semiconducting metal oxides (selectivity, sensitivity, stability and response time) can be greatly enhanced. One of the most essential methods for improving gas-sensing properties is to reduce grain size to the nanoscale. Until now, many research efforts are focused on developing small-particle sensing materials, because smaller particles

expose the more surface area, increasing the sensitivity of SMOx. The improvement or deterioration of gas sensor operating qualities may be accompanied by a reduction/expansion in particle size, the grain frontier barriers limit the effect of gas on the sensor's conductivity, allowing for complete control of the detecting mechanism. The depletion layer, which encases each grain or grain chain, is responsible for this state so the small grains agglomerate into huge entities at high temperatures, reducing the material's surface area and catalytic characteristics.

In 2012, Xu et al. suggested a semi-quantitative model to describe the effect of particle size on SMO sensitivity **[91-94]**. The model compares the space charge layer to describe the sensing capabilities of semiconducting metal oxides nanoparticles (L) and the grain size (D). The model predicts that the reaction will be stronger if the particle size is a less than double the space charge layer. In D>>2L, the sensitivity is D unconventional and the entire structure is more sensitive to internal charges than the charges collected from the surface. Since the number of necks exceeds the number of particle junctions, applying $D \geq 2L$ causes the space charge layer region on all sides to each neck to form a conductive narrow, thereby determining the size dependence of gas sensitivity and sensor material. Changes the conductivity of improving gas sensing performance by developing SMO materials with innovative nanostructures and excellent properties **[95-98]**.

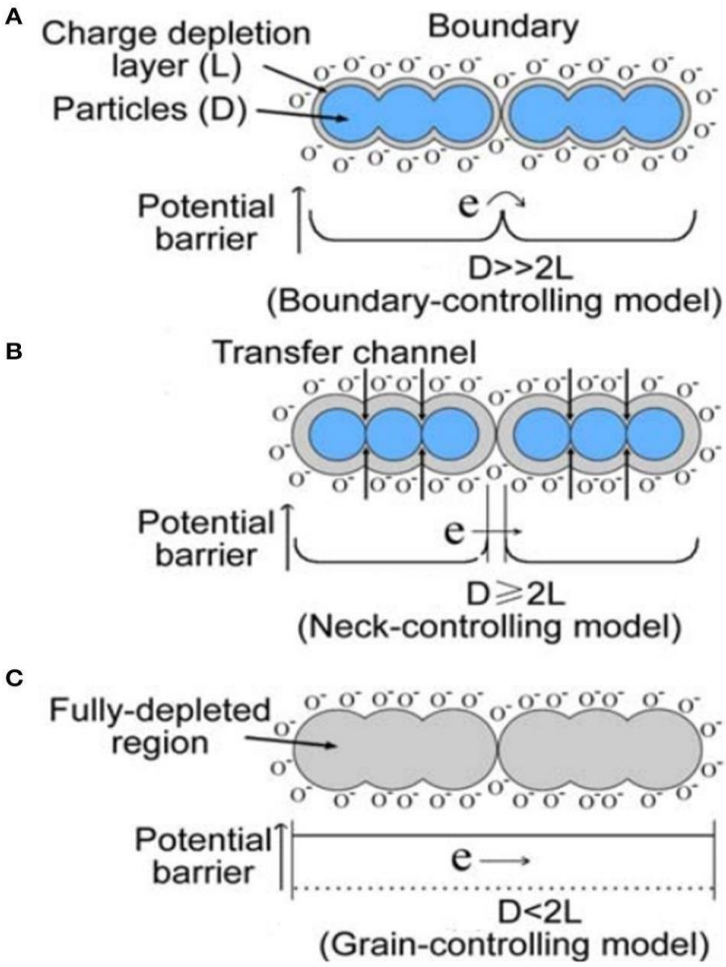

Figure 2.6: The result of crystallite size on the sensitivity of a semiconductor gas analyser based on metal oxide is schematically shown **(A)** D>>2L, **(B)** D≥2L, **(C)** D< 2L **[95]**.

2.6.2. SENSING MECHANISM

Metal oxides are non-stoichiometric, oxygen vacancies are the most obvious defects, and the exchange between the target gas and the oxide surface is reversible, making them very suitable for gas detection. In 1961, Wolkestein first disclosed the sensor mechanism of a metal oxide gas sensor based on the electronic theory of chemisorption and catalysis **[96]**. Morrison (1982), Yamase et al. (1983) and Gopel et al. Later (1995), we established the conditions for charge transport of semiconductors

exposed to the target gas. These ideas can be used to explain the gas detection mechanism of semiconductor metal oxides **[97-99]**.

Based on these ideas, the basic detection process for SMOx-based sensors is the surface interaction between the gas being analysed and sensor material. Semiconductors are divided into two categories: The p-type and the n-type. In n-type semiconductors (ZnO, SnO_2, In_2O_3, and TiO_2), electrons are the primary charge carriers, whereas holes are the primary charge carriers in p-type semiconductors (CuO, TeO_2, BSi_4) **[100]**. When these materials (both p-type and n-type) are exposed to reducing or oxidizing target gases, the resistance changes (increases or decreases), as shown in **Figure 2.7**. The process is guided by the redox reaction, in which reducing gases (CH_4, CO, H_2) provide electrons to metal oxides and oxidative gases (NO_2, O_3, CO_2) absorb them. In the presence of oxygen, electrons from the conduction band are taken from the conduction band to make oxygen ions, resulting in the creation of a depletion layer and an increase in sensor resistance.

The oxygen species adsorbed (ads) are affected by the operation temperature. At temperatures below 150°C, ionized molecular (O^-_2) predominates, while at temperatures above 150°C, atomic species (O^-, O^{2-}) predominate. The presence of this species causes a depletion layer to form, which inhibits electron movement and hence increases resistance. The reactions that produce oxygen ions are as follows **[101-105]**:

$O_2 + e- \rightarrow O_2^- (ads)$ at T<150°C **(101)**

$O_2^- (ads) + e- \rightarrow 2O^- (ads)$ at 150°C<T<450°C **(101)**

$O^- (ads) + e- \rightarrow O^{2-} (ads)$ at T>450°C **(101)**

Oxygen molecules are adsorbed on facets of n-type nanostructures after being exposed to air. As electrons move from the semiconductor powder to the surface, they form an inert barrier on the particle facet, influencing the few oxygen adsorption sites available on the n-type semiconductor surface. In order to conduct, electrons must cross through this surface barrier to proceed from one particle to the next. The extraction of conduction band electrons results in the formation of the adsorbed oxygen ion species (O^{2-}, O_2^- and O^-) and the development of the temperature dependent space charge conduction band. This will increase the resistance of the sensor **[106]**.

When the target gas is injected, it is adsorbed on the surface of the material and, in the case of a reducing gas, it is oxidized, with the electrons being returned to the conduction band. As a result, the width and resistance of the space charge diminish proportionally to the concentration of the object to be analysed. When a gas oxidizes, electrons are removed from the conduction band, causing resistance to climb correspondingly. The presence of reducing gases enhances conductivity in n-type semiconductors, whereas the presence of oxidizing gases decreases conductivity **[107-108]**.

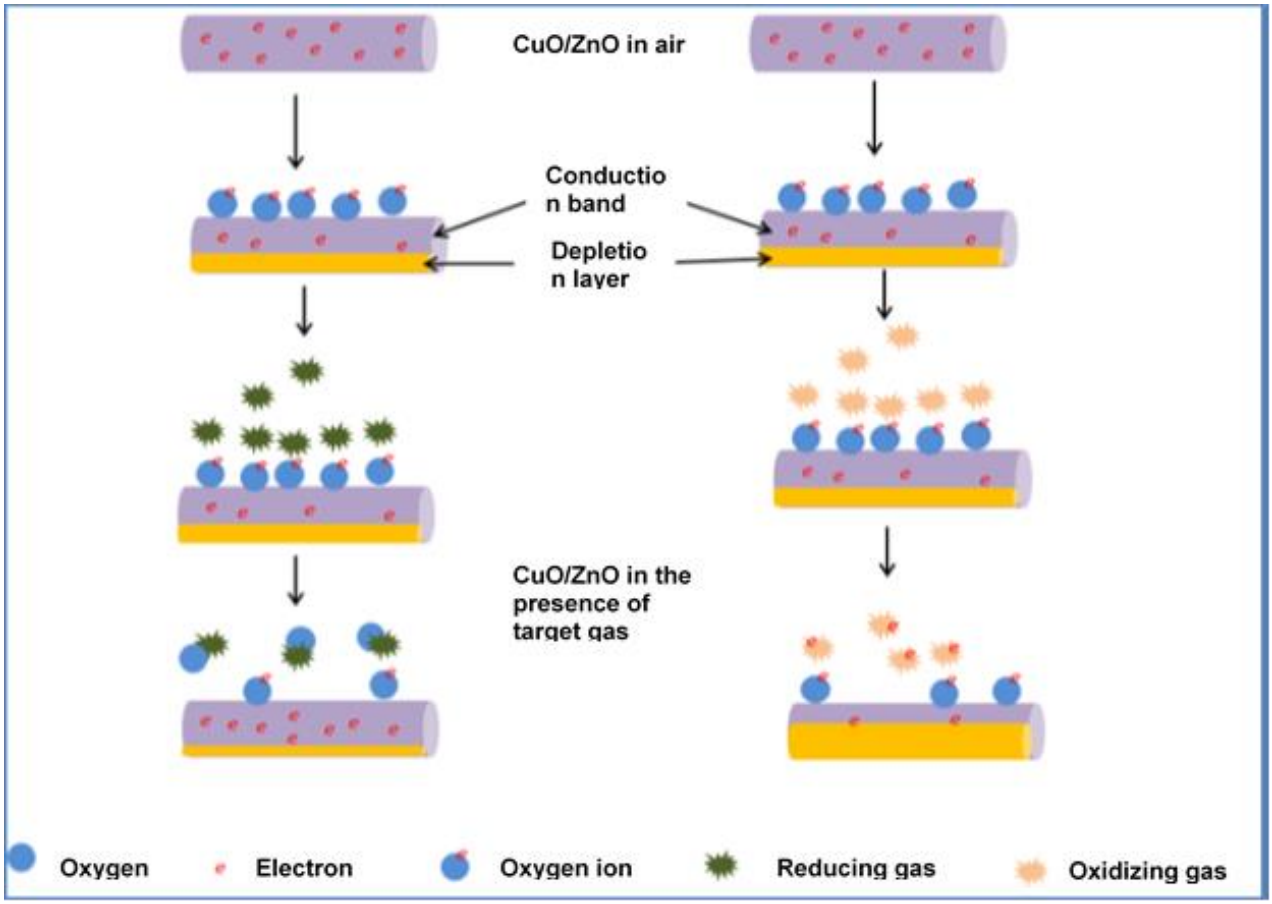

Figure 2.7: The sensing mechanism of a CuO/ZnO sensor when it comes into touch with a reducing or oxidizing target gas is depicted schematically **[101]**.

In contrast to n-type SMOs sensors, the sensing process for p-type semiconductors is the inverse of the n-type SMOs sensors. Assimilation of oxygen molecules on the material surface, accompanied by ionization, results in the formation of a hole accumulation layer on the material surface, which reduces resistance. They transpose in sensor resistance of p- and n-type SMOs gas sensors after exposure to reducing gas as shown in **Figure 2.8 [109]**. When the target molecules are exposed to a reducing environment, they oxidize (react) with the transferred oxygen species on the facet, releasing trapped electrons back into the conduction band and raising sensor resistance as the hole accumulation layer thins. When the target gas oxidizes,

electrons are removed from the conduction band, causing resistance to drop **[110-112]**.

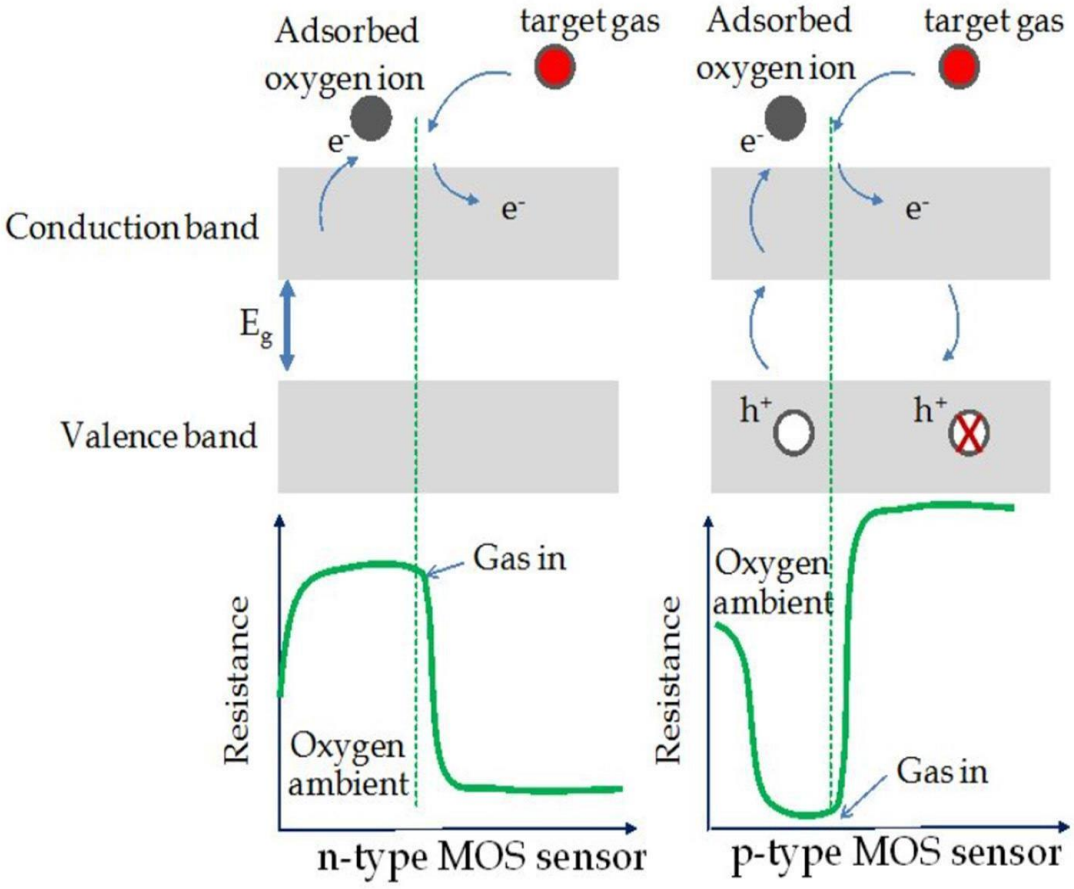

Figure 2.8: The p- and n-SMO sensors' resistance varies when revealed to the aimed gas (reducing gas), as shown in the schematic picture **[109]**.

2.6.3. SELECTIVITY AND STABILITY

Various changes are investigated, such as the development of materials that are sensitive to only one component and have little or no cross-sensitivity to other chemicals that may be present in the work environment, the correct temperature, doping elements, and their concentrations. It has been. Another method relies on the

development of components for separating multiple analytes in a combination. Because it is impossible to do this with just one sensor signal, it has usually done with sensor temperature modulation or sensor arrays **[113-114]**. In practice, however, developing a fully selective metal oxide gas sensor is sometimes impossible, as most materials exhibit cross sensitivity to humidity and other vapours or gases. To address the problem, researchers are focusing their efforts on developing novel gadgets that can address it, Additives can be used to functionalize the metal oxide surface, for example **[115-118]**.

The sensor's stability is highly associated with the device's lifetime, or the amount of time the sensing device is operational. As a result, once the sensor becomes unstable and different out-turns are reported under the same conditions, it can be concluded that the device's lifetime is finished because no further steps will be performed to restore past out-turn characteristics such as resistance baseline or repeatability. The most common reasons of sensor instability in the mid/long term are sensitive layer degradation and irreversible gas detection, both of which shorten device lifetime **[119]**. To be effective, the sensor gadget must produce a consistent and reproducible signal over time. However, previous studies have shown that lowering the afterglow and operating temperature of the sensor material improves stability. It has also been demonstrated that doping metal oxides with mixed oxides or metal particles increases gas sensor stability **[120-122]**.

2.6.4. HUMIDITY AND OPERATING TEMPERATURES

As numerous SMOs humidity-based gas sensors have been created, humidity is an essential component that determines the performance of metal oxide gas sensors. Nonetheless, the detecting process for water vapour and other gases such as NO_2, CO, and H_2S differs. Ionic-type humidity sensors are the most commonly used SMO humidity gas sensors. The conduction process is heavily reliant on H^+ or H_3O^+ derived from adsorbed water dissociation, which transfers between the next hydroxyl groups. The deposited water on the metal oxide surface prevents electron donation to the sensor layer. Furthermore, it reduces the sensitivity of the SMOs sensor for the following reasons: The reaction that happens between the surface oxygen and water molecules causes a drop in the sensor's baseline resistance, resulting in a loss of sensitivity **[123-126]**.

On the facet of a SMOs sensor, three processes occur: desorption, adsorption and oxygen species activity. Because these mechanisms are thermally initiated at low temperatures, the response is generally modest because gas molecules lack the high temperature energy to react with the transferred oxygen species, resulting in a sluggish chemical reaction. As a result, response increases as temperature rises; yet, because the sensor's response is governed by the rate of gas molecule diffusion, the response decreases at high temperatures. The reaction rates of the two processes finally achieve equilibrium at moderate temperatures, and the sensor response reaches its maximum. Researchers discovered that exposing the SMOs sensors with ultraviolet (UV) radiation could reduce the sensors' working temperature. The UV light is used to initiate the chemical processes in the facet without heating the sensors,

which is desirable because it decreases explosion risks and enhances device lifetime **[127-131]**.

2.7. HETERO-JUNCTION P-N TYPES

In 2000, Herbert Kroemer of the University of California, Santa Barbara, California,

USA and Zhores I. Alferov of the Ioffe Institute in Saint Petersburg, Russia shared the Nobel Prize in Physics for "developing semiconductor heterostructures used in high-speed photography and optoelectronics". A heterostructure is an interface formed by two different semiconductor layers or areas. In contrast to a homo-junction, these semiconducting materials exhibit asymmetrical band gaps. The discovery of electronic energy bands benefits many solid-state applications such as transistors, solar cells and semiconductor lasers. The term "heterostructure" refers to a device with multiple heterojunctions, however the two names are frequently used interchangeably. The condition that each material be a semiconductor with unequal band gaps is rather ambiguous, especially at small length scales when electronic properties are impacted by spatial factors **[132]**.

It is common knowledge that semiconductor sensors based on a single SMOx do not give the outstanding overall detection accomplishment in terms of stability, selectivity, and sensitivity. The development of heterostructures between two semiconductors has piqued the interest of researchers as one of many ways to improve the performance of gas sensors. CuO, ZnO and other SMO-based heterojunction components provide excellent gas sensor characteristics. When compared to individual SMOx materials, gas sensors based on the p-n heterojunction structure have a stronger sensor response, a lower operating temperature, and a shorter reaction time. The bending of

the conduction and valence bands, as well as the homogeneity of the Fermi level, are responsible for the p-n junction structure's improved conductivity, response behaviour, and recovery time **[133-136]**.

Various synthesis methods can be used to create hetero-structures such as chemical vapor deposition, sputtering techniques, a flame spray method, electrospinning technique, and the hydrothermal method that has been mostly used method throughout decades **[137-141]**. A p-n junction is an interface or border between two types of semiconductor materials (p-type and n-type) within a single semiconductor crystal. On the "p" (positive) side of an electrically neutral atom's outer shell, there are more holes than electrons. There are more electrons than holes in the "n" (negative) side. This permits current to flow throughout the connection in only one direction. LEDs, solar cells, integrated circuits, Diodes, and transistors all use p-n-heterojunctions as basic "building blocks" of semiconductor materials. Doping, much like ion implantation, to make a p-n-heterojunction, the technique of dopant diffusion, commonly known as epitaxy, is employed (growing a crystalline layer doped with one type of dopant on top of a crystalline layer doped with another type of dopant). The usage of two distinct materials introduces grain boundaries between semiconductors, greatly restricting their utility due to electron and hole dispersion **[142-144]**.

REFERENCES

1. https://en.wikipedia.org/wiki/Gas_detector#History.

2. Sun, Jianhai; Geng, Zhaoxin; Xue, Ning; Liu, Chunxiu; Ma, Tianjun (17 August 2018). "A Mini-System Integrated with Metal-Oxide-Semiconductor Sensor and Micro-Packed Gas Chromatographic Column". Micromachines. 9 (8): pp .408.

3. D.J. Wales, J. Grand, V.P. Ting, R.D. Burke, K.J. Edler, C.R. Bowen, S. Mintova, A.D. Burrows, Gas sensing using porous materials for automotive applications, Chem. Soc. Rev. 44 (2015) pp. 4290–4321.

4. J. Hu, C. Zou, Y.J. Su, M. Li, Y.T. Han, E.S. Kong, Z. Yang, Y.F. Zhang, an ultrasensitive NO2 gas sensor based on a hierarchical Cu2O/CuO mesocrystal nanoflower, J. Mater. Chem. A Mater. Energy Sustain. 6 (2018) pp. 17120–17131.

5. O. Lupan, V. Postica, M. Hoppe, N. Wolff, O. Polonskyi, T. Pauporté, B. Viana, O. Majérus, L. Kienle,F.Faupel,R.Adelung, PdO/PdO2 functionalized ZnO:Pd films for lower operating temperature H2 gas sensing, Nanoscale 10 (2018) pp. 14107–14127.

6. T.S. Wang, Q. Yu, S.F. Zhang, X.Y. Kou, P. Sun, G.Y. Lu, Rational design of 3D inverse opal heterogeneous composite microspheres as excellent visible-light-induced NO2 sensors at room temperature, Nanoscale 10 (2018) pp. 4841–4851.

7. M. Weber, J.H. Kim, J.H. Lee, J.Y. Kim, I. Iatsunskyi, E. Coy, M. Drobek, A. Julbe, M. Bechelany, S.S. Kim, High-performance nanowire hydrogen sensors by exploiting the synergistic effect of Pd nanoparticles and metal-organic framework membranes, ACS Appl. Mater. Interfaces 10 (2018) pp. 34765–34773.

8. D.E. Motaung, G.H. Mhlongo, A.S. Bolokang, B.P. Dhonge, H.C. Swart, S.S. Ray, Improved sensitivity and selectivity of pristine zinc oxide nano structures to H2S gas: Detailed study on the synthesis reaction time, Appl. Surf. Sci. 386 (2016) pp. 210–223.

9. K.D. Diao, M.J. Zhou, J.C. Zhang, Y.J. Tang, S.X. Wang, X.D. Cui, High response to H2S gas with facile synthesized hierarchical ZnO microstructures, Sens. Actuators B Chem. 219 (2015) pp. 30–37.

10. Y.L. Cao, D.Z. Jia, R.Y. Wang, J.M. Luo, Rapid one-step room-temperature solidstate synthesis and formation mechanism of ZnO nanorods as H2S-sensing materials, Iee J. Solidstate Electron Devices 82 (2013) pp. 67–71.

11. J.F. Deng, Q.Y. Fu, W. Luo, X.H. Tong, J.H. Xiong, Y.X. Hu, Z.P. Zheng, Enhanced H2S gas sensing properties of undoped ZnO nanocrystalline films from QDs by low temperature processing, Sens. Actuators B Chem. 224 (2016) pp. 153–158.

12. F. Huber, S. Riegert, M. Madel, K. Thonke, H2S sensing in the ppb regime with zinc oxide nanowires, Sens. Actuators B Chem. 239 (2017) pp. 358–363.

13. J. Demel, A. Zhigunov, I. Jirka, M. Klementova, K. Lang, Facile synthesis of CuO nanosheets via the controlled delamination of layered copper hydroxide acetate, J. Colloid Interface Sci. 452 (2015) pp. 174–179.

14. N. Verma, N. Kumar, Synthesis and biomedical applications of copper oxide nanoparticles: an expanding horizon, ACS Biomater. Sci. Eng. 5 (2019) pp. 1170–1188.

15. J. Zhang, Z. Qin, D. Zeng, C. Xie, Metal-oxide-semiconductor based gas sensors: screening, preparation, and integration, Phys. Chem. Chem. Phys. 19 (2017) pp. 6313.

16. https://www.grandviewresearch.com/industry-analysis/gas-sensors-market.

17. C. Wang, L. Yin, L. Zhang, D. Xiang, R. Gao, Sensors 10 (2010) pp. 2088-2106.

18. X. Wang, W. Liu, J. Liu, F. Wang, J. Kong, S. Qiu, C. He, L. Luan, ACS Appl. Mater. Inter., 4 (2012) pp. 817-825.

19. Seiyama, T.; Kato, A. A new detector for gaseous components using semiconductor thin film. Anal. Chem. 34 (1962) pp. 1502–1503.

20. Brattain, W.H.; Bardeen, J. Surface properties of germanium. Bell Syst. Tech. J. 32 (1952) pp. 1–41.

21. Heiland, G. Zum einfluss von wasserstoff auf die elektrische leitfähigkeit von ZnO-kristallen. Z. Phys. 138 (1954) pp. 459–464.

22. Kim, H.-J.; Lee, J.-H. Highly sensitive and selective gas sensors using p-type oxide semiconductors: Overview. Sens. Actuators B Chem. 192 (2014) pp. 607–627.

23. S.M. Kanan, O.M. El-Kadri, I.A. Abu-Yousef, M.C. Kanan Semiconducting metal oxide based sensors for selective gas pollutant detection Sensors (Basel), 9 (2009) pp. 8158-8196.

24. P.-R. Chung, C.-T. Tzeng, M.-T. Ke, C.-Y. Lee Formaldehyde gas sensors: a review Sensors (Basel), 13 (2013) pp. 4468.

25. S.J. Kim, S.J. Choi, J.S. Jang, H.J. Cho, W.T. Koo, H.L. Tuller, I.D. Kim, Exceptional high performance of Pt-based bimetallic catalysts foe exclusive detection of exhaled biomarkers, Adv mater. 29 (2017) pp. 170-737.

26. Yamazoe, N. New Approaches for Improving Semiconductor Gas Sensors. Sens. Actuators, B 5 (1991) pp. 7-19.

27. Yoon, J.-W.; Lee, J.-H. Toward Breath Analysis on a Chip for Disease Diagnosis Using Semiconductors-Based Chemiresistors: Recent Progress and Future Perspectives. Lab Chip, 17 (2017) pp. 3537-3557.

28. P. Ivanov, E. Llobet, X. Vilanova, J. Brezmes, J. Hubalek, X. Correig, Response of a Zn2TiO4 Gas Sensor to Propanol at Room Temperature, J.Sens. Actuators B: Chem. 99 (2004) pp. 201–206.

29. G. Neri, Fifty Years of Chemoresistive Gas Sensors, Chemosensors 3 (2015) pp. 1-20.

30. A. Schutze, T. Baur, M. Leidinger, W. Reimringer, R. Jung, T. Conrad, T. Sauerwald, highly sensitive and selective VOC sensor system based on semiconductor gas sensors: How to? Environments 4, 20 (2017) pp. 1-13.

31. S.S. Varghese, S. H. Varghese, S. Swaminathan, K. K. Singh, V. Mittal, Two Dimensional Materials for Sensing: Graphene and Beyond, Electronics 4 (2015) pp. 651-687.

32. V. Palmisano, E. Weidner, L. Boon-Brett, C. Bonato, F. Harskamp, P. Moretto, M.B. Post, R. Burgess, C. Rivkin, W.J. Buttner, Selectivity and resistance to poisons of commercial hydrogen sensors. Int. J. Hyd. Ener. 40 (2015) pp. 11740-11747.

33. Global Burden of Disease project, BBC Science and Environment http://www.bbc.com/news/science-environment-35568249. (13-02-2016).

34. Eco Watch https://www.ecowatch.com. (06-03-2017).

35. G. Neri, Fifty Years of Chemoresistive Gas Sensors, Chemosensors. 3 (2015) pp. 1-20.

36. K. Watchakun, T. Samerjai, N. Tamaekong, C. Liewhiran, C. Siriwong, V. Kruefu, A. Wisitsoraat, A. Tuantranont, and S. Phanichphant, Semiconducting metal oxides as sensor for environmentally hazardous gases, Sen. Act. B. 160 (2011) pp. 580-591.

37. https://www.britannica.com/science/methane.

38. Sulfur Oxides: Sources, Exposures and Health Effects X. Pan, in Encyclopedia of Environmental Health, 2011.

39. Burnett WW, King EG, Grace M, et al. Hydrogen sulfide poisoning: review of 5 years' experience Canad. Med. Assoc. J., 177 (1977), pp. 1277-1280.

40. Glass DCA review of the health effects of hydrogen sulfide exposure Ann. Occup. Hyg, 34 (1990), pp. 323-327.

41. Millea TP, Kucan JO, Smoot EC Anhydrous ammonia injuries J. Burn. Care Rehabil, 10 (1989), pp. 448-453.

42. A. Ruiz, J. Arbiol, A. Cornet, J.R. Morante, Mater. Sci. Eng., C 19 (2002) 105-109. M. Gorguner, M. Akgun, EAJM 42 (2010) pp. 28-35.

43. U.T. Nakate, G.H. Lee, R. Ahmad, P. Patil, Y.B. Hahn, Y.T. Yu, E. kyung Suh. Nano-bitter gourd like structured CuO for enhanced hydrogen gas sensor application. Int. J. Hydrogen Energy (2018), pp. 22705-22714.

44. F. Zhang, A. Zhu, Y. Luo, Y. Tian, J. Yang, Y. Qin. CuO nanosheets for sensitive and selective determination of H_2S with high recovery ability. J. Phys. Chem. C., 114 (2010), pp. 19214-19219.

45. R. Molavi, M.H. Sheikhi. Facile wet chemical synthesis of Al doped CuO nano-leaves for carbon monoxide gas sensor applications. Mater. Sci. Semicond. Process. 106 (2020), pp. 104768.

46. P. Rai, S.-H. Jeon, C.-H. Lee, J.-H. Lee, Y.-T. Yu. Functionalization of ZnO nanorods by CuO nanospikes for gas sensor applications. RSC Adv., 4 (2014) pp. 23604-23609.

47. Z.J. Li, Y.Y. Liu, D.F. Guo, J.J. Guo, Y.L. Su Room-temperature synthesis of CuO/reduced graphene oxide nanohybrids for high-performance NO2 gas sensor. Sens Actuators B: Chem., 271 (2018) pp. 306-310.

48. N. Zhang, X.H. Ma, Y.Y. Yin, Y. Chen, C.N. Li, J.Z. Yin, S.P. Ruan Synthesis of CuO-CdS composite nanowires and their ultrasensitive ethanol sensing properties. Inorg. Chem. Front., 6 (2019) pp. 238-247.

49. G.-J. Sun, S.-W. Choi, A. Katoch, P. Wu, S.S. Kim Bi-functional mechanism of H2S detection using CuO–SnO_2 nanowires J. Mater. Chem. C, 1 (2013) pp. 5454.

50. K.T. Alali, Z. Lu, H. Zhang, J. Liu, Q. Liu, R. Li, K. Aljebawi, J. Wang P–p heterojunction CuO/CuCo2O4 nanotubes synthesized via electrospinning technology for detecting n-propanol gas at room temperature.,7 (2017) pp. 1219-1230.

51. J. Selvi, S. Mahalakshmi, V. Parthasarathy, C. Hu, Y.F. Lin, K.L. Tung, R. Anbarasan, A.A. Annie Optical, thermal, mechanical properties and non-isothermal degradation kinetic studies on PVA/CuO nanocomposites Polym. Compos. 40 (2019) pp. 3737-3748.

52. Wiberg E, Holleman AF (2001). Inorganic Chemistry. Elsevier. ISBN 978-0-12-352651-9.

53. Fierro JL (2006). Metal Oxides: Chemistry & Applications. CRC Press. p. 182. ISBN 978-0824723712.

54. Klingshirn CF, Waag A, Hoffmann A, Geurts J (2010). Zinc Oxide: From Fundamental Properties towards Novel Applications. Springer. pp. 9–10. ISBN 978-3-642-10576-0.

55. Rossler U, ed. (1999). Landolt-Bornstein, New Series, Group III. Vol. 17B, 22, 41B. Springer, Heidelberg.

56. Battez AH, González R, Viesca JL, Fernández JE, Fernández JD, Machado A, Chou R, Riba J (2008). "CuO, ZrO2 and ZnO nanoparticles as antiwear additive in oil lubricants". Wear. 265 (3–4): 422–428. doi: 10.1016/j.wear.2007.11.013.

57. Porter F (1991). Zinc Handbook: Properties, Processing, and Use in Design. CRC Press. ISBN 978-0-8247-8340-2.

58. Millot M, Tena-Zaera R, Munoz-Sanjose V, Broto JM, Gonzalez J (2010). "Anharmonic effects in ZnO optical phonons probed by Raman spectroscopy". Applied

Physics Letters. 96 (15): 152103. Bibcode: 2010ApPhL.96o2103M. doi:10.1063/1.3387843.

59. Elen K, Van den Rul H, Hardy A, Van Bael MK, D'Haen J, Peeters R, et al. (February 2009). "Hydrothermal synthesis of ZnO nanorods: a statistical determination of the significant parameters in view of reducing the diameter". Nanotechnology.20(5):055608.Bibcode:2009Nanot.20e5608E.doi:10.1088/0957-4484/20/5/055608. PMID 19417355.

60. Craddock PT (1998). "Zinc in India". 2000 years of zinc and brass. British Museum. p. 27. ISBN 978-0-86159-124-4.

61. Craddock PT (2008). "Mining and Metallurgy, chapter 4". In Oleson JP (Ed.). The Oxford Handbook of Engineering and Technology in the Classical World. Oxford University Press. pp. 111–112. ISBN 978-0-19-518731-1.

62. Harding FJ (2007). Breast Cancer: Cause – Prevention – Cure. Tekline Publishing. p. 83. ISBN 978-0-9554221-0-2.

63. Sanchez-Pescador R, Brown JT, Roberts M, Urdea MS (February 1988). "The nucleotide sequence of the tetracycline resistance determinant tetM from Ureaplasma urealyticum". Nucleic Acids Research. 16 (3): 1216–7. doi:10.1093/nar/16.3.1216. PMC 334766. PMID 3344217.

64. Battez AH, González R, Viesca JL, Fernández JE, Fernández JD, Machado A, Chou R, Riba J (2008). "CuO, ZrO2 and ZnO nanoparticles as antiwear additive in oil lubricants". Wear. 265 (3–4): 422–428. doi: 10.1016/j.wear.2007.11.013.

65. Ambica Dhatu Private Limited. Applications of ZnO. Archived December 19, 2019, at the Wayback Machine Access date January 25, 2009.

66. L. Schmidt-Mende, J.L. MacManus-Driscoll, Mater. Today, 10 (2007) pp. 40-48.

67. https://www.hindawi.com/journals/tswj/2014/925494/.

68. V. Gandhi, R. Ganesan, H. H. A. Syedahamed and M. Thaiyan, “Effect of cobalt dopingon structural, optical, and magnetic properties of ZnO nanoparticles synthesized by coprecipitation method,” Journal of Physical Chemistry C, vol. 118 (2014) pp. 9715–9725.

69. D. P. Norton, M. E. Overberg, S. J. Pearton, K. Pruessner, J. D. Budai, L. A. Boatner,M. F. Chisholm, J. S. Lee, Z. G. Khim, Y. D. Park and R. G. Wilson, “Ferromagnetism in cobalt-implanted ZnO,” Applied Physics Letters, vol. 83 (2003) pp. 5488–5490,.

70. K. Rode, A. Anane, R. Mattana, J.P. Contour, O. Durand and R.L. Bourgeois, “Magnetic semiconductors based on cobalt substituted ZnO,” *Journal of Applied Physics,* vol. 93 (2003) pp. 7676-7678.

71. N. Karak, B. Pal, D. Sarkar and T. K. Kundu, “Grow of Co-doped ZnO nanoparticles by porous alumina assisted sol-gel route: Structural optical and magnetic properties,” Journal of Alloys and Compounds, vol. 647 (2015), pp. 252-258.

72. S. Baruah and J. Dutta, “Hydrothermal growth of ZnO nanostructures,” *Science and Technology of Advanced Materials,* vol. 10 (2009) pp. 013001-0130019.

73. J. Serrano, A. H. Romero, F. J. Manjo´n, R. Lauck, M. Cardona and A. Rubio, “Pressure dependence of the lattice dynamics of ZnO: An ab initio approach,” *Physical Review B,* vol. 69 (2004) pp. 0943061-09430614.

74. J. L. MacManus-Driscoll and L. Schmidt-Mende, “ZnO- nanostructure, defects, and devices,” *Materials today,* vol. 10 (2007) pp. 40-48.

75. S. B. Zhang, S. H. Wei and A. Zunge, “Intrinsic n-type versus p-type doping asymmetry and the defect physics of ZnO,” *Physical Review B,* vol. 63 (2001) pp. 0752051-0752057.

76. H. Kato, M. Sano, K. Miyamoto and T. Yao, “Growth and characterization of Ga-doped ZnO layers on a-plane sapphire substrates grown by molecular beam epitaxy,” *Journal of Crystal Growth,* vol. 237–239 (2002) pp. 538–543.

77. Z. L. Wang, “Zinc oxide nanostructures: growth, properties and applications,” *Journal of Physics: Condensed Matter,* vol. 16 (2004) pp. R829–R858.

78. H. Iwanaga, M. Fujii and S. Takeuchi, “Growth model of tetrapod zinc oxide particles,” *Journal of Crystal Growth,* vol. 134(1993) pp. 275-280.

79. O. Dulub, L. A. Boatner, U. Diebold, “STM study of the geometric and electronic structure of ZnO(0001)-Zn, (000-1)-O, (10-10), and (11-20) surfaces,” *Surface Science,* vol. 519 (2002) pp. 201-217.

80. T. Prasada Rao, M.C. Santhoshkumar, “Effect of thickness on structural, optical and electrical properties of nanostructured ZnO thin films by spray pyrolysis,” *Applied Surface Science,* vol. 225 (2009) pp. 4579–4584.

81. 110. J. Mizsei, “How can sensitive and selective semiconductor gas sensors be made?” Sensors and Actuators B, vol. 23 (1995) pp. 173-176.

82. A. Gurlo, “Nanosensors: Towards morphological control of gas sensing activity. SnO2, In2O3, ZnO and WO3 case studies,” *Nanoscale,* vol. 3 (2011) pp. 154–165.

83. J. Robertson and B. Falabretti, “Electronic Structure of Transparent Conducting Oxides,” in *Department of Engineering, Cambridge University*, UK, Cambridge CB2 1PZ, (2011) pp. 27-50.

84. H. Odaka, S. Iwata, N. Taga, S. Ohnishi, Y. Kaneta, Y. Shigesato, “Electronic Structures and Optical Properties of ZnO, SnO2 and In2O3,” *Japanese Journal of Applied Physics,* vol. 38 (1999) pp. 3453–3458.

85. H. Hosono, “Ionic amorphous oxide semiconductors: Material design, carrier transport, and device application,” *Journal of Non-Crystalline Solids,* vol. 352 (2006) pp. 851–858.

86. P. G. Patil, D. D. Kajale, V. P. Patil, G. E. Patil and G. H. Jain, “synthesis of nanostructured zro2 for gas sensing application,” *International Journal on Smart Sensing and Intelligent Systems,* vol. 5 (2012) pp. 673-684.

87. P. Duy-Thach and C. Gwiy-Sang, “Effects of defects in Ga-doped ZnO nanorods formed by a hydrothermal method,” *Sensors and Actuators B: Chemical,* vol. 187 (2013) pp. 191-197.

88. Z. Tshabalala, D. Motaung, G. Mhlongo, O. Ntwaeaborwa, Sens.Actuators, B, 224 (2016) pp. 841-856.

89. A.Z. Sadek, S. Choopun, W. Wlodarski, S.J. Ippolito, K. Kalantar-zadeh, Sensors J., 7 (2007) pp. 919-924.

90. N. Han, X. Wu, L. Chai, H. Liu, Y. Chen, Sens. Actuators, B, 150 (2010) pp. 230-238.

91. Y.-F. Sun, S.-B. Liu, F.-L. Meng, J.-Y. Liu, Z. Jin, L.-T. Kong, J.-H. Liu, Sensors, 12 (2012) pp. 2610-2631.

92. A. Rothschild, Y. Komem, J.Appl.Sci, 95 (2004) pp. 6374-6380.

93. N.D. Hoa, V. Van Quang, D. Kim, N. Van Hieu, J. Alloys Compd., 549 (2013) pp. 260-268.

94. K.-Y. Choi, J.-S. Park, K.-B. Park, H.J. Kim, H.-D. Park, S.-D. Kim, Sens. Actuators, B, 150 (2010) pp. 65-72.

95. L. You, Y. Sun, J. Ma, Y. Guan, J. Sun, Y. Du, G. Lu, Sens. Actuators, B, 157 (2011) pp. 401-407.

96. M. Ahsan, M. Ahmad, T. Tesfamichael, J. Bell, W. Wlodarski, N. Motta, Sens. Actuators, B, 173 (2012) pp. 789-796.

97. X. Wang, W. Liu, J. Liu, F. Wang, J. Kong, S. Qiu, C. He, L. Luan, ACS Appl. Mater. Inter., 4 (2012) pp. 817-825.

98. W. Göpel, K.D. Schierbaum, Sens. Actuators, B, 26 (1995) pp. 1-12.

99. P. Rai, Y.-S. Kim, H.-M. Song, M.-K. Song, Y.-T. Yu, Sens. Actuators, B, 165 (2012) pp. 133-142.

100. G. Korotcenkov, Mater. Sci. Eng. R, 61 (2008) pp. 1-39.

101. F.F. Wolkenstein, Discuss. Faraday Soc. 31 (1961) pp. 209-218.

102. R.S. Morrison, Sens. Actuators 2 (1982) pp. 329-341.

103. S. Basu, P.K. Basu, Journal of Sensors (2009), doi:10.1155/2009/861968.

104. D. E. Motaung, G. H. Mhlongo, I. Kortidis, S. S. Nkosi, G. F. Malgas, B. W. Mwakikunga, S. Sinha Ray, G. Kiriakidis, Appl. Surf. Sci. 279 (2013) pp. 142-149.

105. Q.R. Deng, X.H. Xia, M.L. Guo, Y. Gao, G. Shao, Mater. Lett. 65 (2011) pp. 2051-2054.

106. S.J. Pearton, D P. Norton, M.P. Ivill, A. F. Hebard, J.M. Zavada, W.M. Chen, I. A. Buyanova, IEEE Transactions on Electron Devices 54(5) (2007) pp. 1040-1048.

107. Romppainen, P. (1997). Electrical Studies on the Response Characteristics of Tin Dioxide-Bases Semiconductor Gas Sensors. Oulu, University of Oulu.

108. Morrison, R. S. (1987). Mechanism of semiconductor gas sensor operation. Sens.Actuat. 11, pp.283–287. doi: 10.1016/0250-6874(87)80007-0.

109. Wei, G., Tang, N., He, K., Hu, X., Li, M., and Li, K. (2020). Gas-sensing performances of metal oxide nanostructures for detecting dissolved gases: a mini review. Front. Chem. 8: pp. 76. doi: 10.3389/fchem.2020.00076.

110. Choopun, S., Hongsith, N., and Wongrat, E. (2012). “Metal-oxide nanowires for gas sensors,” in Nanowires – Recent Advances, ed. X. Peng (London:IntechOpen), pp. 3–24. doi: 10.5772/54385.

111. Kim, H.-J., and Lee, J.-H. (2014). highly sensitive and selective gas sensors using p-type oxide semiconductors: overview. Sens. Actuators B 192, pp. 607–627.doi: 10.1016/j.snb.2013.11.005.

112. Liu, X., Pan, K., Wang, L., Dong, C., Xiao, X., and Wang, Y. (2015).Butane detection: W-doped TiO2 nanoparticles for a butane gas sensor with high sensitivity and fast response/recovery. RSC Adv. 5 pp. 96539–96546.doi: 10.1039/C5RA20886F.

113. Degler, D., Weimar, U., and Barsan, N. (2019). Current understanding of the fundamental mechanisms of doped and loaded semiconducting metal-oxide-based sas sensing materials. ACS Sens. 4 pp. 2228–2249.doi: 10.1021/acssensors.9b00975.

114. S. Chnkraborty, Л. Sen, and H. S. Maiti, Sens. Actuators, B 115, (2006) pp. 610.

115. F. Parrot, I'll. Menini, Л. Marline/, K. Soulantica, A. Maisonnat, and B. Chaudret, Sens. Actuators, B Г18 (2006) pp. 276.

116. P. Hes/. ler, R. lonescu, K. I.lobet, L. I. Reyes,]. M. Smulko, L. B. Kish, and C G. Granqvist, /7n/s. StatusSolidi B 244 (2007) pp. 4331.

117. A. Basebirotto, S. Capone, Л. D'Amico, G. Di Natale, V. Ferragina, G. Ferri, L. Francioso, M. Grassi,

118. N. Ciuerrini, P. Makovati, F. Martinelli, and P. Siciliano, Sens. Actuators, B 130 (2008) pp. 164.

119. F. Tian, Y. Liu, K. Guo, Mater. Sci. Semicond. Process. 21 (2014) pp. 140-145.

120. G. Hong, Q.-H. Wu, J. Ren, C. Wang, W. Zhang, S.-T. Lee Recent progress in organic molecule/graphene interfaces Nano Today, 8 (2013) pp. 388-402.

121. C. Cantalini, M. Pelino, H.T. Sun, M. Faccio, S. Santucci, L. Lozzi, M. Passacantando, Sens. Actuators, B, 35 (1996) pp. 112-118.

122. G. Korotcenkov, B.K. Cho, Sens. Actuators, B, 156 (2011) pp. 527-538.

123. H. Tang, M. Yan, H. Zhang, S. Li, X. Ma, M. Wang, D. Yang, Sens. Actuators, B, 114 (2006) pp. 910-915.

124. 153. H. Wu, K. Kan, L. Wang, G. Zhang, Y. Yang, H. Li, L. Jing, P. Shen, L. Li, K. Shi, Electrospinning of mesoporous p-type In2O3/TiO2 composite nanofibers for enhancing NOx gas sensing properties at room temperature, Cryst. Eng. Comm 16 (2014) pp. 9116-9124.

125. N. Barsan, M. Schweizer-Berberich, W. Göpel, Fresenius J. Anal. Chem., 365 (1999) pp. 287-304.

126. K.J. Choi, H.W. Jang, Sensors, 10 (2010) pp. 4083-4099.

127. V. Shinde, T. Gujar, C. Lokhande, Sens. Actuators, B, 123 (2007) pp. 701-706.

128. K. Aguir, C. Lemire, D.B.B. Lollman, Sens.Actuators, B, 84 (2002) pp. 1-5.

129. S.-W. Fan, A.K. Srivastava, V.P. Dravid, Sens. Actuators, B, 144 (2010) pp. 159-1.

130. E. Comini, G. Faglia, G. Sberveglieri, Sens. Actuators, B, 78 (2001) pp. 73-77.

131. Zhao, T., Qiu, P., Fan, Y., Yang, J., Jiang, W., and Wang, L. (2019). Hierarchical branched mesoporous TiO2-SnO2 nanocomposites with well-defined n–n heterojunctions for highly efficient ethanol sensing. Adv. Sci. 6: 1902008.doi: 10.1002/advs.201902008.

132. Wang, Q., Kou, X., Liu, C., Zhao, L., Lin, T., Liu, T., et al. (2018). Hydrothermal synthesis of hierarchical CoO/SnO2 nanostructures for ethanol gas sensor. J.Colloid Interface Sci. 513 pp. 760–766.

133. Zeng,W., Liu, T., andWang, Z. (2012). Enhanced gas sensing properties by SnO2 nanosphere functionalized TiO2 nanobelts. J. Mater. Chem. 22 pp. 3544–3548.

134. Shanmugasundaram, A., Basak, P., Satyanarayana, L., and Sunkara, M. (2013). Hierarchical SnO/SnO2 nanocomposites: formation of in situ p-n junctions and enhanced H2 sensing. Sens. Actuators B 185 pp. 265–273.

135. Li, L., Zhang, C., and Chen,W. (2015). Fabrication of SnO2-SnO nanocomposites with p-n heterojunctions for low-temperature sensing of NO2 gas. Nanoscale 7 pp. 12133–12142.

136. Yang, Z., Zhang, Z., Liu, K., Yuan, Q., and Dong, B. (2015). Controllable assembly of SnO2 nanocubes onto TiO2 electrospun nanofibers towards humidity sensing applications. J.Mater. Chem. C 3 pp. 6701–6708.

137. Wang, Z., Li, Z., Sun, J., Zhang, H.,Wang, W., Zheng,W., et al. (2010). Improved hydrogen monitoring properties based on p-NiO/n-SnO2 heterojunction composite nanofibers. J. Phys. ChemC 114 pp. 6100–6105.

138. Maziarz,W. (2019). TiO2/SnO2 and TiO2/CuO thin film nano-heterostructures as gas sensors. Appl. Surf. Sci. 480 pp. 362–370.

139. Lyson-Sypien, B., Kusior, A., Rekas, M., Zukrowski, J., and Gajewska, M., Michalow-Mauke, K., et al. (2017). Nanocrystalline TiO2/SnO2 heterostructures for gas sensing. Beilstein J. Nanotechnol. 8 pp. 108–122.

140. Sharma, B., Sharma, A., Joshi, M., and Myung, J.-, h. (2020). Sputtered SnO2/ZnO heterostructures for improved NO2 gas sensing properties. Chemosensors 8 pp. 67.

141. Hook, J. R.; H. E. Hall (2001). Solid State Physics. John Wiley & Sons. ISBN 978-0-471-92805-8.

142. Luque, Antonio; Steven Hegedus (29 March 2011). Handbook of Photovoltaic Science and Engineering. John Wiley & Sons. ISBN 978-0-470-97612-8.

143. Riordan, Michael; Hoddeson, Lillian (1988). Crystal fire: the invention of the transistor and the birth of the information age. USA: W. W. Norton & Company. pp. 88–97. ISBN 978-0-393-31851-7.

144. J. Pike, S. Chan, F. Zhang, X. Wang, J. Hanson, Appl. Catal. A 303 (2006) pp. 273.

CHAPTER THREE

3. MATERIALS, SYNTHESIS AND CHARACTERIZATION

3.1. MATERIALS USED

Copper (II) acetate monohydrate (Cu $(CO_2CH_3)_2$. H_2O), Zinc acetate dihydrate ($Zn(CO_2CH_3)_2$. $2H_2O$), ammonium hydroxide (NH_4OH), sodium hydroxide (NaOH), Urea (CH_4N_2O), and Ethanol purity of 98% were acquired from Sigma Aldrich and utilized without additional ablution.

3.2. SYNTHESIS METHOD OF THE MATERIALS

One of the most essential technologies for high level material processing of nanostructured materials is hydrothermal synthesis, with applications in a variety of sectors such as catalysis, ceramics, biomedicine, electronics, optoelectronics, gas sensing and magnetic data storage. Hydrothermal synthesis is an aqueous chemical reaction that takes place in a fixed vessel at a temperature that increases pressure. This technology is made up of two parts: a polytetrafluoroethylene (PTFE) or Teflon liner and a PPL lined autoclave. The reactor is made up of two parts: a high-quality stainless-steel shell on the exterior and a Teflon liner on the inside. The container is sealed by tightening the lid with a hook wrench while secured to a suitable nozzle. The synthesis of this approach allows for low temperatures ranging from 100 to 220 °C, corresponding to the boiling point and the critical temperature of water, respectively. It is critical to emphasize that hydrothermal processing has several advantages, together with excessive purity (> 99.5 percentage) for sterilisation and chemical homogeneity, tiny particle size (up to 5 nm), single step synthesis, and cheap cost

equipment. Thus, a 4748A, 125 ml autoclave with the PTFE Teflon vessel acquired from Anton Paar will be employed to create different nanostructures in this experiment.

To synthesize the individual CuO, ZnO and CuO-ZnO heterostructure, a simple hydrothermal method will be used. To make the reaction solutions, 3 grams of CuO, 3 grams of ZnO, and a combination of each 3 grams of CuO/ZnO were poured into three separate beakers, then 150ml of distilled water was added and stirred for 1 hour at 70 °C. Three separate beakers holding the solutions were made, each with 0.5 M Sodium hydroxide (NaOH), 0.6 M Ammonium hydroxide (NH_4OH), and 0.3 M Urea (CH_4N_2O) dropwise in each beaker under careful stirring to preserve the pH of 9. After the samples were collected and transferred in to Teflon vessels, then placed in a microwave oven (Anton Paar Multiwave 3000/Perkin Elmer) for 16 hours at 180 °C. After being cooled down to room temperature, the finished products were placed into a centrifuge and washed 10 times with distilled water in an interval of 0-10 minutes, the final products were dried at 80 °C for 15 hours and calcined for 2 hours at 400 °C.

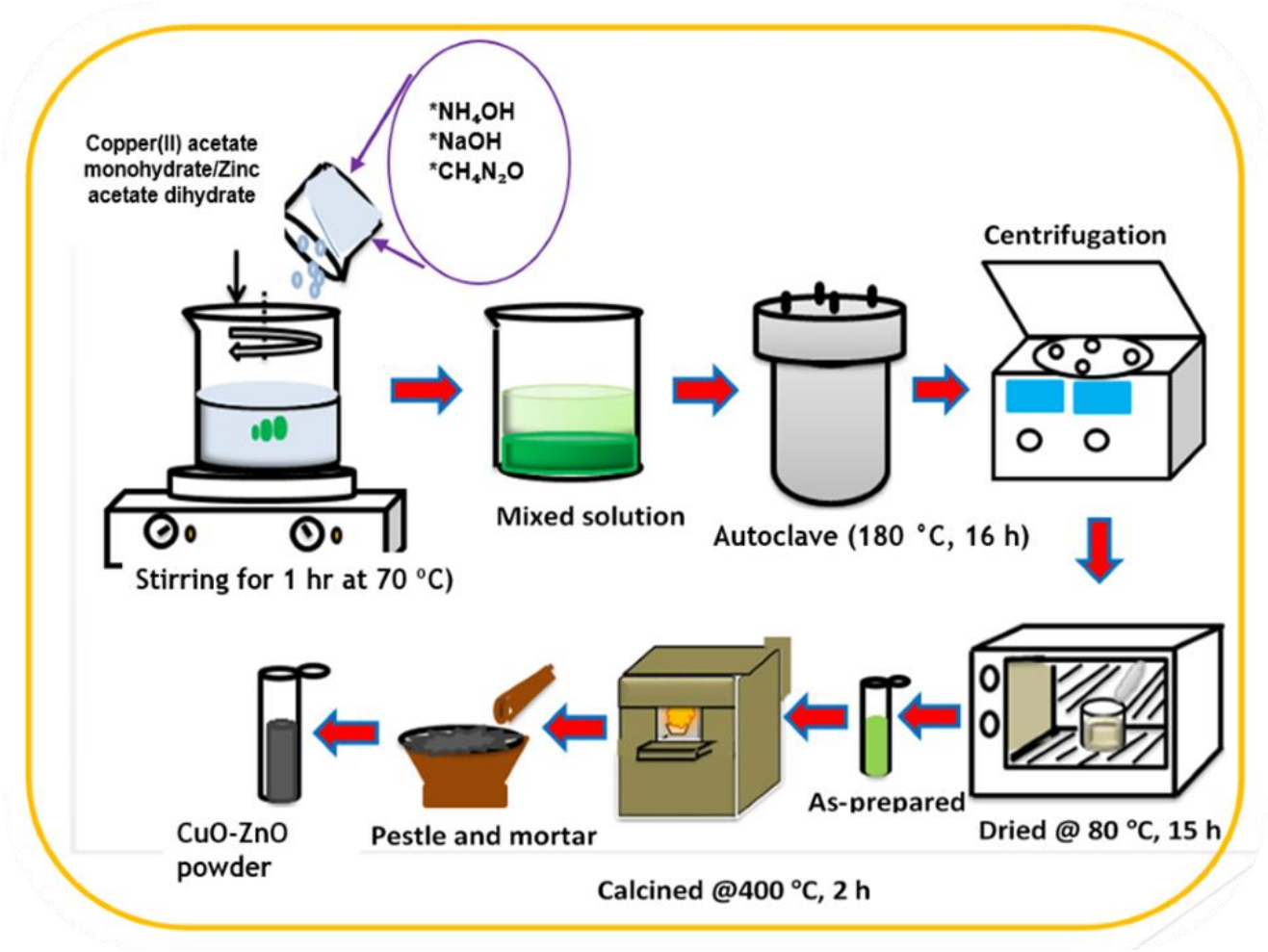

Figure 3.1: The proposed formation of the synthesis process of CuO, ZnO and CuO-ZnO with different base induced by the different form of pH.

3.3. GAS SENSOR FABRICATION AND TESTING OF DEVICES

To fabricate the gas sensing films, an appropriate amount of individual CuO, ZnO and CuO-ZnO heterostructure powder will be placed it in an agate mortar and ground it by adding a terpineol to form slurry or a paste. Then, the paste will be carefully coated onto alumina substrates (size: 0.5 mm × 2 mm) with two Pt electrodes (on its top surface) and a micro-heater (on its bottom surface). The sensor units will be put in a sealed chamber (a KENOSISTEC KSGAS6S Italy gas sensing technology) at a

regulated temperature and under various situations (i.e., in dry air and below corresponding to the damp of 40 and 60%). The resistances of the sensors will be tested to various gas concentrations ranging from parts per billion (ppb) to parts per million (ppm) by switching between the mixture of gases and synthetic dry air. The tested target gases include carbon monoxide (CO), methane (CH4), nitrogen dioxide, ethanol, propanol and BTEX gases, which is benzene, ethylbenzene, toluene and xylene.

3.4. CHARACTERIZATION TECHNIQUES

The structural, internal structure, surface morphology, chemical composition, an optical, paramagnetic properties and surface area of metal oxide semiconductors will be probed using Scanning Electron Microscopy (SEM), Transmission Electron Microscopy (TEM), X-Ray Diffraction (XRD), Photoluminescence (PL), Ultraviolet–Visible Spectroscopy (UV-Vis), Electron Paramagnetic Resonance Spectroscopy (EPRS), Energy Dispersive X-ray Spectroscopy (EDS), and X-Ray Photoelectron Spectroscopy (XPS) techniques. While using the Kinosistec gas testing station to explore the gas detecting properties as a result, the theories and principles underlying the instruments are presented in this chapter.

3.4.1. SCANNING ELECTRON MICROSCOPY (SEM)

The invention of the electron microscope can be traced back to the discovery of electron optics. In the early twentieth century, Bush investigated charged particle trajectories in axisymmetric magnetic and electric fields, revealing that such fields may

operate as particle lenses and emplacing the framework for geometric electron optics. Around the same time, De Broglie, a French physicist, invented the concept of corpuscle waves. Charged particles were assigned a frequency and, as a result, a wavelength: The dawn of wave electron optics. After these two electro-optical discoveries, the concept of electron microscopy began to take shape. In 1942, Zworykin described and built the first genuine SEM, demonstrating how secondary electrons created terrain contrast by positively biasing the accumulator to the sample. His use of photomultiplier tubes as preamplifiers for secondary electron emission currents was one of his most significant contributions. In compared to TEM performance, he achieved a resolution of 50nm, which was still considered low at the time **[1]**.

Oatley began working on a scanning electron microscope based on Zworykin's instrument in 1948. After that, Smith (1956) showed how signal processing might be applied to improve micrographs. He improved the scanning system by using nonlinear signal amplification. He was also the first to correct lens cylindrical faults with a stigmator in a scanning electron microscope. In 1960, Everhart and Thornley enhanced the secondary electron encounter dramatically. A positively biased grid collects electrons, a scintillator converts the electrons into light, and a light guide directs the light to a photomultiplier tube of the same type of detector. Pease and Nixon amalgamated all these advanced designs in 1963 to create SEM V with three magnetic lenses and an Everhart-Thornley detector (ETD). This was the driving force behind the development of the first SEM model in 1965 **[2-3]**.

A field-emitter in an electron gat placed at the apex of a scanning electron microscope's column emits electrons (SEM). Electrons create a cloud that electromagnetic lenses (condenser lenses and objective lenses) use to steer, guide,

and apertures focus and coils. High voltage (5-20 kV) accelerates electrons in a vacuum into a tiny probe that examines the material's surface. Magnetic fields may also be utilized to regulate and shape a beam. When an electron beam interchanges with a material, it loses energy in a variety of ways, each of which conveys details about the sample, as seen in **Figure 3.2**. Resolution is defined as the distance between two elements that can be viewed as independent entities. The ratio of the size of the picture produced to the sample region scanned by the electron beam is known as image magnification. Finding the right magnification but lacking enough resolution will not yield the desired results when running the SEM, and photographs will have no significant information as a consequence. Emission of Fields the scanning electron microscope (SEM) generates a detailed image that may be used to investigate particle size, surface morphology, particle distribution in materials and surface defects **[4-5]**.

Some of the energy is converted to heat, expelled as low-energy secondary electrons, reflected as high-energy backscattered electrons, or radiated as X-rays. The detector converts it into a signal of intensity corresponding to the beam region of the specimen and then directs it to the screen. Furthermore, the x-rays released are specific to the atoms in the sample and are employed in energy dispersive x-ray spectroscopy (EDS). The dispersive x-ray spectroscopy is a useful for obtaining a high-speed qualitative and quantitative analysis of an unknown material, whereas the wavelength dispersive X-ray spectroscopy WDS is useful for obtaining qualitative information and analysing light or trace elements **[5]**.

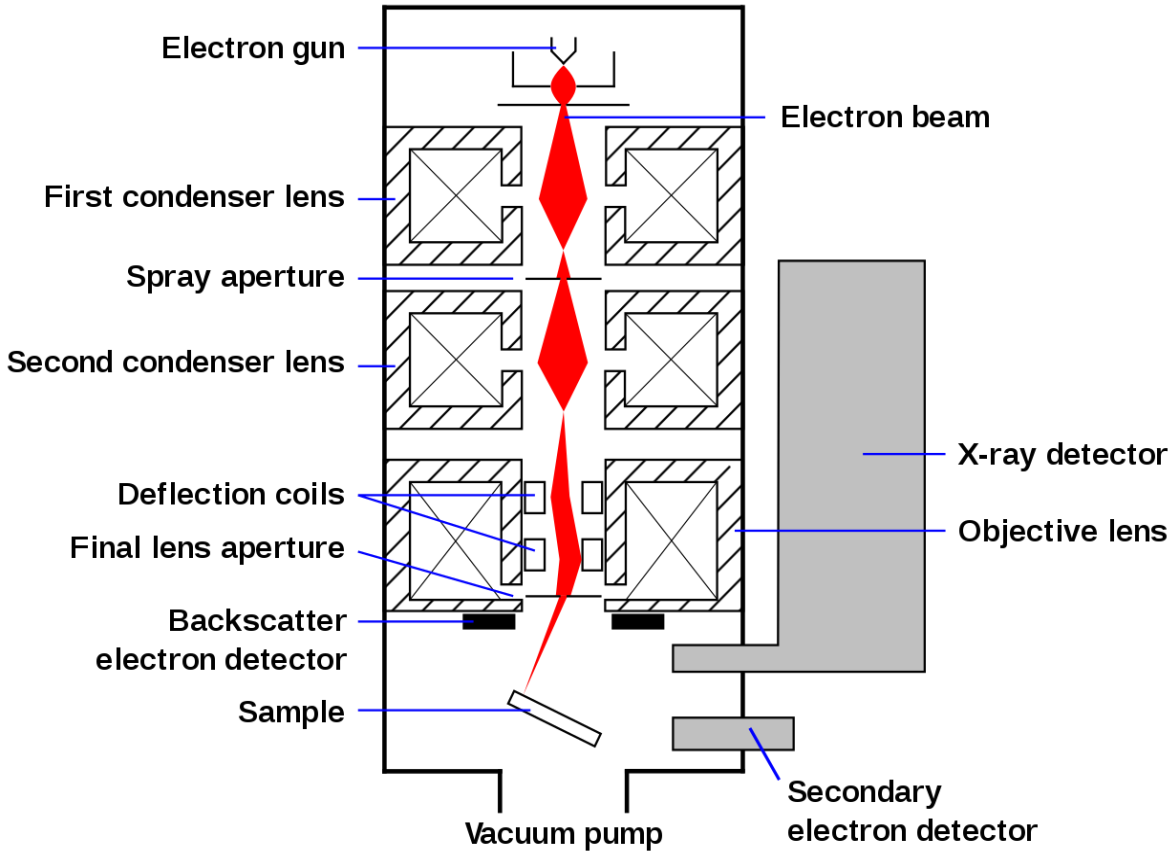

Figure 3.2: Schematic diagram of the SEM **[4]**.

3.4.2. TRANSMISSION ELECTRON MICROSCOPY (TEM)

In 1873 Ernst Abbe argued that the ability to distinguish the details of an object is limited by the wavelength of imaging light, or, in the case of visible light microscopy, several hundred nanometers. Köhler and Rohr pioneered improvements in ultraviolet (UV) microscopes, it resulted in a two-fold increase in resolving power. Because glass absorbs ultraviolet light, expensive quartz optics were required. It was believed that images containing submicron information could not be obtained due to wavelength limitations. Ruska returned to Siemens after World War II and began improving electron microscopes, producing the first microscopes with a magnification of 100k.

Modern microscopes still use the basic structure of this microscope design, which includes multi-stage beam preparation optics **[6-7]**. Transmission electron microscopy (TEM) is an important analytical method in the scientific fields of physics and biology. Characterizing nanomaterials can use them used to provide information about particle size, shape, crystallinity, and the interactions between them. This method differs from SEM in the following ways: Instead of backscattering or knocking out secondary electrons, the primary electron beam passes through the material. An extremely intense beam of electrons is sent through a very thin sample, generally from a tungsten source, and the electrons' interactions with atoms offer information on the crystal structure **[8-9]**.

A general schematic of the TEM is shown in **Figure 3.3**. Essentially, a warm cathode with an electron gun inside emits a distinctly doubled electron through the anode with a power difference of about 1300 kV. The electrons pass through a collecting lens and are directed into a thin, coherent beam that forms a parallel beam before passing through the pattern. Capacitor holes remove excess expected electrons from interacting with the pattern. The target lens amplifies the record of the pattern so that the picture can be found on the screen. In this study, a high-resolution TEM JEOL JEM-2100 setup was used to study the internal morphology of CuO, ZnO, and CuO/ZnO nanostructures at an accelerating voltage of 200 kV **[10]**.

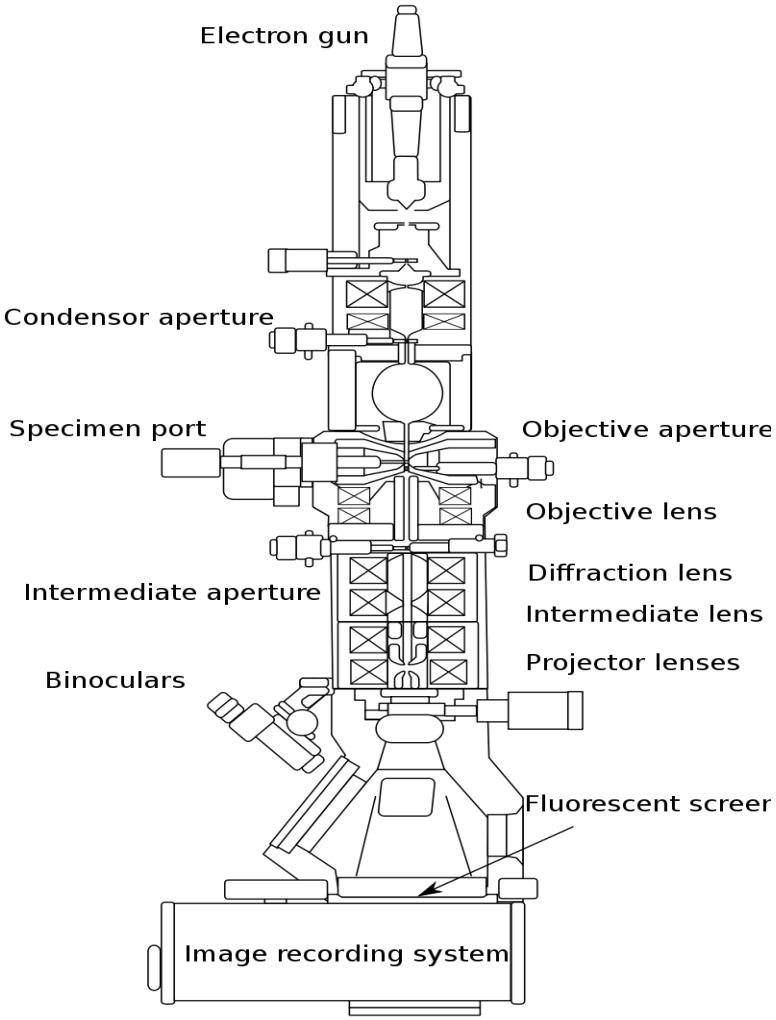

Figure 3.3: A general schematic of the TEM is shown **[10]**.

3.4.3. X-RAY DIFFRACTION (XRD)

On June 8, 1912, at the University of Berlin, a thirty-three-year-old physicist named Max von Laue revealed his discovery of X-ray diffraction in crystals as in a three-dimensional diffraction grating. The non-destructive technique of X-ray diffraction (XRD) is used to characterize crystalline materials. Average grain size, crystallinity, strain, and crystal defects are among the preferred crystal orientations (texture), structures, phases, and other structural factors discussed. X-ray diffraction peaks are

formed due to constructive interference of monochromatic X-ray beams scattered at specific angles in each pair of grating planes in the specimen. The distribution of atoms inside the lattice governs peak intensities. The incident x-ray beam on a substance is the basis for this technique, as shown in **Figure 3.4 [11]**.

When a monochromatic X-ray beam of wavelength (λ) is stipulate obliquely in a crystal with a set of planes (hkl), if the phases of the reflected waves are the same, the reflected waves of the beam are amplified to form constructive interference, and constructive interference fabricates X-ray diffraction peaks. The diffraction peaks should be formed in line with Bragg's criteria.

$$n\lambda=2dsin\theta \quad \textbf{[12]}$$

Where θ is the angle of incidence, λ is the approaching X-ray Cu Kα (λ = 1.5418 Å), n = 1, and d is the interplanar distance of the crystal. Bragg's condition satisfies angle variations and polycrystalline material interplanar spacing.

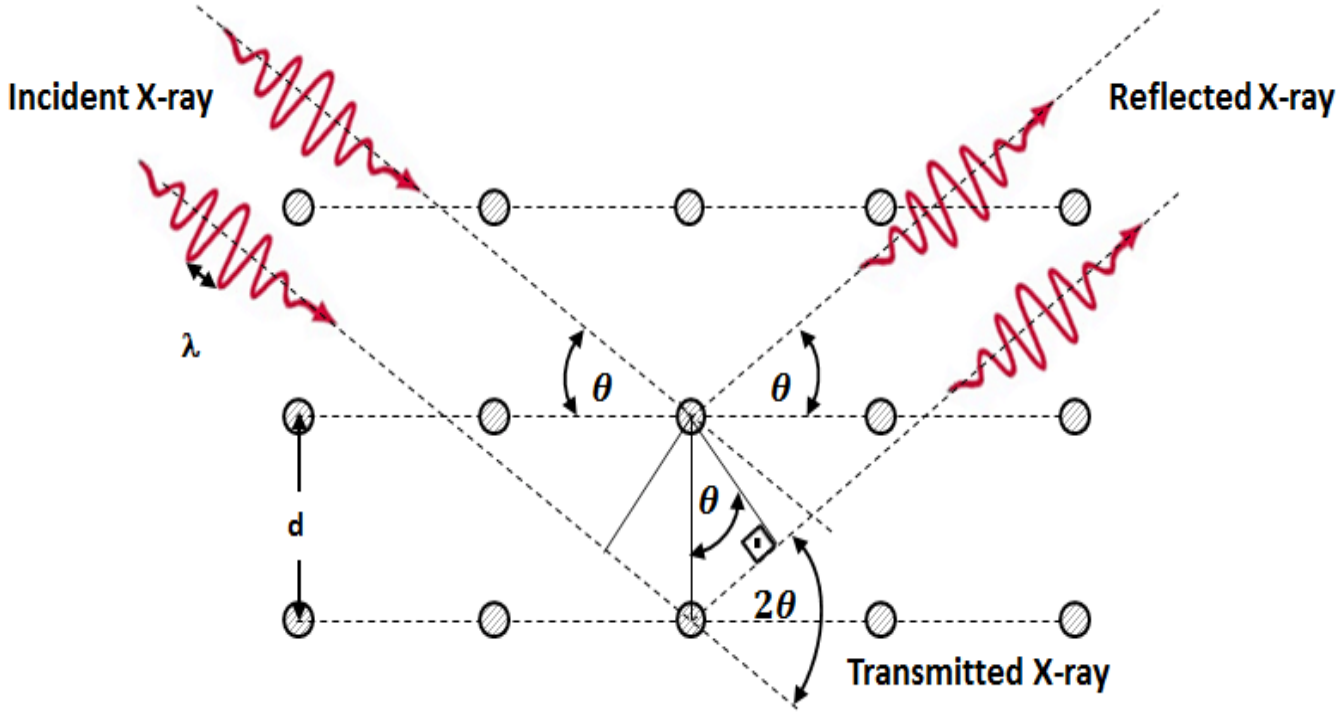

Figure 3.4: Based on Bragg's law, a schematic diagram of a diffraction pattern is shown **[12]**.

The width and intensity of a given peak in its complete width at half maximal (***B***, measured in radians) helps determine the crystallite size (L) using the Debye-Scherrer prototype displayed in the mathematical statement below by observing the diffraction pattern **[13]**.

$$L = \frac{K\lambda}{\beta Cos\theta}$$

Where K=0.94 is the crystallite form factor

The Williamson Hall plot is another proposed model that explains the strain (ε) caused by crystal defects and lattice strain. It is based on the mathematical statement:

$$\beta(hkl)Cos\theta = \frac{K\lambda}{L} + 4\varepsilon\, tan\theta \qquad \textbf{[13]}$$

A PanAlytical X'pert PRO PW3040/60 X-ray diffractometer equipped with a Cu K monochromated radiation source was utilized in this investigation to analyse the produced CuO-ZnO powders. As shown in **Figure 3.5**, the detector is mounted on the rim of a ring that rotates around an axis and is centred on the specimen stage. X-rays deviate from the source of the X-ray tube and refract in the sample before reaching the detector, creating a diffracted beam that converges at a slit.

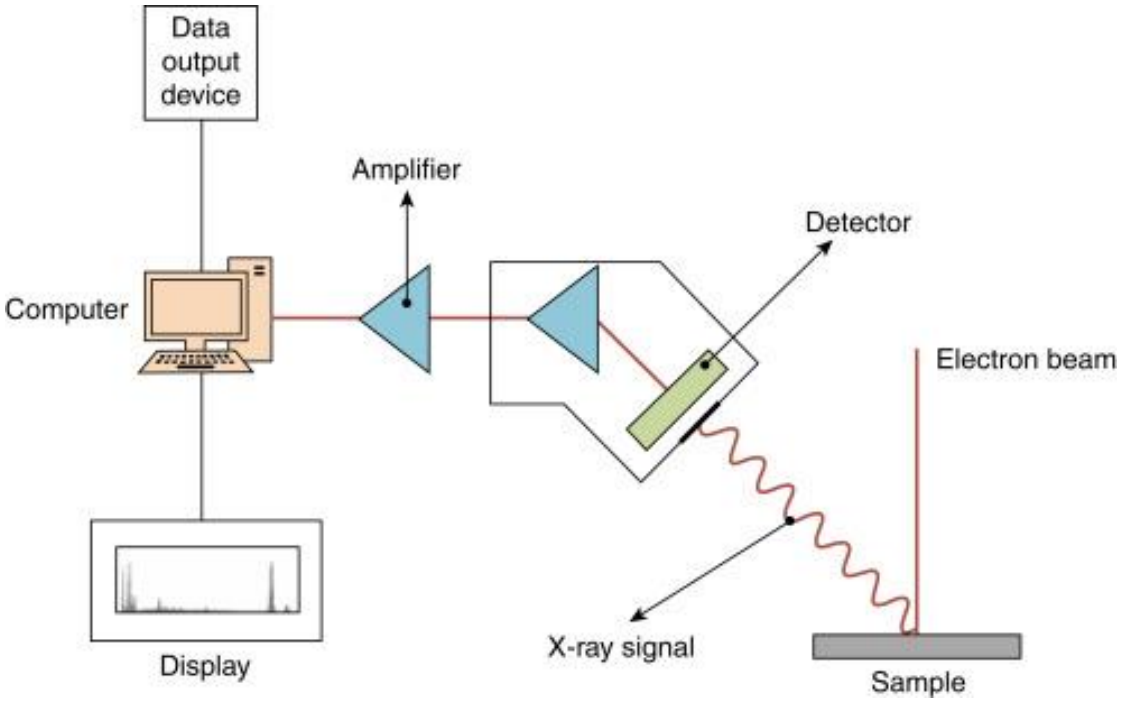

Figure 3.5: X-ray spectrometer schematic diagram **[14]**.

3.4.4. PHOTOLUMINESCENCE SPECTROSCOPY (PL)

PL is a non-destructive characterization method used to study photoexcitation and optical transitions in the electron arrangement of materials. A process known as photoexcitation absorbs the light rays that hit the sample and transfers additional energy to the substance. As a result of photo-excitation, electrons within a substance

change into acceptable exhilarated states. Excess energy is squandered when these electrons remit to their base state, which may or may not involve light emission (radiative procedure) (non-radiative procedure). The sample can release overabundance energy in the form of light, or luminescence, which is known as photoluminescence and is commonly distinguish in III-V semiconductors **[14-15]**.

In semiconductor materials, if the incident photon's energy is comparable to or massive than the energy band gap, it will exhilarate a valence band electron, which will then migrate into the conduction band. Radiation will recombine from the exhilarated state to the base state. Absorption occurs when electrons are excited from the energy level of a neutral acceptor to a higher energy level, and may move from the valence band to the energy level of an ionizing donor or from a valence band to the energy of an ionizing acceptor. This phenomenon helps to explain the imperfections of semiconductor energy bands **[16]**. In this study, PL studies were performed at room temperature triggering at 325 nm using a Horiba Jobin-Yvon iHR 320 NanoLog spectrometer equipped with a Symphony® cryogenic detector and a xenon lamp as a continuous power source. **Figure 3.6** depicts the schematic diagram of the PL spectrophotometer.

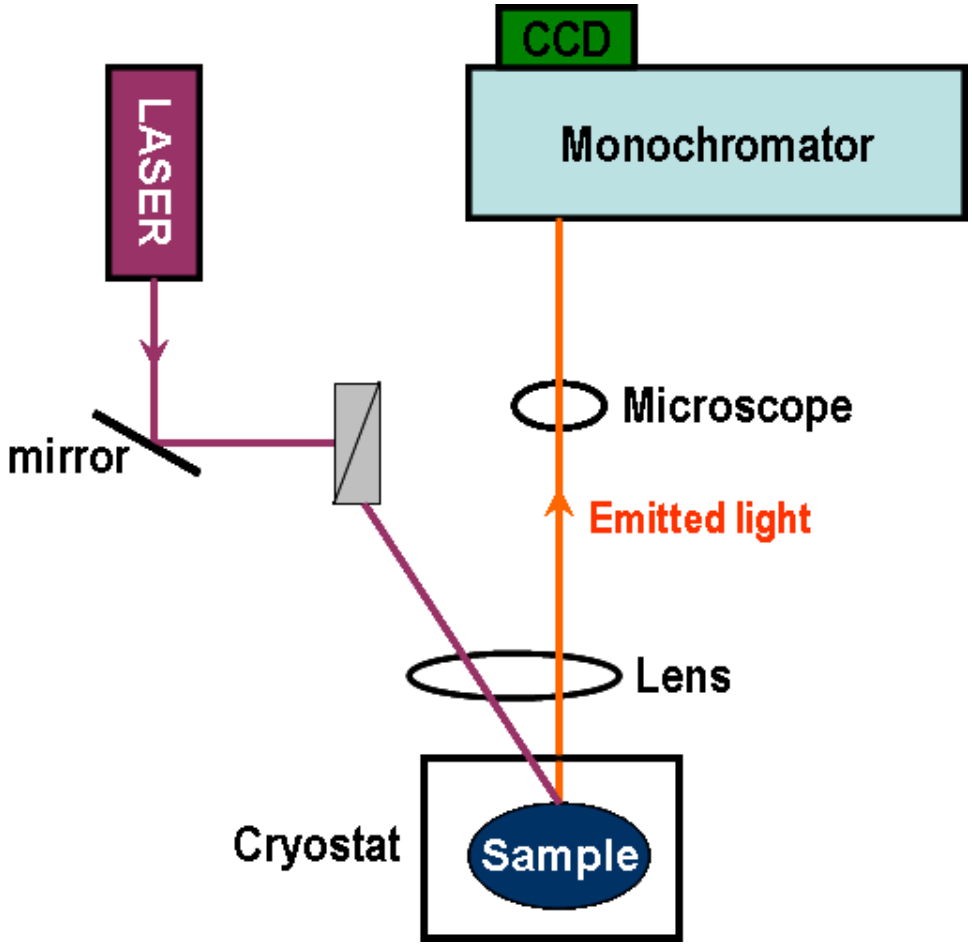

Figure 3.6: A typical PL arrangement is depicted schematically **[16]**.

3.4.5. ULTRAVIOLET-VISIBLE SPECTROSCOPY (UV-VIS)

During WWII, the American government promoted the development and commercialization of UV-Vis spectrophotometers to assist in monitoring the amount of vitamins in troops' meal rations. In 1940, the first UV-visible devices were profitably available. By the 41st year of the 20th century, the Beckman ultraviolet-visible spectrophotometry offered analytical findings in minutes, making it more agile than competitors do. Many advancements have occurred since then in the history of ultraviolet-visible spectrophotometry **[17-19]**. Subsequent decades saw a large-scale

manufacture of UV-visible devices, resulting in their ultimate value decrease. The Bausch & Lomb SPECTRONIC 20 ultraviolet-visible spectrophotometry, introduced in the 53rd year of the 20th century, was the first mass-produced spectrophotometer. The creation of a dual-beam spectrophotometer has reduced analysis time from minutes to seconds. Commercially introduced by Applied Physics Corporation in 1954, Cary 14 provides speed and simplicity for simultaneous sample and solvent evaluation, following years saw significant advancements in UV-Vis devices **[20]**.

Computers were quickly able to manage UV-Vis spectrophotometers after the widespread use of personal computers (PCs) in the 1980s.Through external applications and onscreen displays, the PC assisted in storage configuration. UV-Vis devices became smaller as fibre optics became more popular. With the advent of the new century, devices have become even more optimized. The volume is smaller, less stray and noise and xenon lights are used, which reduces warm-up time and extends bulb life. Similarly, research and discoveries in the early 20th century have made it possible to measure proteins and nucleic acids using UV-VIS devices **[21-22]**.

UV-vis spectroscopy is used to determine the sample's transmittance, reflectance, and absorption. When electromagnetic energy of various wavelengths (near UV and near IR) is ideally irradiated on to the sample, an UV-visible spectrum can be obtained. As a result, monochromatic radiation is used at the same time. The spectrum compares the amount of energy absorbed at each wavelength to the wavelength. The two basic factors used to characterize the UV spectra of substances are the position of the maximum of the absorption band termed -max and the intensity of the bands. The sample is then illuminated with light of an ultraviolet wavelength. The gadget measures both the wavelength and the quantity of light absorbed at each wavelength. The final

spectrum depicts an absorbance vs. wavelength curve. The absorbance may be used to calculate the concentration of a material in a solution using Lambert Bert's law **[23]**.

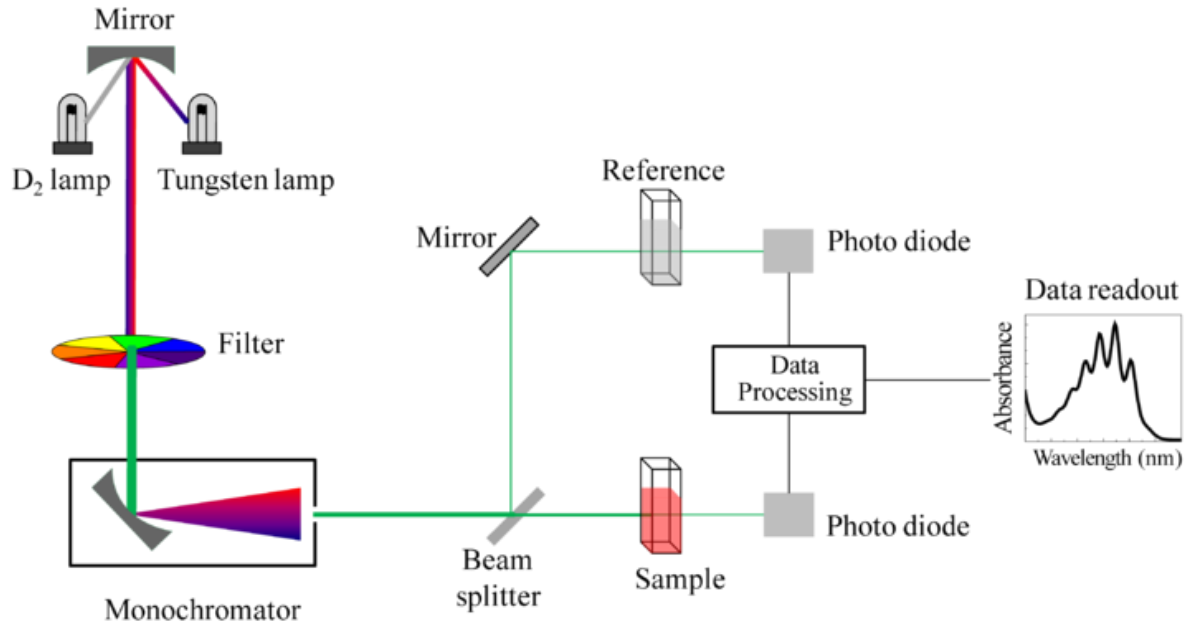

Figure 3.7: The schematic diagram of UV-visible spectrophotometer (UV-vis) **[18]**.

3.4.6. ELECTRON PARAMAGNETIC RESONANCE SPECTROSCOPY (EPRS)

In 1944, the Russian physicist Zawoyski demonstrated a technique called electron paramagnetic resonance spectroscopy (EPR) that predicated on the changes between quantized positions of the displacing magnetic moment. Electron Paramagnetic Resonance Spectroscopy that is conjointly called Electron Spin Resonance (ESR), the methodology is to examine the ions, atoms, or molecules containing singular electrons in gas phases, solid, or liquid, and electron-conducting systems such as metals and semiconductors and point defects in solids **[24, 25]**.

The first derivative of their absorption spectra is used to calculate electron paramagnetic resonance (EPR) spectra. When a compound or molecule has a singular electron, its spin can be in a pair of dissimilar position ms= ±1/2. The configuration can be equidistant to the magnetic field correlating to a decreased energy position ms= -1/2 or opposite to the orientation of the enforced magnetic domain correlating to the increased energy position ms= +1/2. The two energy directions are dissimilar, and this energy dissimilarity eliminates the degeneracy of the electron spin positions. Energy dissimilarity is computed as follows:

$$\Delta \mathrm{E} = E_+ - E_- = hv = g_s \mu_B B \qquad \text{Replace} \quad \mu_B = \frac{\mathrm{eh}}{2mc} \qquad \textbf{[26]}$$

B is the magnetic field strength where it is measured in Tesla $kg{\cdot}s^{-2}{\cdot}A^{-1}$, μ_B is the Bohr magneton 9.2740 x 10^{-24} $kg{\cdot}m^2{\cdot}s^{-2}{\cdot}T^{-1}$, g_s is the electron spin g-factor, *v* is the frequency of radiation, and whilst the *h* Planck constant is equivalent to 6.6260 x 10^{-34} $m^2{\cdot}kg{\cdot}s^{-1}$ **[27]**.

The Nano sample is displayed to microwave radiation while being held in a direct magnetic field to conduct electron paramagnetic resonance (EPR) measurements, which agitates electrons in the uppermost filled molecular orbital to the minimal unfilled molecular orbital. Individual electrons arrange themselves equidistant to the applied magnetic field because of the weak magnetic field. At a given magnetic field strength, microwave irradiation changes the orientation of a few individual electrons, separating the energy positions as shown in the diagram below.

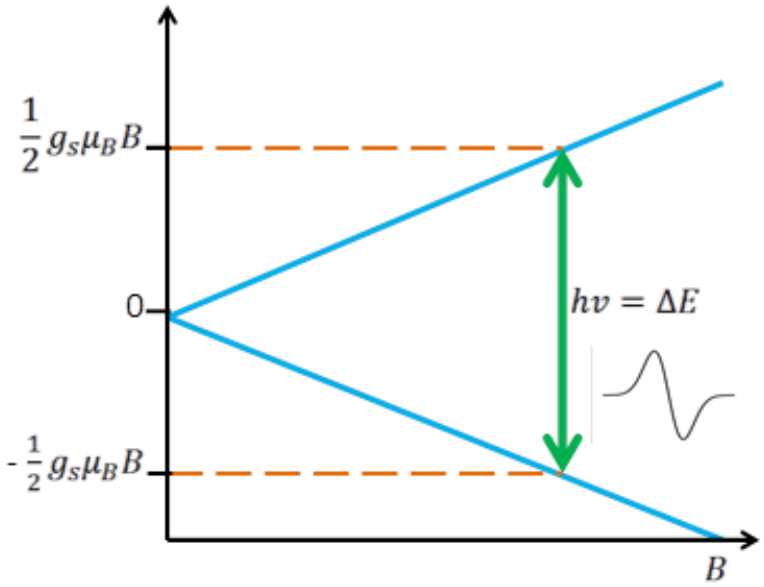

Figure 3.8: Energy level diagram of electron spin in applied magnetic field B (ms = ±1/2) **[28]**.

The observed electron paramagnetic resonance (EPR) spectra is the result of the spectroscopic detection of this resonance. As shown in Figure 2, the three main components of the electron paramagnetic resonance (EPR) technique are the microwave bridge (resonator), signal detector, and the magnetic field source. The frequency produced from the microwave is transferred across the waveguide to the specimen located between magnets. The electron paramagnetic resonance (EPR) spectra can be performed by differing the magnetic field while maintaining a constant frequency or by differing the frequency while maintaining a constant magnetic field. The JEOL (EPR) spectrometer X-band working at 9.4 gigahertz at the room temperature was utilized in this study **[29]**.

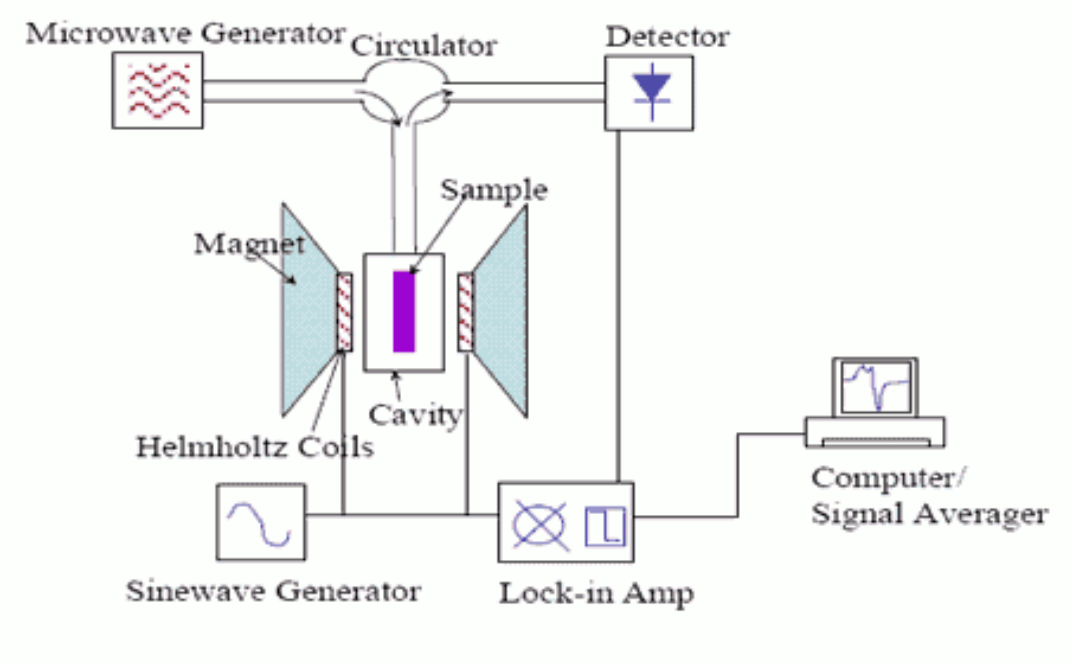

Figure 3.9: Schematic diagram of the electron paramagnetic resonance **[29]**.

3.4.7. ENERGY-DISPERSIVE X-RAY SPECTROSCOPY (EDX, EDS, OR EDXS)

An X-ray technique (also known as EDS or EDXA) known as Energy Dispersive X-ray Analysis (EDXA) is utilized to establish the elemental configuration of the material used in combination with an electron microscope. This approach is based on creating a unique x-ray image that reveals the components contained in the sample. Since each element has a different atomic structure, the peaks of the X-ray emission spectrum are clearly clustered. This is the fundamental concept of EDX characterisation **[30]**.

Fitzgerald, Kiel, and Heinrich were the first to employ solid-state detectors for electron beam microanalysis in the late 1960s. Since then, the detector resolution has

improved to less than 150 eV. The EDS is the most frequently used microanalysis to link to scanning electron microscopes because solid sensors can record information faster and are easier to use. From a tiny beryllium window, the X-ray beam enters an air-cooled reverse-biased lithium drift silicon sensor. In the reverse-biased diode's sensor, X-ray photon absorption generates photo-electrons and electron-hole pairs. The detector bias voltage wipes out these electron-hole pairs, and the charge-detecting amplifier then transforms them into voltage pulses. The signal is amplified even further before being transferred to a pulse-height analyser, where the pulses are organized by voltage. On a data processor, the voltage dispensation can be examined and modified to locate data or peaks **[31]**.

By concentrating a high-energy beam or X-ray of charge carriers (such protons or electrons) on a sample, this method excites it to create separate X-rays. In the sample, the electrons in the stationary atom are at unexcited or discrete energy levels in the ground state (or electron shell bonded to the nucleus). When the incoming beam agitates an electron from the inner shell, a "hole" is created for an electron from the outer elevated-energy shell to fill. It has the ability to emit an X-ray beam with the energy difference between the high and low energy shells. A material's amount of x-rays may be counted and quantified using an energy dispersive spectrometer. The atomic structure of the element it is released, as well as the energy difference between two shells, define the X-rays' energy, allowing the elemental composition of the sample to be identified as displayed on **Figure 3.10 [32]**.

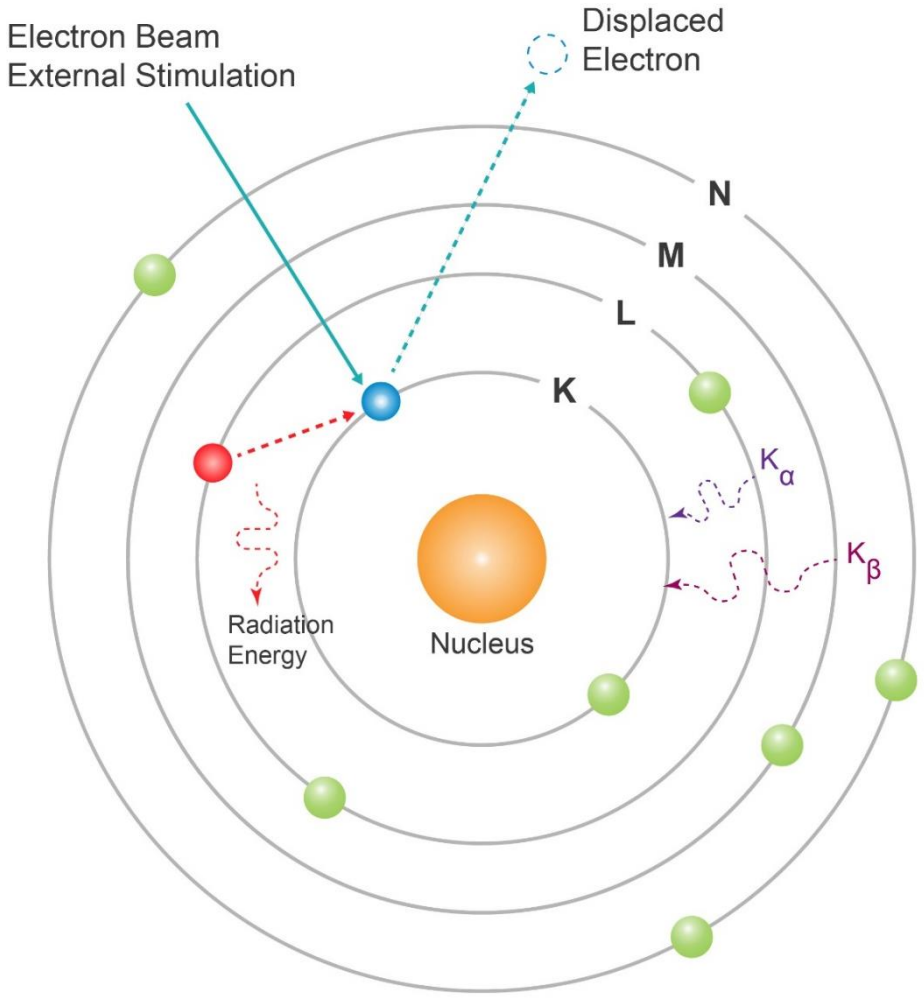

Figure 3.10: Schematic diagram of the principle of EDX, EDXS, or EDS **[32]**.

3.4.8. X-RAY PHOTOELECTRON SPECTROSCOPY (XPS)

A surface technique called X-ray photoelectron spectroscopy (XPS) computes the chemical states, constituent configuration, surface states, and electronic states of the components in a substance. It has a close connection to EDS. It employs ejected electrons in a similar manner to Auger electron spectroscopy (AES). The element-specific binding energies of these emitted electrons are calculated from the kinetic energies and quantities of emitted electrons, allowing for chemical characterisation of

a sample **[33]**. Siegbahn first reported the technique in 1967, based on Einstein's description of the photoelectric effect in 1905 **[34]**. In 1969, he was granted the Nobel Prize in Material science for creating the introductory exchanging monochromatic XPS strategy with his group about gather at Sweden's Uppsala institution.

According to Einstein, light is not a wave, so the photoelectric effect describes how electrons are ejected from a metal surface when exposed to light. A photon is a group of wave parcels in relation to energy (E) as equal to E=hv, where v is frequency and h is the Planck constant. The photon vitality ought to be more prominent than the work function (ϕ) of the material for the electron to be emitted; otherwise, no electrons are emitted.

As a result, the photoelectric effect equation becomes:

$$Ek = hf - \phi, \qquad \textbf{[35]}$$

Where Ek is the emitted electron's maximum kinetic energy. Excited electrons migrate from the nuclear to the continuum states, forming holes and ions (X+) in the molecule. A detector measures the kinetic energy of the ejected electron. Because XPS relies on photoemission from x-rays with energies ranging from 100 eV to 100 keV, Einstein's photoelectric impact condition can be used to calculate the orbital's binding energy from which an electron is discharged. To calculate the binding energy of each emitted electron, Ernest Rutherford proposed Equation below.

$$\text{Binding Energy (BE)} = EP - Ek - \phi \qquad \textbf{[36]}$$

The Ep is the given energy of the substance from the incident X-ray photons. The XPS spectrum’s characteristic spectral peaks, with each peak representing the amount of element present, represent the atomic electronic configurations (1s, 2s, 2p, and 3s). The XPS method is shown schematically in **Figure 3.11** to account for the long one-

meter track length between the sensors and the substance, the instrument's XPS detectors require ultra-high vacuum to operate. Only electrons emitted and detected by the detector are counted. Excited electrons recombine within the material, are trapped in excited states, or collide in-elastically, leaving fewer electrons to escape. It should be noted that the XPS cannot detect hydrogen or helium **[37]**.

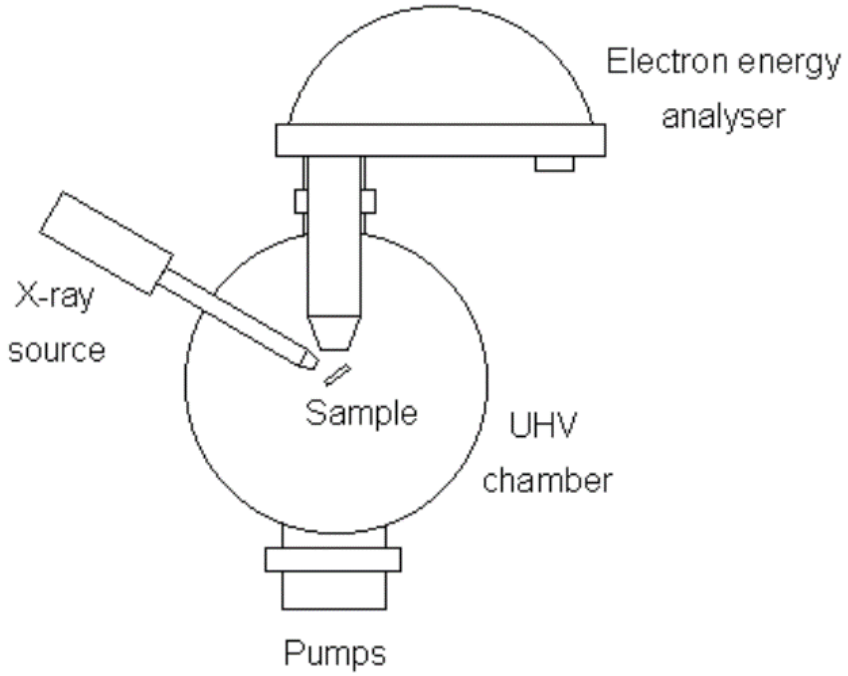

Figure 3.11: The Schematic diagram of XPS technique **[38]**.

3.4.9. GAS TESTING STATION

The gas detection properties were next studied in two particular atmospheres at temperatures ranging from 250 to 400 °C using a KENOSISTEC KSGAS6S gas detection station and altering the voltage (Italy). The gas sensing experiments in this work were carried out using a KENOSISTEC UHV equipment gas station (**Figure. 3.12**). The system includes a sensing chamber with a sampling stage, an air mixer

and a dry air inlet to supply dry air to the mixer, 4 unequal gas inlets, and a flow controller to control the amount of air in the chamber, 2 thermostatically controlled tanks, and 1 Includes thermostatic tanks. A device that supplies humidified air to the mixer and a device that measures volatile gas when measuring humidity, six KEITHLEY picometers for measuring conductivity and six warmers that provide voltage across the specimen, gas inlet and outlet, including a vent. Then the specimens were displayed to gas and moisture in the chamber for a long time. Pico amperes measure conductivity on the various gases and humidity, while heaters provide voltage across the sample.

Figure 3.12: Schematic diagram of an installed KENOSISTEC KSGAS6S gas sensor station **[39]**.

REFERENCES

1. https://en.wikipedia.org/wiki/Scanning_electron_microscope#/media/File:Schema_MEB_(en).svg

2. K. Mills, H. Dong, Nanofiber technology: Introduction to production and treatment http://www.research.cornell.edu/KIC/events/Journalists2007/pdfs/Electrospinning.pd.

3. S. Zhang, F. Gelain, X. Zhao, Dynamic Behaviors of Lipid-Like Self-Assembling

4. J. Goldstein, Third Edition, Springer (2003).

5. C. Wang, X. Chu, M. Wu, Sens.Actuators, B, 113 (2006) pp. 320-323.

6. J. Goldstein, et al. Scanning Electron Microscopy and X-ray Microanalysis (3rd ed.), Plenum Press, New York (2003).

7. P.J. Breton From microns to nanometers: early landmarks in the science of scanning electron microscope imaging Scanning Microsc., 13-1 (1999) pp. 1-6.

8. S. Gupta, A. Joshi, M. Kaur, J. Chem. Sci., 122 (2010) pp. 57-62.

9. D. Basak, G. Amin, B. Mallik, G. Paul, S. Sen, J. Cryst.Growth, 256 (2003) pp. 73-77.

10. W.J. Dawson, Hydrothermal Synthesis of Advanced Ceramic Powders, American Ceramic Soc. Bull, 67 (1988) pp. 1673-1678.

11. Dina N. Oosthuizen, David E. Motaung, Hendrik C. Swart, In Depth Study on the Notable Room-Temperature NO2 Gas Sensor Based on CuO Nanoplatelets Prepared by Sonochemical Method: Comparison of Various Bases, Sensors and Actuators B: Chemical 266 (2018) pp. 761-772.

12. B.L. Cushing, V.L. Kolesnichenko, and C.J. O'Connor, Recent Advances in the Liquid-Phase Syntheses of Inorganic Nanoparticles, Chemical Reviews, 104 (2004) pp. 3893-3946.

13. https://www.sciencedirect.com/science/article/pii/B9780128095973004466#f0030.

14. N. Han, X. Wu, L. Chai, H. Liu, Y. Chen, Sens.Actuators, B, 150 (2010) pp. 230-238.

15. W. Guo, T. Liu, R. Sun, Y. Chen, W. Zeng, Z. Wang, Sens.Actuators, B, 178 (2013) pp. 53-62.

16. P. Rai, J.-N. Jo, I.-H. Lee, Y.-T. Yu, Mater. Chem.Phys., 124 (2010) pp.406-412.

17. https://commons.wikimedia.org/wiki/File:Schematic_of_UV_visible_spectrophotometer.png

18. https://icjs.us/uv-vis-spectroscopy-a-step-in-the-light-direction/

19. Abdelhalim, M. A. K., Moussa, S. A. A., & AL-Mohy, Y. H. (2013). Ultraviolet-Visible and Fluorescence Spectroscopy Techniques Are Important Diagnostic Tools during the Progression of Atherosclerosis: Diet Zinc Supplementation Retarded or Delayed Atherosclerosis. BioMed Research International, 2013, pp. 1–8. https://doi.org/10.1155/2013/652604.

20. UV-Visible Spectroscopy. (2016, July 13). Chemistry LibreTexts.

21. UV-visible-NIR reflectance spectrophotometry in cultural heritage: Background paper (2016).AnalyticalMethods, 8(30), pp. 5894–5896. https://doi.org/10.1039/C6AY90112C.

22. Chen, X., Yin, G., Zhao, N., Gan, T., Yang, R., Xia, M., Feng, C., Chen, Y., & Huang, Y. (2021). Simultaneous determination of nitrate, chemical oxygen demand and turbidity in water based on UV–Vis absorption spectrometry combined with interval analysis. Spectrochimica Acta Part A: Molecular and BiomolecularSpectroscopy,244,118827.https://doi.org/10.1016/j.saa.2020.118827.

23. Abdelhalim, M. A. K., Moussa, S. A. A., & AL-Mohy, Y. H. (2013). Ultraviolet-Visible and Fluorescence Spectroscopy Techniques Are Important Diagnostic Tools during the Progression of Atherosclerosis: Diet Zinc Supplementation Retarded or Delayed Atherosclerosis. BioMed Research International, 2013, pp. 1–8. https://doi.org/10.1155/2013/652604.

24. P.L. Hall, Clay Minerals 15 (1980) pp. 321-335.

25. A.R. Barron, Connexions (2014).C.V. Raman, K.S. Krishnan, Indian J. Phys. 2 (1928) pp. 387-398.

26. E. Smith and G. Dent, Wiley and Sons Ltd., Great Britain (2005).

27. J. Bhat, A. Patil, N. Swami, B. Mulimani, B. Gayathri, N. Deshpande, G. Kim, M. Seo, Y. Lee, J. Appl. Phys., 108 (2010) pp. 043513.

28. http://stanford.edu/courses/2007/ap272/thareja1/.

29. D.M. Murphy, Chapter 1, WILEY-VCH Verlag GmbH & Co. KGaA, Weinheim (2009).

30. https://en.wikipedia.org/wiki/Energy-dispersive_X-ray_spectroscopy

Wikipedia, “Energy-dispersive X-ray spectroscopy - Wikipedia, the free encyclopedia,”

31. https://www.semitracks.com/reference-material/failure-and-yield-analysis/failure-analysis-materials-characterization/energy-dispersive-x-ray-spectrometry.php

32. Wikipedia, “Energy-dispersive X-ray spectroscopy - Wikipedia, the free encyclopaedia,” Wikipedia, 2014. [Online]. Available: https://en.wikipedia.org/wiki/Energy-dispersive_X-ray_spectroscopy. [Accessed 237 2014].

33. A. Einstein, Ann. Physik 17 (1905), pp. 132. 1921 Nobel Prize in Physics.

34. R.F. Egerton, Springer (2005).

35. J. Goldstein, Third Edition, Springer (2003).

36. L.C. Feldman, J.W. Mayer, (1986).

37. http://www.chem.qmul.ac.uk/surfaces/scc/scat5_3.htm.

38. https://www.researchgate.net/publication/224830248_Synthesis_and_Stoichiometric_Analysis_of_a_LiIon_Battery_Cathode_Material/link/554b019a0cf21ed21359025f/download

39. https://www.kenosistec.com/en/thin-film-deposition-systems/gas-sensor-test-system/.

CHAPTER FOUR

COMPARISON STUDY ON ZNO AND CUO GAS SENSING CHARACTERISTICS: TEMPERATURE MODULATED-DUAL SELECTIVITY TOWARDS BENZENE AND XYLENE VAPOURS*

4.1. INTRODUCTION

The swift advancement of science and technology has indeed led to improved quality of life for mankind, while at the same time, it has also led to increased air pollution globally. For instance, in households, mankind is threatened by the emission of volatile organic compounds (VOCs) from furniture or paint, nitrogen dioxide, carbon monoxide from coal stoves, etc., which leads to serious indoor air pollutions **[1-3]**. Among them, benzene, toluene, ethylbenzene, and xylene (BTEX) are utilized as organic solvents in the factories of paints, leather, and plastic. BTEX are dangerous aromatic hydrocarbon compounds, which have become ever-present environmental air pollutants in urban and rural zones of industrialized and emerging nations. The World Health Organization (WHO) has validated BTEX vapours as sturdy carcinogen. This has prompted several institutes, such as the Occupational Safety and Health Administration (OSHA), and National Institute for Occupational Safety and Health (NIOSH) to establish precise recommendations to guarantee harmless and well working environments for the workers exposed to BTEX. Presently, exclusive and dedicated profitable laboratory approaches are extensively utilized to detect BTEX in

* **This chapter is published in Materials Chemistry and Physics, 297, (2023), 127352**

indoor and outdoor environments, as well as gas chromatography-mass spectrometry (GC-MS) and photoionization detector (PID) methods **[4, 5]**.

The major limitation of the above-mentioned techniques is that they are very bulky, which makes them difficult to handle. In addition, they are expensive and require skilled technicians and more time for operations and analyses **[6]**. These limitations make them inappropriate for real-time applications in environmental monitoring, which has become a significant challenge in the scientific community. Therefore, alternate approaches to rapidly detect BTEX compounds precisely, predominantly at low concentrations ppm are required. Currently, gas sensor technologies developed from semiconductor metal oxides (SMOs), have attracted significant attention in the scientific community owing to their portability. As a result, among the SMOs, an n-type ZnO with a bandgap of 3.37 eV was used for the detection of harmful gases, due to its unique features, such as low cost, non-harmfulness, and high conductivity **[7-9]**.

The advantage of ZnO material is that it can be easily prepared in various morphologies, which lead to higher surface defects, like oxygen vacancies (V_O), which are significantly beneficial for the gas-sensing properties **[10]**. Nevertheless, the application of ZnO SMO for detection of VOCs as an individual gas sensor is very limited, let alone it displays a superior response. In addition, it is difficult to monitor or detect BTEX, due to its chemical inertness which causes alteration and recombination of sensing nanostructures. Several efforts have been made to detect BTEX by modifying the structure of ZnO with various shapes and defects **[11, 12]**, by incorporating transitional metals **[13, 14]**, noble metals **[15, 16],** single walled carbon nanotubes **[17]** and boron nitride materials **[18]**. However, for the practical application of BTEX detection for indoor quality monitoring, greener, safer, and economical approach should be considered. In contrast to n-type materials, p-type SMOs have

also attracted attention over the past few years. Within the p-type SMOs, CuO has reflected as one of the most used materials, due to its narrow bandgap of 1.2 eV. CuO is acknowledged as one of the best catalysts catalytic combustions of BTEX and promotes the alteration of BTEX to an oxidized intermediate **[19-24]**. Fe et al. **[22]** investigated the geometrical influence of CuO materials on the catalytic combustion of benzene to CO_2. The observations pointed out that the amount of oxygen species contents was sturdily reliant on the orientation of crystal planes. Several efforts have been made to detect BTEX using pure CuO **[22]** and a series of CuO/SnO_2 composites **[24]**.

Thus, realizing a tuned gas-sensing material, that can display excellent sensitivity and selectivity, and rapid recovery times for the detection of BTEX compound related environmental pollution, remains a significant scientific challenge. Such difficulties are caused by their similar physical and chemical properties. In addition, there are no studies demonstrating dual-mode selectivity towards benzene and xylene at low operational temperatures of 75 and 150 °C, particularly utilizing a single or undoped SMO ZnO. The current study focuses on the fabrication of various nanostructures using different bases (NaOH, NH_4OH, Urea and KOH). The use of various bases is driven by their influence on the surface morphology, structural properties, and surface defects **[25, 26]**. For instance, previous study **[26]** have reported that among the mentioned bases above, NaOH has shown better surface defects, like oxygen vacancies (V_O), which are very beneficial for gas sensing characteristics. Thus, herein, we report on the dual mode-temperature selectivity towards benzene and xylene vapors at low operational temperatures of 75 and 150 °C, respectively, using a ZnO based sensor prepared using NaOH. The sensor disclosed an ultra-sensitivity, selectivity, and low limit of detection of 18 ppb towards xylene, which was linked to

improved V_O observed in the *in-situ* photoluminescence and electron paramagnetic resonance studies. The ZnO-NaOH sensor showed impressive long-term operational features after storage for 36 months in ambient environments.

4.2. EXPERIMENTAL DETAILS

4.2.1. MATERIALS

Copper (II) acetate monohydrate (Cu $(CO_2CH_3)_2$. H_2O), zinc acetate dihydrate (Zn $(CO_2CH_3)_2$. $2H_2O$), ammonium (NH_4OH) (30-33% NH_3 in water, 99.99%), sodium hydroxide (NaOH, 99%), urea, potassium hydroxide (KOH, 99%) and ethanol (99% purity) were purchased from Sigma-Aldrich.

4.3. SYNTHESIS METHOD

Firstly, 3 grams of Copper (II) acetate monohydrate, 3 grams of Zinc acetate dihydrate were added into two separate beakers, 150 ml of distilled water as a solvent was added to each beaker and stirred for 1 hour (h) thereafter, 5 ml NH_4OH was added dropwise under continuous stirring until the pH of 9.00 was reached. The solution was then stirred at 20 °C for 1 h. The same procedure was repeated using different bases (i.e., 5 ml of NaOH, urea and KOH). The mixtures were transferred to Teflon-lined autoclave reactor vessels and then placed in an oven for 16 h at 180 °C. After cooling to room temperature, the products were centrifuged and washed 10 times with distilled water at interval of 0-10 minutes. The final product was dried at 80 °C for 15 h and calcined at 300 °C for 2h.

4.4. CHARACTERIZATION TECHNIQUES

The structure was analysed using X-ray diffraction (Bruker AXS D8 Advance x-ray diffractometer with a Cu-kα (λ = 1.5406 Å). The morphology was analysed using a Zeiss scanning electron microscope (SEM) operated at 3kV EHT. *In-situ* photoluminescence (PL, spectrometer with a Kimmon IK series 325 nm laser) and electron paramagnetic resonance (EPR, FSA JEOL) results were measured at 25, 75 and 150 °C, to associate with the gas sensing conditions. XPS analyses were performed using PHI 5000 Scanning ECA Microprobe.

4.5. FABRICATION AND TESTING OF THE SENSING DEVICES

The preparation and fabrication of ZnO- and CuO-based sensors were conducted according to ref. **[6]**. The nanostructured materials were ultrasonically dispersed in ethanol (Analytical Reagent) to achieve a 2.5 mol/L suspension. The suspension was sonicated for 30 min to obtain a corresponding slurry. The slurry was carefully pasted onto platinum (Pt) inter-digital pattern on an alumina substrate. The change in resistance was performed utilizing a 4-channel Gas Mixing System (GMS) gas testing instrument (see **Scheme 4.1**). The fabricated sensors were positioned in a Teflon chamber and tested to benzene, ethylbenzene, toluene, xylene (BTEX), and nitrogen dioxide. The analyses were performed at different operating temperatures (25, 75, 150 and 200 °C) by adjusting the heating voltage. Prior to the sensing analyses, the sensors were exposed to dry air for 3 h to stabilize the resistance during the analyses, which were then exposed to the target gases for 5min, and dry air was allowed to flow for 5 min for recovery. Additionally, the measurements were further conducted at relative humidity (RH) of 40 and 60%. The response of the sensors was stated as

R_a/R_g for the reducing and R_g/R_a, for oxidizing gas, where R_a and R_g represented sensor exposed to air (R_a) and tested analyte, respectively.

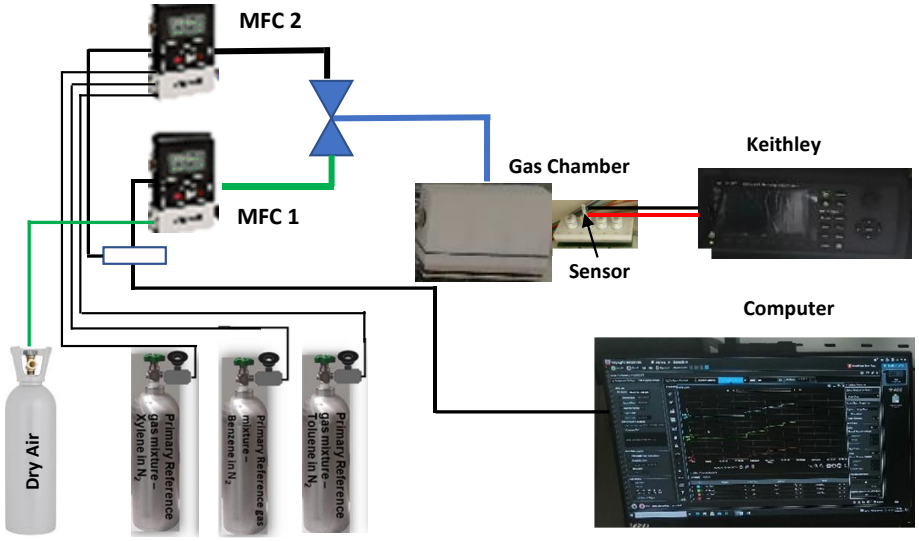

Scheme 4.1: Gas sensing set-up.

4.6. RESULTS AND DISCUSSION

4.6.1. MORPHOLOGY AND STRUCTURAL ANALYSIS

SEM was utilized to study the surface morphology of ZnO synthesized using various bases. The ZnO-NaOH nanostructures are displayed in **Figure 4.1: a-c**, showing short rod-like structures and nanoparticles, where some are interconnected with tiny voids. The short rod-like structures have an estimated average diameter of 1.1 µm. Nonetheless, using NH_4OH as the base (i.e., ZnO-NH_4OH), agglomerated nanoplatelets with an estimated average thickness of 27 nm, are presented in **Figure 4.1: d-f**. The nanoplatelets were directed radially outwards displaying a tetragonal shape with sharp/pointy tops. Upon using urea as the base, (**Figure 4.1: g-i**), nanoplatelets, which were randomly arranged to form a spherical shape were

observed. When using KOH as a base (**Figure 4.1: j-l**), platelets and rod like structures, with diameter ranging around 50-70 nm were observed.

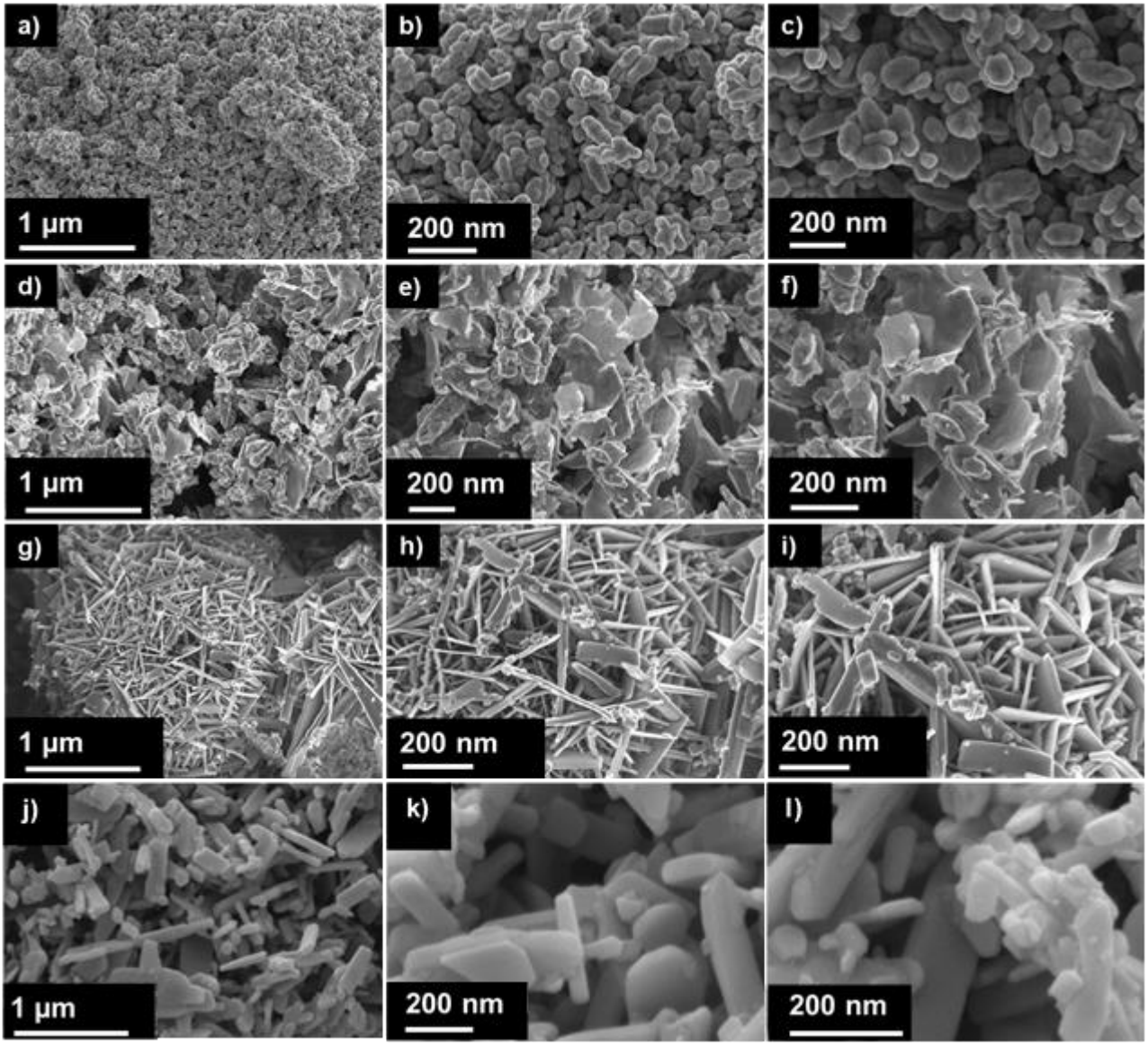

Figure 4.1: Low to high magnification SEM images nanostructure for ZnO prepared with (a-c) sodium hydroxide (NaOH), (d-f) with ammonium hydroxide (NH_4OH), (g-i) with urea, and (j-l) KOH.

4.6.2. POSSIBLE GROWTH MECHANISM

The growth mechanism of ZnO nanoparticles synthesised using NaOH follows Ostwald ripening. The reaction occurring between the Zn precursor and NaOH solution are presented in Equations (**1-6**) **[27, 28].**

$$Zn^{2+} + 2OH^{-} \leftrightarrow Zn(OH)_2 \quad \textbf{(1)}$$

$$Zn(OH)_2 + 2OH^{-} \leftrightarrow [Zn(OH)_4]^{2-} \quad \textbf{(2)}$$

$$[Zn(OH)_4]^{2-} \leftrightarrow Zn_2^{2-} + 2H_2O \quad \textbf{(3)}$$

$$Zn_2^{2-} + 2H_2O \leftrightarrow ZnO + 2OH^{-} \quad \textbf{(4)}$$

$$ZnO + OH^{-} \leftrightarrow ZnOOH^{-} \quad \textbf{(5)}$$

$$ZnOH^{-} + Na^{+} \leftrightarrow ZnOOH - Na \quad \textbf{(6)}$$

The ZnO nuclei are formed from the hydrated $Zn(OH)_4$ colloids once supersaturation is reached. During synthesis nucleation occurs first, whereby small crystallites form and due to the energy difference, they agglomerate forming lager crystals. The nucleation and growth rate are affected by several factors, including supersaturation, which is the concentration of NaOH **[29]**. At lower supersaturation, larger crystallite sizes are often observed due to the rapid crystal growth and slow nucleation experienced. This promotes formation of 1-3 dimensional morphologies, such as (tubes, rods, hierarchical, etc.). The opposite is observed at higher supersaturation where nucleation is promoted over crystal growth consequently smaller crystals with morphologies, such as nanoparticles are achieved as seen in **Figure 4.1: a-c.** Therefore, in this work it can be clearly seen that the reaction is dominated by crystal nucleation. Additionally, the crystal growth is deferred by the dissociation of NaOH to Na^{+} and OH^{-} ions, resulting to formation of nanoparticles.

In the case of NH_4OH as a base, the ZnO nanostructures formed irregular shaped of flake platelets. The growth mechanism can be explained using the subsequent steps in equations (**7-15**) **[30, 31]**:

$$Zn(CH_3COO)_2 \rightarrow 2CH_3COO^- + Zn^{2+} \quad \textbf{(7)}$$

$$CH_3COO^- + H_2O \rightarrow OH^- + CH_3COOH \quad \textbf{(8)}$$

$$NH_3 + H_2O \leftrightarrow NH_4^+ + OH^- \quad \textbf{(9)}$$

$$Zn^{2+} + 2OH^- \rightarrow Zn(OH)_2 \quad \textbf{(10)}$$

$$Zn^{2+} + 4OH^- \rightarrow Zn(OH)_4^{2-} \quad \textbf{(11)}$$

$$Zn^{2+} + 4NH_4^+ \rightarrow [Zn(NH_3)_4]^{2+} \quad \textbf{(12)}$$

$$Zn(NH_3)_4^{2+} + 2OH^- \rightarrow ZnO + 4NH_3 + H_2O \quad \textbf{(13)}$$

$$Zn(OH)_4^{2-} \rightarrow ZnO + H_2O + 2OH^- \quad \textbf{(14)}$$

$$Zn(OH)_2 + 2OH^- \rightarrow Zn(OH)_4^{2-} \quad \textbf{(15)}$$

The $Zn(CH_3COO)_2.2H_2O$ dissolved in deionized water dissociate into Zn^{2+} ions and CH_3COO^- ions that further hydrolyses, producing OH^- ions. The OH^- ions together with the NH_4^+ ions from the added ammonia solution reacts with the Zn^{2+} ion forming $[Zn(NH_3)_4]^{2+}$, $Zn(OH)_2$ and or $Zn(OH)_4^{2-}$ complexes. Further reaction of the complex ions with OH^- ions results to nucleation of ZnO crystals. When using NH_4OH as a base, supersaturation is reached at a level lower than that of NaOH. In accordance with the Ostwald ripening process, crystal growth occurs at a moderate rate in such that nucleation is surpassed and promotes the controlled formation of platelets or disc like structure.

In the case of using urea as base, the growth mechanism is proposed in refs. **[32, 33].** In this process, the formation of ZnO nanoplatelets comprises the following order of reactions in the aqueous solution comprising Zn^{2+} and urea:

$$CO(NH_2)_2 + 3H_2O \rightarrow 2NH_4OH + CO_2 \uparrow \quad \textbf{(16)}$$

$$NH_4OH \rightarrow NH_4^+ + OH^- \quad \textbf{(17)}$$

$$5Zn^{2+} + 2CO_2 + 6OH^- + 2H_2O \rightarrow Zn_5(CO_3)_2(OH)_6 + 4H^+ \quad \textbf{(18)}$$

$$Zn_5(CO_3)_2(OH)_6 \rightarrow 5ZnO + 3H_2O + 2CO_2 \quad \textbf{(19)}$$

When heating the precursor solution, CO_2 and OH^- are being released by urea as depicted in Equations (**16-17**). As a result, CO_2 reacts with Zn^{2+} in the alkali solution and form basic zinc carbonate, see Equation **18**. According to Equation **19**, when annealing the nanostructures at 400 °C, decomposing of basic zinc carbonate to produce CO_2 and H_2O occurs and this leads to the observed ZnO nanoplatelets in **Figure 4.1: g-i**.

When using a strong basic condition, such as KOH, all the dissolved $\mathrm{Zn(OH)_2}$ are arranged in a $\mathrm{Zn(OH)_4^{2-}}$ growth units that contains negative charge **[34]**. As a result, complex $\mathrm{Zn(OH)_4^{2-}}$ are hard to be incorporated on the positive and negative surface of ZnO. Thus, this restricts the growth of the crystal on [0001] direction and give rise to thicker nanoplates like structure as depicted in **Figure 4.1: j-l**. Further details can be found in ref. **[34].**

Figure 4.2: shows SEM images of CuO nanostructures measured at various magnifications, prepared using various bases. **Figure 4.2: a-c** shows that CuO-NaOH nanostructures are made of short nanorods, which are arranged randomly with

different lengths between 130-250 nm and some form an agglomerated cluster. In **Figure 4.2: d-f**, an irregular shape with nanoplatelets with almost uniform shape are observed when ammonia was used. When using urea, **Figure 4.2: g-i** (CuO- urea), nanostructures with a sphere like shape that are built up of hierarchical arrangements are observed. More interestingly, the spheres were hollow and had diameters of approximately 7-12 µm. The nanorods-like structures were directed radially outward displaying a tetragonal shape with sharp/pointy tops. When using KOH (**Figure 4.2: j-l**), CuO with platelets-like structures were observed. These nanoplatelets were also observed for the ZnO prepared with KOH. The diameter of the nanoplatelets ranges from 30 to 50 nm.

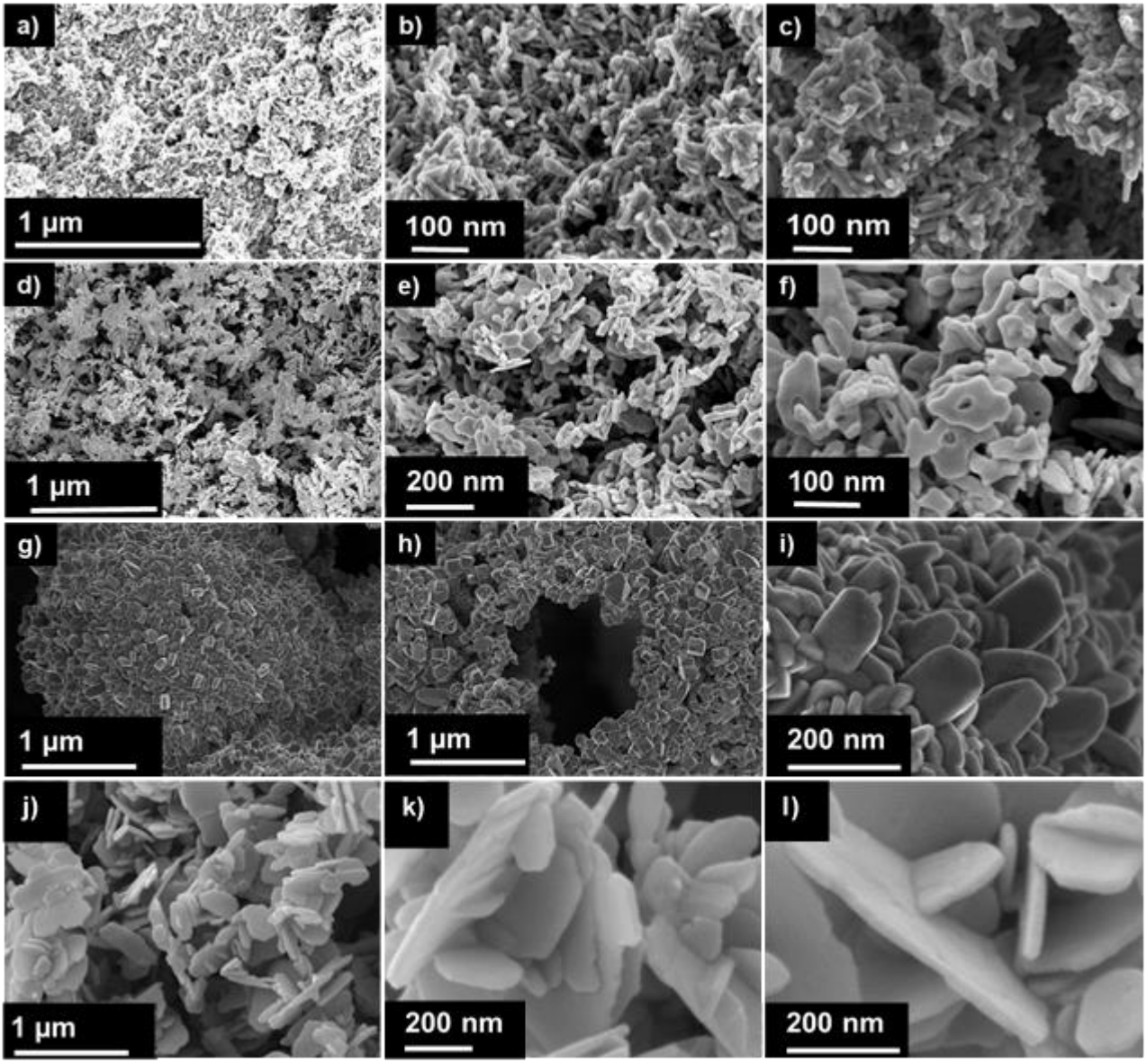

Figure 4.2: Low to high magnification of SEM micrographs of (a-c) CuO-NaOH, (d-f) CuO-NH_4OH, (g-i) CuO-Urea and (j-l) KOH.

Figure 4.3: illustrates XRD patterns of the pure ZnO and CuO synthesized using various bases. The XRD patterns of ZnO nanostructure in **Figure 4.3: a**, show that ZnO contains hexagonal wurtzite structure card number (JCPDS: 36-1451) **[11]**. In addition, the peaks shifted towards higher theta angles due to an increase in the lattice strain, see **Figure 4.3: c**. The diffraction peaks observed at 2θ = 31.81°,34.46°,36.28°, etc., are associated with the (100), (002), and (101) planes, respectively. For the ZnO-

KOH, the peaks are sharper, and the (002) is more exposed compared to that of other ZnO materials. The crystallite sizes were calculated using the Scherrer formula $D = \frac{k\lambda}{\beta cos\theta}$ **[35]** where $k, \lambda\ \theta\ and\ \beta$ are constant, wavelength of the X-ray, full width at half maximum and the Bragg's angle, respectively. Thus, crystallite sizes for ZnO-NaOH, ZnO-NH_4OH, ZnO-urea, and ZnO-KOH were 21.0, 24.6 26.6 nm, and 38.3 nm, respectively. **Figure 4.3: b** displays the XRD patterns of the pure CuO nanostructure samples prepared using various bases. The nanostructures were highly coordinated with the standard card of monoclinic CuO (JCPDS: 48–1548) **[36]**. The 2θ in the diffraction peaks are 33.20°,35.98°,39.18° and 68.46° corresponding to (110), (11-1), (111), (11-2), (20-2), (020), (202), (11-3), (022), (220) of CuO. The diffraction peaks are perfectly sharp, showing no impurities on all bases. The crystallite sizes of 13.4, 14.8, 23.9 and 19.9 nm were witnessed for the CuO-NaOH, CuO-NH_4OH, CuO-urea and CuO-KOH, respectively.

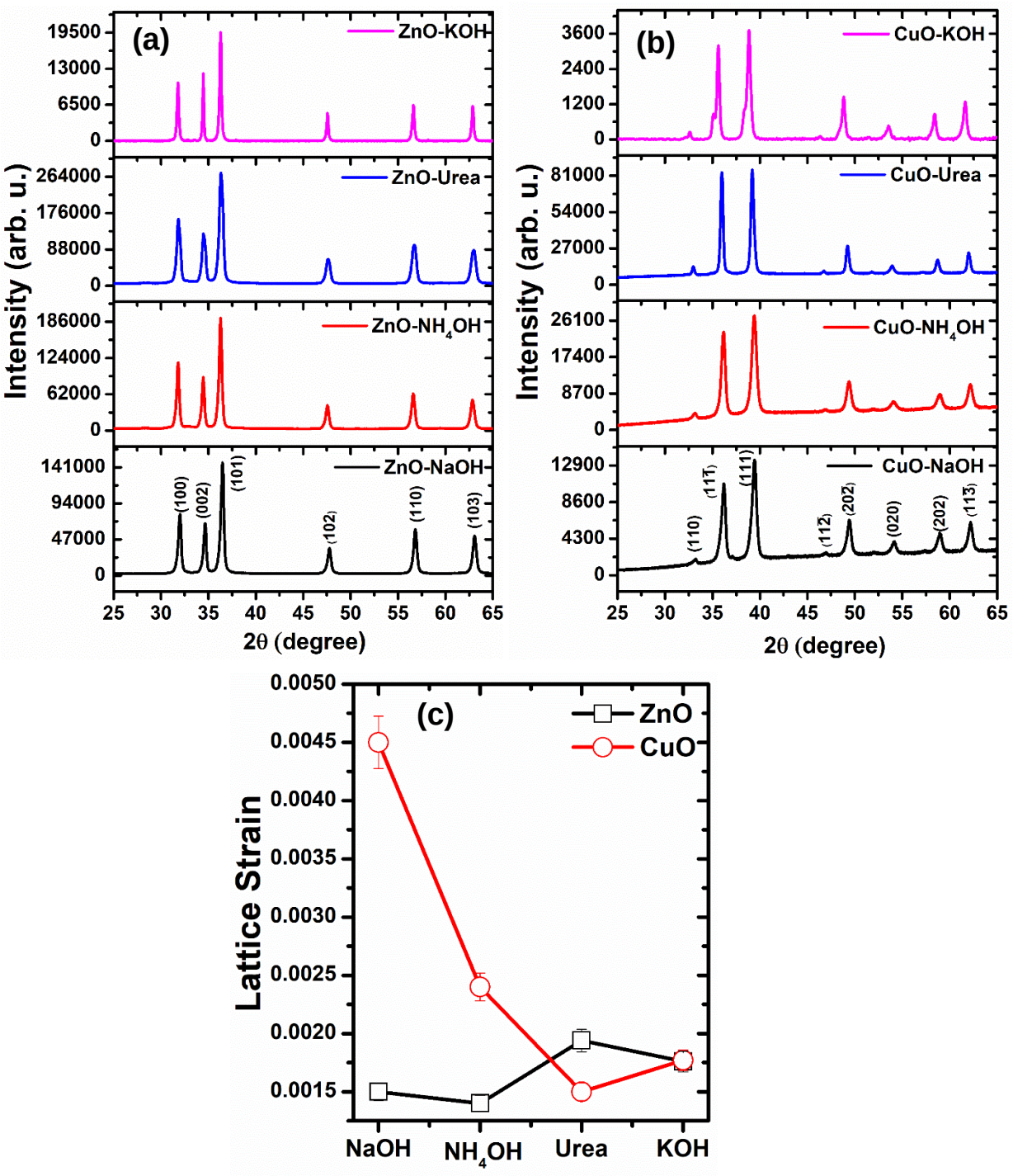

Figure 4.3: XRD patterns for (a) ZnO and (b) CuO nanostructures prepared using various bases. (c) Lattice strain of ZnO and CuO nanostructures prepared using various bases.

4.6.3. PHOTOLUMINESCENCE AND ELECTRON PARAMAGNETIC RESONANCE STUDIES

To study the role of defects in gas sensing, PL spectroscopy was performed at various operating temperatures (25, 75 and 150 °C). The in-situ PL spectra of ZnO in **Figure 4.4: a** and **b** disclose a sharp emission at 3.23 eV and a broad emission at 2.76 - 1.5 eV, which are associated with blue-green, yellow, and orange-red emissions, respectively. While that of ZnO-Urea illustrates emission at 2.96 and shoulder at 3.23 eV. The peak observed at 3.23 eV is usually referred to as the near-band-edge (NBE) peak, which originates from free exciton recombination **[37]**. As noted from **Figure 4.4: i)**, a clear shift is observed in the ZnO spectra prepared using various bases. Moreover, ZnO-NaOH exhibited higher PL emissions than its counterparts. Such PL emissions indicate that the nature and strength of the base have a solid effect on the surface of the nanomaterials. Mamabolo et al. **[38]** showed that the base had a significant impact on luminescence characteristics. They observed a colour variation from black to reddish, and then to grey for their SnO_2 prepared using various bases. The deconvoluted spectra show peaks at 2.43 eV, 2.0 eV, and 1.62 eV for the ZnO-NaOH. While the ZnO-NH_4OH shows peaks at 2.2 eV, 1.90 and 1.62 eV. Additionally, the emission spectra of ZnO-Urea display peaks at 3.0 and 2.86 eV, which are linked to zinc interstitials and oxygen vacancies (V_O). The ZnO-KOH shows PL emissions at 2.4, 2.0 and 1.61 eV, which are almost in the same positions as those of ZnO-NaOH. The green emission at 2.43 eV is related to the recombination of electrons trapped in singly ionized oxygen vacancies (F^+ centre or V_O^+) with photogenerated holes **[37, 39]** or zinc vacancies (V_{Zn}) **[40]**. The PL emissions in the range of 1.90 and 2.2 eV are correlated to the doubly ionized oxygen vacancy (F^{+2} centre or V_O^{+2}) **[39, 41]** and transitions from Zn interstitial to oxygen interstitials. The red emission witnessed at

1.62 eV is linked to excess of oxygen interstitial **[41]**. **Figure 4.4: e-h** demonstrates the in situ PL spectra of CuO nanostructures, prepared using different bases. All spectra show emissions in the range of 2.25-3.25 eV. The deconvoluted spectra using the Gaussian fit, show only three peaks for all CuO spectra. The CuO-NaOH shows emissions at 3.01, 2.86 and 2.76 eV, while those of CuO-NH_4OH are observed at 3.32, 2.95 and 2.83 eV. In addition, the CuO-urea emissions were observed at 3.38, 2.93 and 2.73 eV. A peak at 3.3 eV is related to NBE, while those observed at 2.93-2.86 eV and 2.7 eV are related to CuO characteristics and defect related emission, respectively **[42]**. Among the samples, the ZnO-NaOH showed strong PL emissions at 2.76 - 1.5 eV related to surface defects.

The in-situ PL measurements clearly show that the emission of the ZnO nanostructures synthesized utilizing different bases decreases with the operational temperature. Such behaviour was also observed for CuO-based materials. A decrease in the PL emission was also observed by Mamabolo et al. **[38]** and Tshabalala et al. **[6]** when using pure SnO_2 and TiO_2 nanostructures, respectively. By comparing the PL emission of various ZnO nanostructures at a sensing temperature of 25 and 150 °C, ZnO-NaOH indeed dominates in terms of surface defects (see **Figure 4.4: i** and **j**), which might lead to better sensing performance. The lower surface defects are justified by higher intensity of NBE peak emission observed for the ZnO-NH_4OH, ZnO-urea and ZnO-KOH, respectively.

Figure 4.4: k and **l** shows the the band gap energy (E_g) of the as-prepared ZnO and CuO using various bases. The band gaps were probed by utilizing Tauc's plot, by extrapolating the absorption edges. The Tauc's equation is defined as: $(\alpha hv) = B(hv - E_g)^n$, where α, h, v and B are absorption coefficient, Planck's constant,

incident light frequency, and proportionality constant, respectively. As depicted in **Figure 4.4: k** and **l**, and as well as in **Table 4.3**, the optical band gap values vary with the use of various bases, confirming that the base has indeed an effect on the band gap.

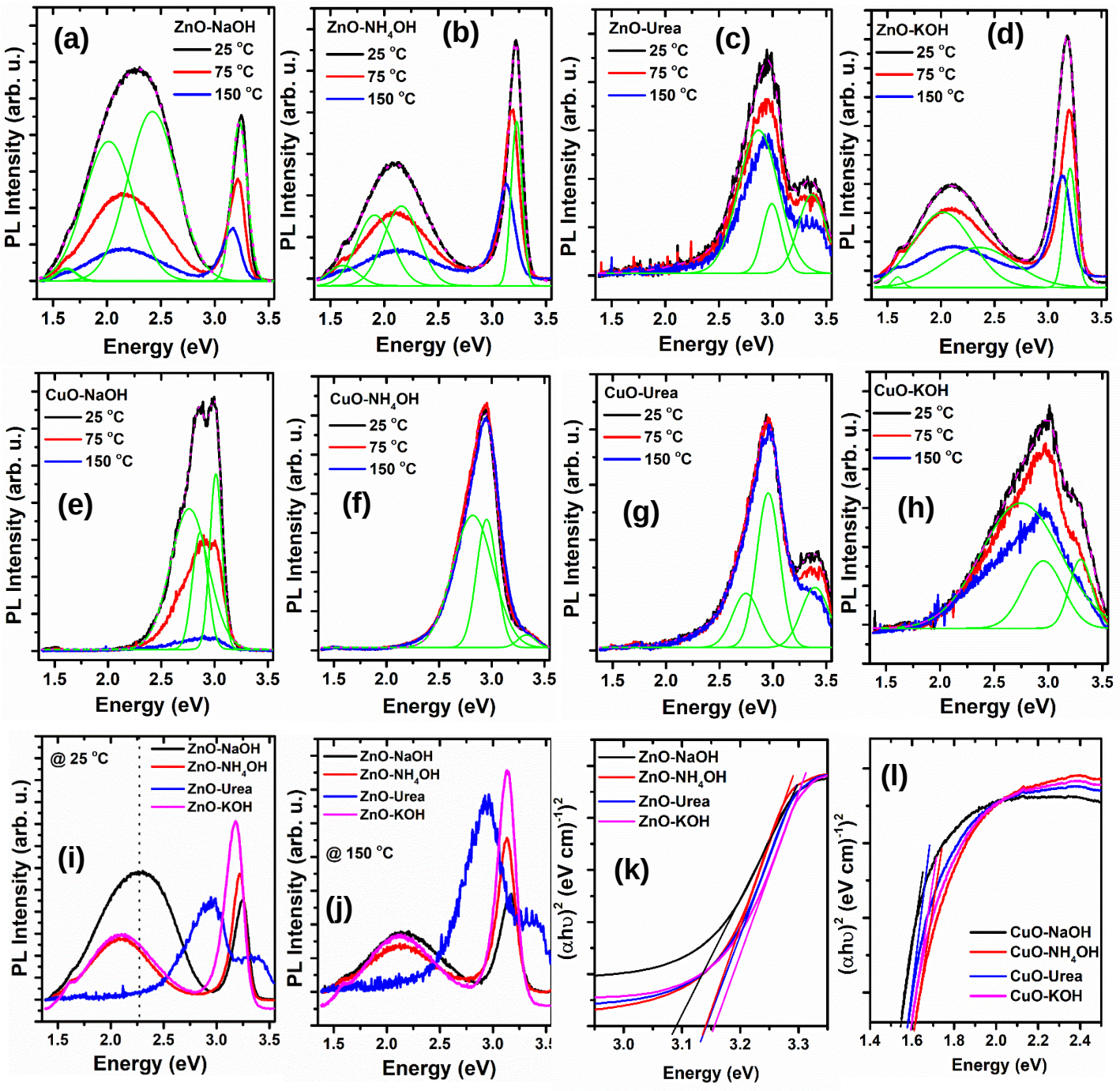

Figure 4.4: PL spectra illustrating the emissions of (a) ZnO-NaOH, (b) ZnO-NH_4OH, (c) ZnO-Urea, (d) ZnO-KOH, (e) CuO-NaOH, (f) CuO-NH_4OH, (g) CuO-Urea, and (h) CuO-KOH measured at various *in-situ* PL temperatures. PL spectra of ZnO prepared by using various bases, measured at (i) room temperature, and (j) 150 °C. UV-vis Tauc's plot showing the band gap energies of the various (k) ZnO and (l) CuO nanostructures.

To supplement the PL studies, we conducted *in-situ* EPR measurements at functional temperatures of 25, 75 and 150 °C. **Figure 4.5: a and b** displays the EPR analyses of pure ZnO and CuO synthesized utilizing different bases. All ZnO nanostructures exibited clear ferromagnetic (FM) signals. However, the pure CuO appear to display sharp peaks, which may be because the materials contain both FM and paramagnetic signals. Additionally, it is noted that ZnO-NaOH reveals higher FM signal, indicating that the material possess higher V_O, and this agrees with the PL results. Interestingly, the samples prepared using Urea as a base show a variation on the signals, where the EPR signal for ZnO-Urea shifted to higher field, while that of CuO-urea shows a small hump, see the arrow. A variation on the EPR signals was also witnessed by Mamabolo et al. **[38]**. They associated this behaviour with the variation of morphology induced by the use of different bases. The g-factors of $g \approx 1.990$ - 1.991 for ZnO-NaOH, ZnO-NH_4OH and ZnO-KOH and $g \approx 2.0018$ for ZnO-Urea observed. According to studies, the g-factors around 1.990 - 1.991 are associated to V_O **[26, 43]**, while that at 2.0018 is linked to V_{zn} **[26, 44]**. The in-situ EPR analyses in **Figure 4.5: c** also confim that the FM signals reduces when increasing the temperature, validating the PL findings.

Since the samples prepared using NaOH displayed higher surface defects, thus, the XPS analysis of ZnO-NaOH and CuO-NaOH nanostructures were conducted. The survey spectrum illustrating zinc and oxygen peaks is shown in **Figure 4.5: d**. The high-resolution spectra of the core level binding energy of Zn $2p_{3/2}$ and Zn $2p_{1/2}$ are observed at 1021.2 eV and 1044.4 eV, respectively (see **Figure 4.5: e**). The two peaks show the energy difference of roughly 23.1 eV, confirming the existence of Zn, chiefly in the Zn^{2+} chemical state **[35].**

The high-resolution XPS shows the Cu 2p peaks around 934.7−954.7 eV, which are associated with Cu $2p_{3/2}$ and Cu $2p_{1/2}$, as well as shakeup peaks, as revealed in **Figure 4.5: f**. The creation of CuO was established by Cu^{2+} with orbital splitting of about 0.5 eV between the Cu $2p_{3/2}$ and Cu $2p_{1/2}$, see **Figure 4.5: f [42]**. The high-resolution spectra of O 1s peaks for the ZnO-NaOH and CuO-NaOH are shown in **Figure 4.5: g** and **h**. The O 1s spectra showing four different distinctive peaks are observed at 528.0, 530.2, 531.5 and 532.1 eV for the ZnO-NaOH nanostructure. The peaks at 528, 530, 531 and 532 eV are linked to O^{2-} ions, lattice oxygen in hexagonal wurtzite structure oxygen vacancies (V_O) in the ZnO matrix, creation of adsorbed oxygen on the ZnO surface, respectively **[35]**. The O1s core level of CuO-NaOH only shows three peaks at 529.3, 530.5 and 532.5 eV, see **Figure 4.5: h**. Thus, the ZnO-NaOH showed higher relative percentage of the V_O (33.5%), compared to that of CuO-NaOH (16.2%). This shows that a higher V_O could be capable to interact strongly with the target gas molecules and lead in an improved sensing characteristic.

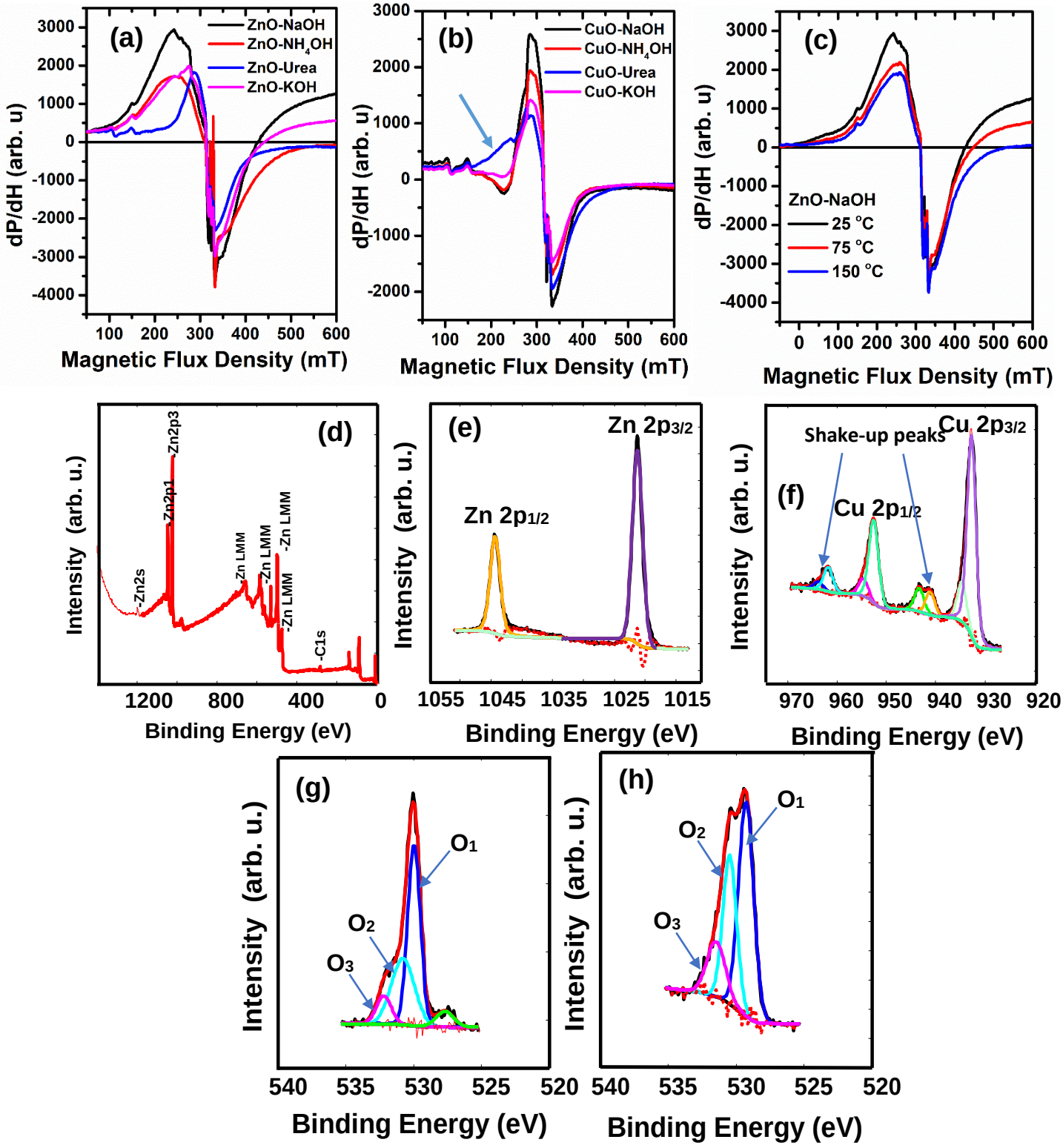

Figure 4.5: EPR spectra of the different (a) ZnO and (b) CuO nanostructures and (c) In-situ EPR measurements of ZnO-NaOH at different temperatures. XPS core level peaks of (d) Zn2p, (e) Cu2p, (f, g) O 1s of ZnO-NaOH and CuO-NaOH.

4.6.4. GAS SENSING CHARACTERISTICS

To assess the sensing behaviour of the fabricated sensors towards BTEX, ethanol and NO_2, different parameters were tested. It is acknowledged that operational temperature is vital on the properties of chemiresistive sensors, since it does not just affect the kind of adsorbed oxygen, but also influences the movement and migration of conductive carriers. As a result, the performances of the sensors were tested at various temperatures (25, 75, 150 and 200 °C). **Figure 4.6: a** and **b** displays the resistance in air (R_a) versus the operational temperature. The R_a for all the sensors reduces with operational temperature, illustrating a negative resistivity-temperature coefficient; thus, denoting the exceptional characteristic of SMO. This behaviour is due to more carriers that are created once the temperature increases, as a result leading to reduced sensing resistance. In this process, the sensing resistance is intensely dependent on the operating temperature. This behaviour has been witnessed by previous studies using either pure SMO, doped SMO or mixed SMO structures **[45-47]**.

Figure 4.6: c-h shows the response versus the operational temperature for BTEX, ethanol and NO_2 gas at an optimum concentration of 100 ppm. As shown in **Figure 4.6**, ZnO-NaOH show improved response towards benzene at low operational temperature of 75 °C, in comparison to other gases. Interestingly, when operating temperature was increased to 150 °C, the same sensor (i.e., ZnO-NaOH) demonstrated improved response towards xylene vapor. Nonetheless, at 200 °C, the response of sensor dropped, denoting that 150 °C is an optimal temperature. This shows that ZnO-NaOH has temperature dependent selectivity or (dual selectivity)

towards benzene and xylene. A dual temperature selectivity towards BTEX was previously observed by Kim et al. **[48]** towards xylene and toluene at elevated temperatures of 350 and 400 °C, respectively, utilizing an Nb-doped NiO hollow-sphere-based sensor. This observation was also observed by Tshabalala et al. **[6]** using TiO_2 nanowires for toluene and xylene detection at 25 and 125 °C, respectively. Furthermore, the ZnO-NH_4OH-based sensor also showed an improved response towards toluene and ethanol compared to other sensors at 150 °C. While at 200 °C, the responses reduced. The decrease in reduction of the sensor response could be associated to adsorption saturation. When the operational temperature increases the analyte gas is desorbed prior it can interact with the adsorbed oxygen ions on the surface of the sensors, as a result, a reduction in the sensing response is observed. The sensors prepared using either Urea or KOH base displayed poor responses when exposed to various analytes. Though the KOH has higher basicity, the poor response could be justified by bigger crystallite sizes, leading to higher resistance in air (see **Figure 4.6: a** and **b**), which in turn led to smaller change in resistance when the sensor was exposed to the target gases.

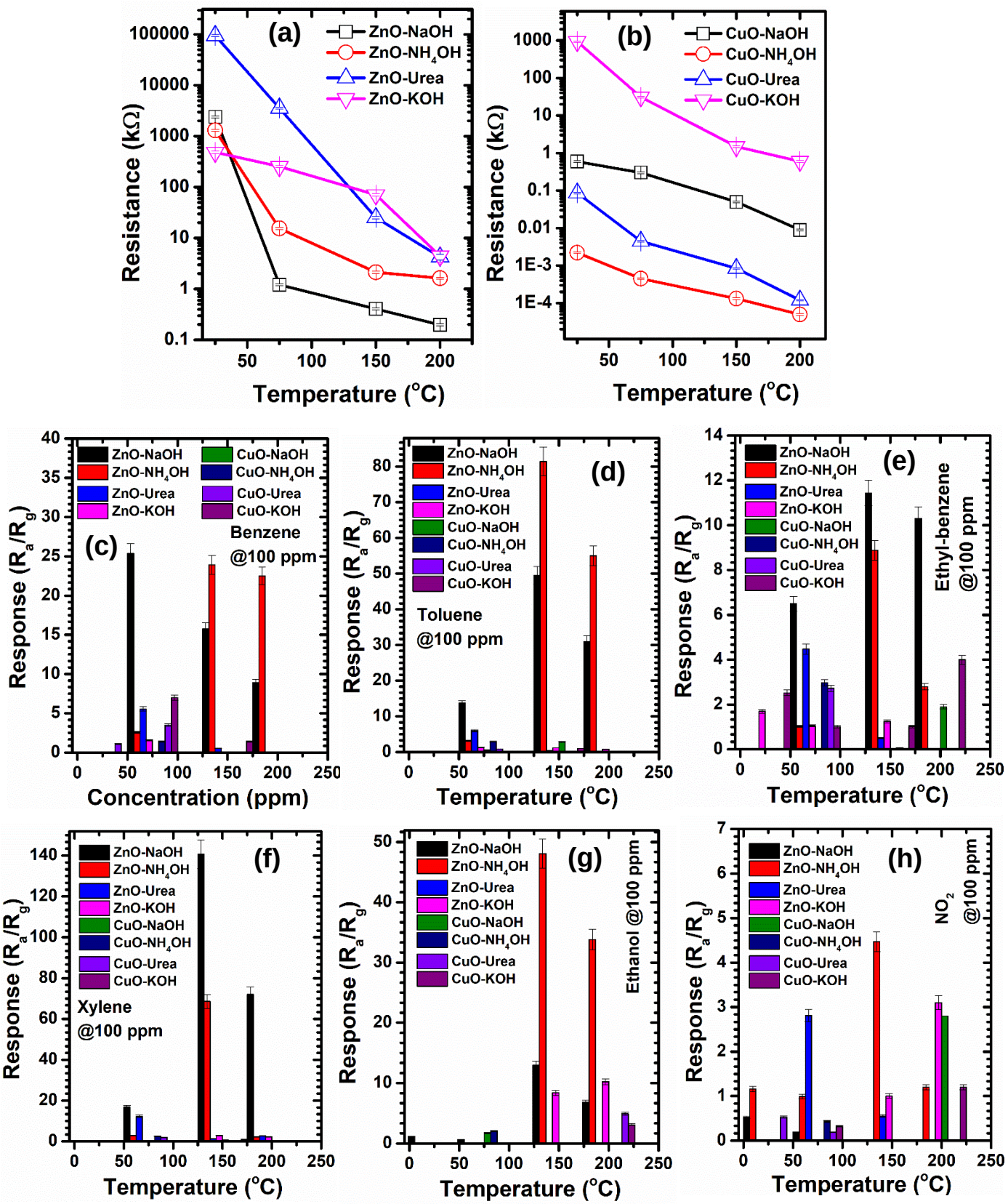

Figure 4.6: R_a versus temperature for (a) ZnO and (b) CuO nanostructures. Response versus temperature for various sensors towards (c) benzene, (d) toluene, (e) ethyl-benzene, (f) xylene, (g) ethanol and (h) NO_2 gas.

The sensor responses versus the concentration of BTEX, ethanol and NO_2 are shown in **Figure 4.7**. The ZnO-NaOH sensor displayed an improved responses towards benzene vapor at 75 °C, and its response at 5 ppm was roughly 2.5. As listed in **Table 4.1**, the Occupational Safety and Health Administration (OSHA) Standards have stated that the employer should ensure that the employees are not exposed to more than Allowed Limits of Exposure (ALE), not exposed to a concentration of more than the Time Weighted Average (TWA) for more than 8 hours and for 15 minutes for Short Term Limits of Exposure (STLE), NIOSH specified Recommended Limits of Exposure (RLE) for both TWA and STLE and Fatal Exposure Levels (FEL) of the gases. On the other hand, American Conference of Governmental Industrial Hygienists (ACGIH), has also identified Minimum Limit Levels (MLL) of TWA and STLE for all the gases, see **Table 4.1 [49]**. Thus, the current results fit well with the recommendations of OSHA. While the sensor showed such a high response at 5 ppm, nonetheless its response still increased with gas concentrations up to 100 ppm, showing a response of 25. Nonetheless, at an elevated operational temperature of 150 °C, the sensor exhibited a superior response of 142 towards 100 ppm of xylene (**Figure 4.7: b**). As shown in **Figure 4.7: b**, the ZnO-NaOH-based sensor response increased exponentially, indicating no saturation. The detected concentration of 100 ppm for xylene is in line with the permissible exposure limit (PEL) acknowledged by the OSHA, NIOSH and ACGIH, respectively **[50]**.

Table 4.1: Summary of recommended limits by various institutions **[49, 50]**.

		Benzene	Toluene	Ethylbenzene	Xylene
OSHA	TWA (ppm)	1	200	100	100
(ALE)	STLE (ppm)	5	500	125	150
NIOSH	TWA (ppm)	0.1	100	100	100
(RLE)	STLE (ppm)	1	150	125	150
ACGIH	TWA (ppm)	0.5	50	100	100
(MLV)	STLE (ppm)	2.5	Unsubstantiated	125	150

Figure 4.7: d and **e** presents the real-time resistance plots of ZnO prepared using various bases tested for benzene and xylene at 75 °C and 150 °C, respectively. While that in **Figure 4.7: f** is the resistance plot of various ZnO sensors tested towards xylene at 200 °C. A clear response and recovery curves were observed for all the sensors towards benzene and xylene, without disclosing any sensor poisoning. Though, by comparing the change in resistance for the sensors tested towards xylene at 150 and 200 °C, it is observed that the change in resistance at 200 °C is smaller compared to that at 150 °C, justifying the optimum temperature as 150 °C. For a sensor to be considered for actual applications, the response and recovery times are some of the vital parameters to be considered. Thus, the response and recovery times, which are considered as the time essential to increasing the response variation to 90% of the maximum value and time that is essential for decreasing the complete response variation to 10%, respectively. **Figure 4.7: e** and **f** show the t_{res} and t_{rec} of the sensor towards benzene and xylene vapour. The ZnO-NaOH based sensor shows a t_{res} and

t_{rec} of 33.1 and 141.1 s towards 5 ppm and 55.7 s and 51.3 s at 100 ppm benzene, respectively.

When the ZnO-NaOH-based sensor is exposed to 100 ppm xylene, the t_{res} and t_{rec} of 88.7 s and 19.0 s are observed, respectively. It is evident from **Figure 4.7: a** and **b** that at higher concentrations of both benzene and xylene, t_{rec} is shorter. The sensitivity values of the sensors towards benzene and xylene were extracted by fitting a linear plot in **Figure 4.7: a** and **b**, see **figure 4.7: c** for better details. Amongst the sensors, the ZnO-NaOH-based sensor showed a greater sensitivity of 0.178 ppm^{-1} towards benzene at 75 °C, when compared to 0.023 ppm^{-1}, 0.054 ppm^{-1}, 0.013 ppm^{-1}, 0.036 and 0.064 ppm^{-1} for ZnO-NH_4OH, ZnO-Urea, CuO-NH_4OH, CuO-Urea and CuO-KOH, respectively. In addition, when the sensors were exposed to xylene at 150 °C, a superior sensitivity of 1.210 ppm^{-1}, towards xylene was observed, which was higher than that of ZnO-NH_4OH (0.610 ppm^{-1}), ZnO-urea (0.012 ppm^{-1}), CuO-NaOH (0.005 ppm^{-1}), and CuO-urea (0.002 ppm^{-1}) and CuO-KOH (0.0167 ppm^{-1}). Thus, the ZnO-NaOH-based sensor had a remarkable sensitivity towards xylene compared to benzene.

Additionally, the limit of detection was calculated using the following formula: $LoD = 3\left(\frac{RMS_{noise}}{Slope}\right)$, where RMS_{noise} is considered as the root mean square, which was obtained from the fluctuations in the response of the sensor prior to the target gas (i.e., baseline). To calculate the RMS_{noise}, we considered 30 points as provided by the following expression **[6]**: $RMS_{noise} = \sqrt{\sum_i {(x_i - x)^2}/{N}}$, where x_i, x and *N* correspond to the experimental data, average value of the data points and total number of data points, respectively.

Clearly, the ZnO-NaOH sensor showed the minimal LoD of 0.018 (18 ppb) for xylene and 1.597 ppm for benzene. As a result, this validates the substantial role of V_O by improving the sensing characteristics. This nominal LoD is smaller than 5 ppm, which cannot be experimentally detected due to the limitations of the sensor measurement system. The reduced LoD may be utilized to detect xylene at minimal ppb levels. Thus, the findings show that our ZnO-NaOH-based sensor illustrates a potential outlook for benzene and xylene detection for quality monitoring in indoor environments.

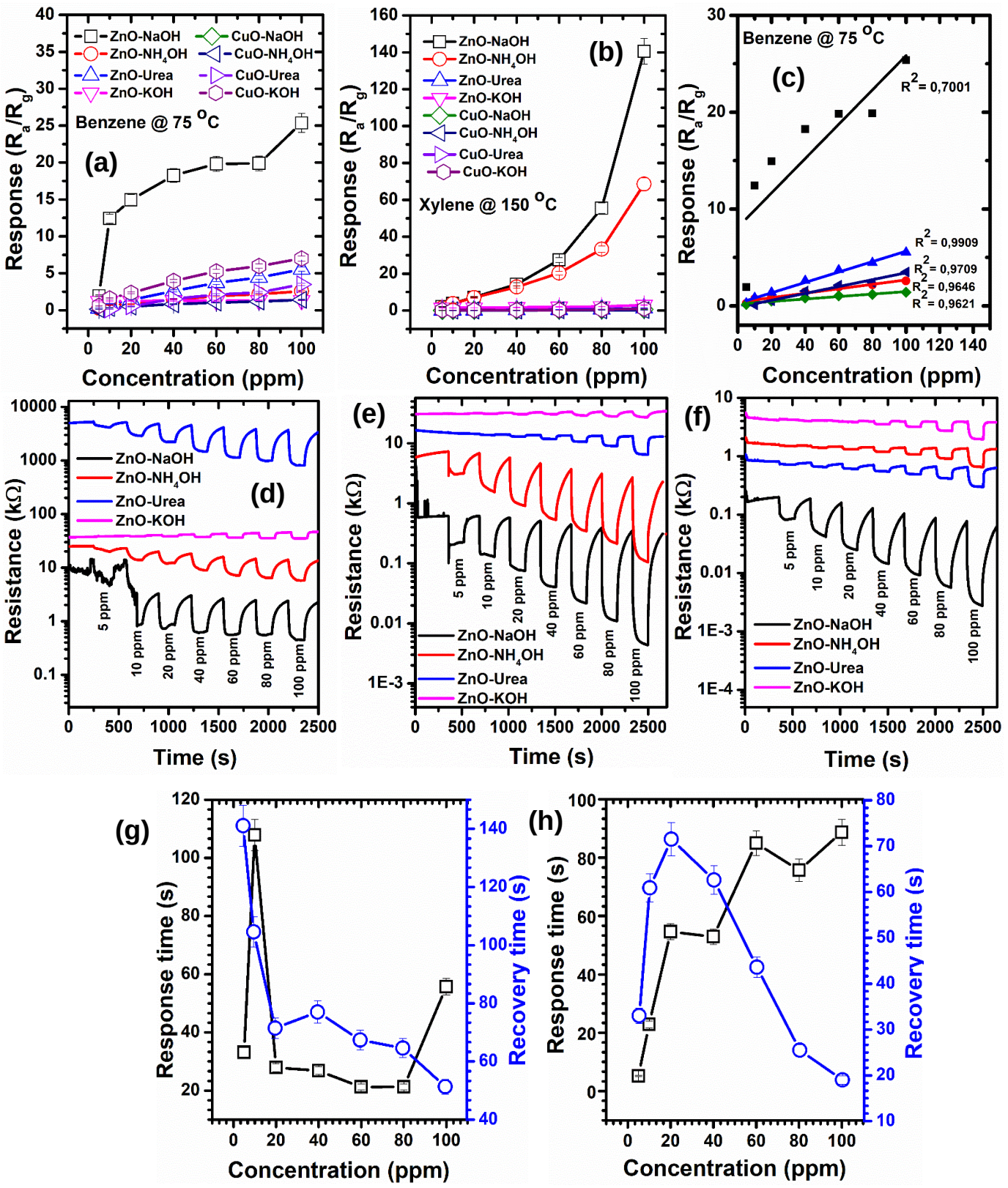

Figure 4.7: Response versus gas concentration of (a) benzene at 75 °C, (b) xylene at 150 °C, (c) sensitivity plot of benzene at 75 °C. Real-time resistance plots of different sensors towards (d) benzene at 75 °C, (e) xylene at 150 °C and (f) 200 °C. Response time and recovery times of (g) benzene at 75 °C, (h) xylene at 150 °C for ZnO-NaOH-based sensor.

Selectivity is one of the most vital sensor parameters for real time applications. It is well known that the chemical inertia of BTEX is a significant challenge for its selective detection. Thus, in the current work, the dual-mode selectivity of ZnO-NaOH towards benzene and xylene in the presence of other interfering gases at 75 °C and 150 °C was realized as shown in **Figure 4.8: a** and **b**. As presented in **Figure 4.8: a**, at the operating temperature of 75 °C, ZnO-NaOH shows a higher response to benzene, which is roughly twice that of the other sensors and gases. The CuO-KOH-based sensor also showed a response of 7 towards benzene, which was however lower than that of ZnO-NaOH-based sensor.

Furthermore, the radar plot in **Figure 4.8: b** shows that when the sensors were tested at 150 °C, the ZnO-NaOH-based sensor exhibited a higher response towards xylene vapour. Its response was also almost two times higher compared to other gases, where the possible interference gas could be toluene on both occasions. Furthermore, though ZnO-urea showed a response towards xylene, nonetheless its response was smaller compared to that of ZnO-NaOH-based sensor towards xylene detection.

Thus, to validate the possible interference of toluene in the detection of either benzene or xylene, cross-selectivity calculations were performed using the following expression: $K = S_{benzene}/S_0$ **[51]**, where K is the selectivity coefficient and $S_{benzene}$ is linked to ZnO-NaOH-based sensor response and S_0 is associated to the response of the interfering gases (i.e., toluene, ethylbenzene, xylene, ethanol and NO_2). Moreover, for the xylene, the $K = S_{xylene}/S_0$ over the interference gases (i.e., benzene, toluene, ethylbenzene, ethanol and NO_2). **Figure 4.8: c** and **d** show cross-sensitivity values for benzene and xylene, respectively. The higher 'K' value denotes the superior selectivity of the ZnO-NaOH towards benzene at 75 °C and xylene at 150 °C.

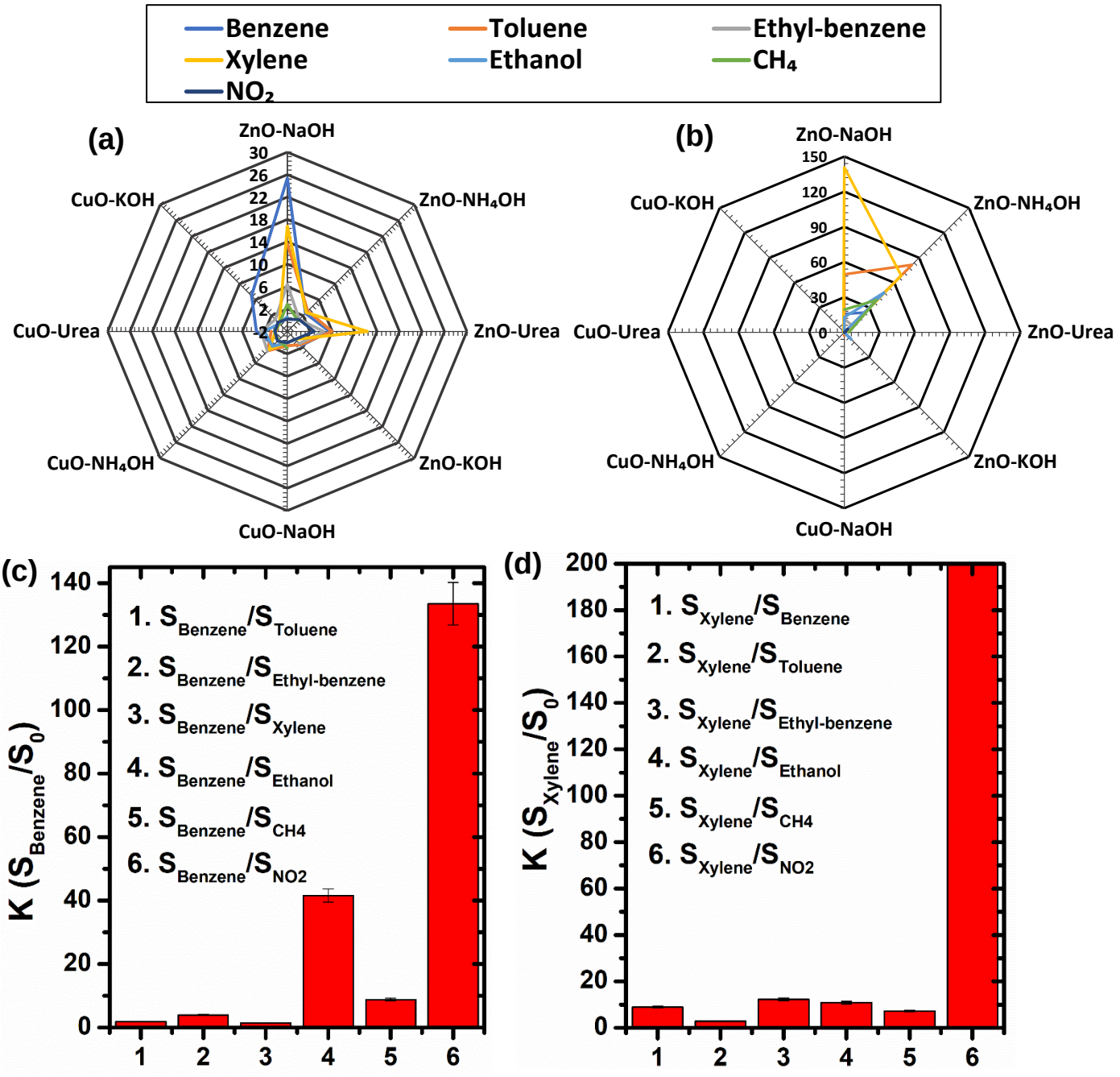

Figure 4.8: Radar selectivity of various sensors towards different gases at (a) 75 °C and (b) 150 °C. cross-sensitivity values of benzene and xylene over the interference gases at (c) 75 °C and (d) 150 °C, respectively.

Table 4.2 shows a comparability between the results of the current work on xylene sensing with that published in the literature. As shown in **Table 4.2**, several studies have reported good selectivity towards xylene, although at higher operational temperature in comparison to our current results. Besides, despite the voluminous work on the selectivity of xylene, limited studies have reported selectivity utilizing a single SMO gas sensor, as most studies have focused on either using heterostructure or doped materials. However, their sensing response values were lower than those reported in the current study. Ren et al. **[24]** has prepared 3 mol. % CuO/SnO_2 composites for detection of 100 ppm xylene at elevated temperature of 280 °C, displaying a response of 13. Additionally, Gao et al. **[52]** reported a response value of 22 towards 100 ppm xylene using 3 at. % Sn-doped NiO based sensor at operational temperature of 225 °C. Guo et al. **[53]** disclosed a remarkable response of 101 towards 100 ppm xylene at 175 °C. Their response was roughly 16.4 times more than that of pure Co_3O_4. Thus, according to **Table 4.2**, our sensor response is approximately 0.71 higher of other sensors, or even two times more to other sensors reported in the literature.

Figure 4.9: a and **b** shows the comparability between the results of the current study on the cross selectivity toward benzene and xylene in the presence of other interference gases. Our ZnO-NaOH-based sensor has a comparable cross-selectivity toward benzene in the presence of other gases. Additionally, when comparing our ZnO-NaOH sensor with the other sensors in the literature tested towards xylene, our sensor also shows a superior cross-selectivity. Therefore, our findings show that proper design and tuning of nanostructures utilizing a proper base has a potential influence on the selectivity of BTEX.

Table 4.2: Summary of various sensors in the literature used to detect xylene vapour.

Sensing element	Concentration (ppm)	T_{res}/T_{rec} (s)	Response	Temp. (°C)	Refs.
ZnO-NaOH	**100**	**88/19**	**142**	**150**	**This work**
ZnO-nanorods	100	6/12	9.6	150	**[11]**
Co-doped ZnO nanoparticles	100	75/55	76%	100	**[14]**
Boron nitride quantum dots decorated ZnO nanoplates	100	20/20	3.46	370	**[18]**
3 mol.%CuO/ZnO	100		13	280	**[24]**
3 at.% Sn-doped NiO	100	298/223	20.2	225	**[52]**
TiO_2-Nanowires	100	45/95	37	125	**[3]**
SnO_2-Co_3O_4 nanocomposites	100	204/367	101	175	**[53]**
SnO_2/Co_3O_4 nanorods	100	98/107	47.8	280	**[54]**
Flower-like Co_3O_4 structures	100	131/ > 250	79.8	150	**[55]**
Co3O4 nanocubes	100		6.45	200	**[56]**
Hierarchical $NiCo_2O_4$	100	20/9	9.2	220	**[57]**
Porous coral-like $NiCo_2O_4$ nanospheres	100	30/30	16.4	260	**[58]**

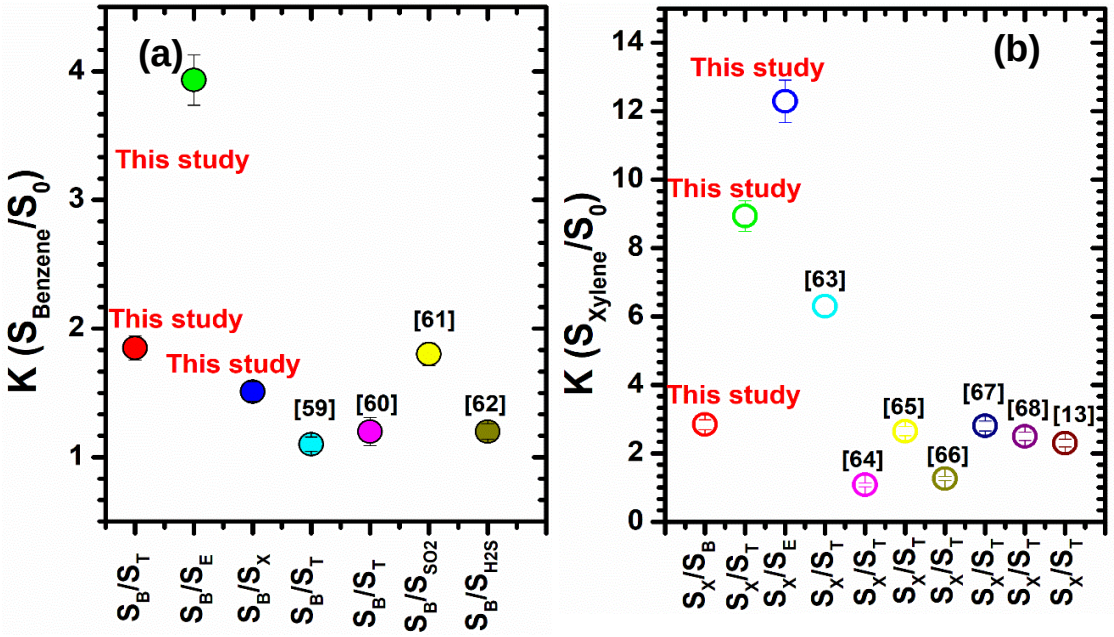

Figure 4.9: Comparisons of the cross-selectivity towards (a) benzene and (b) xylene in the presence of other interference gases. Note that B, T, E and X correspond to benzene, toluene, ethylbenzene, and xylene, respectively.

Long-term operational stability and repeatability are among the most vital parameters of gas sensors for real-time applications. Generally, the stability is associated with the service life of the SMO sensor. **Figure 4.10: a** shows the real-time resistance plot versus number of days. As demonstrated in **Figure 4.10: a** and **Figure 4.10: b**, when the sensor was stored for more than 90 days, the resistance increased strongly, denoting a possible poisoning. **Figure 4.10: c** displays the response versus number of days (1 to 547 days), which shows that when the sensor is stored for 30 days, a response dropped by roughly 4%, denoting the excellent stability. Nonetheless, increasing the storage time from 60 to 557 days, the response decreased by 82 and 97 % after 150- and 547-days storage, respectively.

For practical use, sensors should be able to operate in the presence of humidity. Thus, **Figure 4.10: g** illustrates the real-time resistance of the ZnO-NaOH-based sensor

exposed towards various concentrations of xylene in the presence of 60 % RH. As depicted in the Figure, the change in sensor resistance is limited in the presence of RH and this is confirmed in **Figure 4.10: h**, where the sensor response reduces with an increase in RH percentage from 40 to 60 % due to possible sensor poisoning.

Generally, a sensor that displays significant deviations in response over consecutive cycles, can be unsuccessful in precisely sensing a particular gas. Though the sensor response dropped after 547 days storage, we further investigated the repeatability and long-term operational analyses after the sensor was stored for 547 days. **Figure 4.10: d** illustrates the repeatability and long-term operational stability of the ZnO-NaOH-based sensor over 10 cycles (see magnified **Figure 4.10: e**) towards xylene for 5 min gas in and 5 min gas out and these analyses were performed twice. In addition, in the same analyses, the exposure time was also investigated for 5, 10, 30 and 60 min towards xylene, as shown in a magnified plot of **Figure 4.10: f**. These analyses were repeated to determine if there was any drift, and which was not observed in either analysis. The entire analyses took more than 80 000 s (22, 22 hours), demonstrating a reasonable long-term operational stability. These findings indicate that the current sensor is still able to demonstrate excellent reliability and high stability for long-term operations, though its response reduced strongly than the initial response of 142.

Nonetheless, the sensor resistance of the 10 cycles in **Figure 4.10: d** and magnified plot in **Figure 4.10: e** shows some slight drift, which could be associated with the interaction between the surface of the ZnO-NaOH based sensor and the xylene gas, where some of the residuals of xylene could have remained on the ZnO-NaOH-based sensor surface. Additionally, the operational temperature could also be affecting the sensing performance. For instance, if the operational temperature is quite low, then

the rate of reaction of the target gas on the sensor surface will be too slow to provide a stable response. Therefore, the steady state response was not achieved due to possibly low operational temperature, leading to low reaction rate.

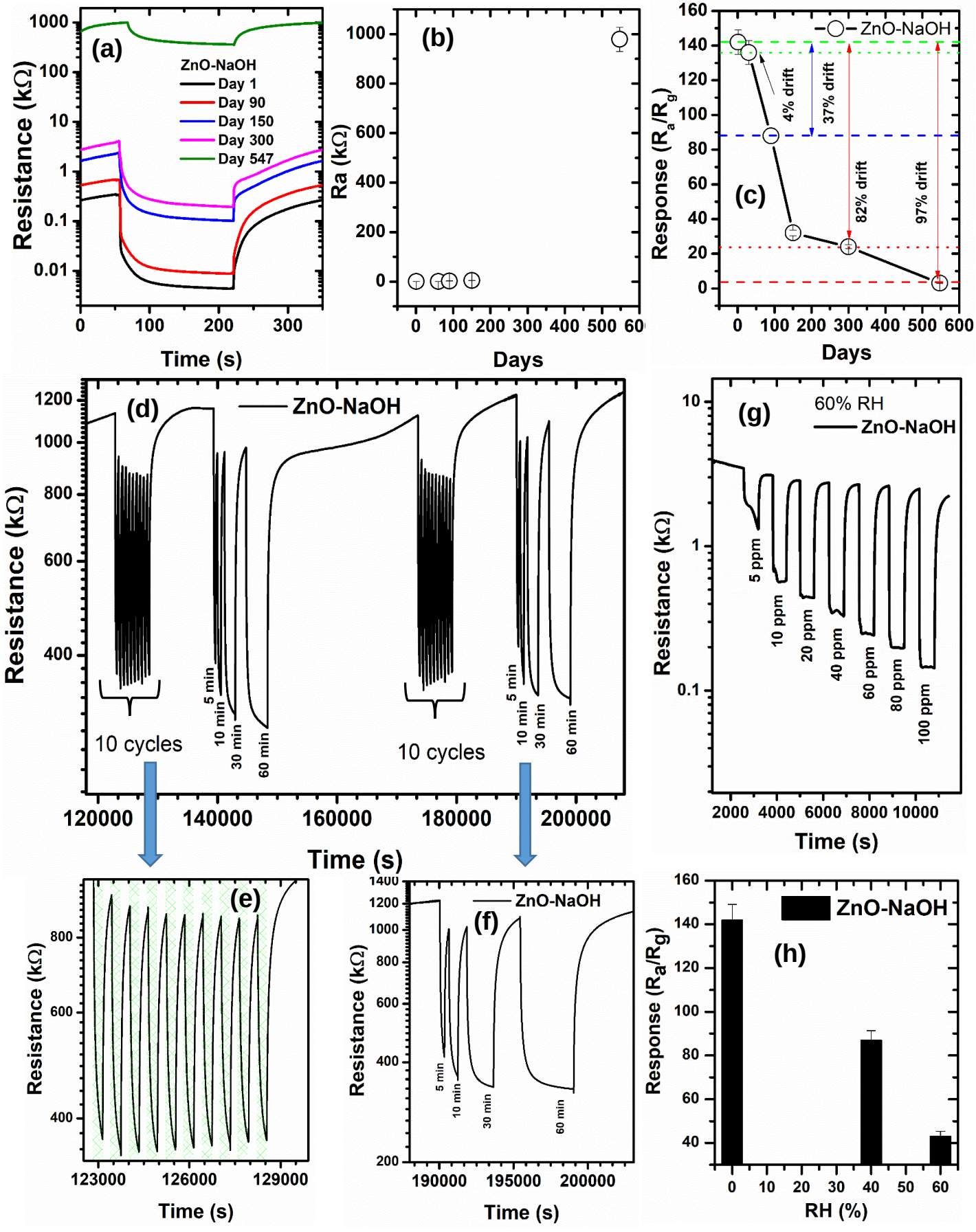
(a)
ZnO-NaOH
Day 1
Day 90
Day 150
Day 300
Day 547
Resistance (kΩ)
Time (s)
(b)
Ra (kΩ)
Days
(c)
ZnO-NaOH
4% drift
37% drift
82% drift
97% drift
Response (Ra/Rg)
Days
(d)
ZnO-NaOH
Resistance (kΩ)
10 cycles
5 min
10 min
30 min
60 min
10 cycles
5 min
10 min
30 min
60 min
Time (s)
(e)
Resistance (kΩ)
Time (s)
(f)
ZnO-NaOH
Resistance (kΩ)
5 min
10 min
30 min
60 min
Time (s)
(g)
60% RH
ZnO-NaOH
Resistance (kΩ)
5 ppm
10 ppm
20 ppm
40 ppm
60 ppm
80 ppm
100 ppm
Time (s)
(h)
ZnO-NaOH
Response (Ra/Rg)
RH (%)

Figure 4.10: (a) Real-time resistance plot against number of days, (b) response against number of days, (c) R_a versus number of days, (d) repeatability and long-term operation stability of ZnO-NaOH based sensor towards xylene 100 ppm vapour at 150 °C. Note: (e) and (f) correspond to magnified plots of Figure 4.10: d. Note (g) and (h) corresponds to response towards xylene in the presence of 60 %RH and response versus RH %, respectively.

4.6.5. GAS SENSING MECHANISM TOWARDS BENZENE AND XYLENE VAPOURS

It is generally known that ZnO is an n-type SMO sensing material. Some of the main influences associated to the gas sensing characteristics are the interaction of the adsorbed oxygen and the analyte gas, which leads to a change in the sensor resistance. When the sensor is exposed to air, oxygen molecules adsorbed onto the surface of the sensing material become ionized to O_2^- (<150 ˚C), O^- (>150 ˚C) by extracting electrons from the conduction band (E_C) of the sensing layer **[12, 69]** (see reactions (**20-22**) and **Scheme 4.2**). Nonetheless, upon exposing the sensor to benzene gas, it reacts with chemisorbed oxygen (O_2^- at an operational temperature of 75 °C), see reaction (**3**) and **Scheme 4.2: a** and **b**. Thus, electrons are released back to the E_C of ZnO, leading to a decrease in the sensor resistance **[12, 69]**.

$$O_2(\text{gas}) \rightarrow O_2(\text{ads}) \quad \textbf{(20)}$$

$$O_2(\text{ads}) + e^- \rightarrow O_2^-(\text{ads}) \quad \textbf{(21)}$$

$$2C_6H_6 + 15O_2^-(\text{ads}) \rightarrow 12CO_2 + 6H_2O + 15e^- \quad \textbf{(22)}$$

Nevertheless, if the sensor is exposed to xylene, it will react with chemisorbed oxygen species (O^- at an operational temperature of 150 °C), see **Scheme 4.2: c-d**. Thus, the

electrons are released back to the E_C of ZnO (see reactions **23-24**), leading to reduced sensor resistance **[3, 12]**.

$$(C_6H_4CH_3CH_3)_{gas} \longleftrightarrow (C_6H_4CH_3CH_3)_{ads} \quad \textbf{(23)}$$

$$(C_6H_4CH_3CH_3)_{ads} + 21O^- \longrightarrow 8CO_2 + 5H_2O_{(gas)} + 21e^- \quad \textbf{(24)}$$

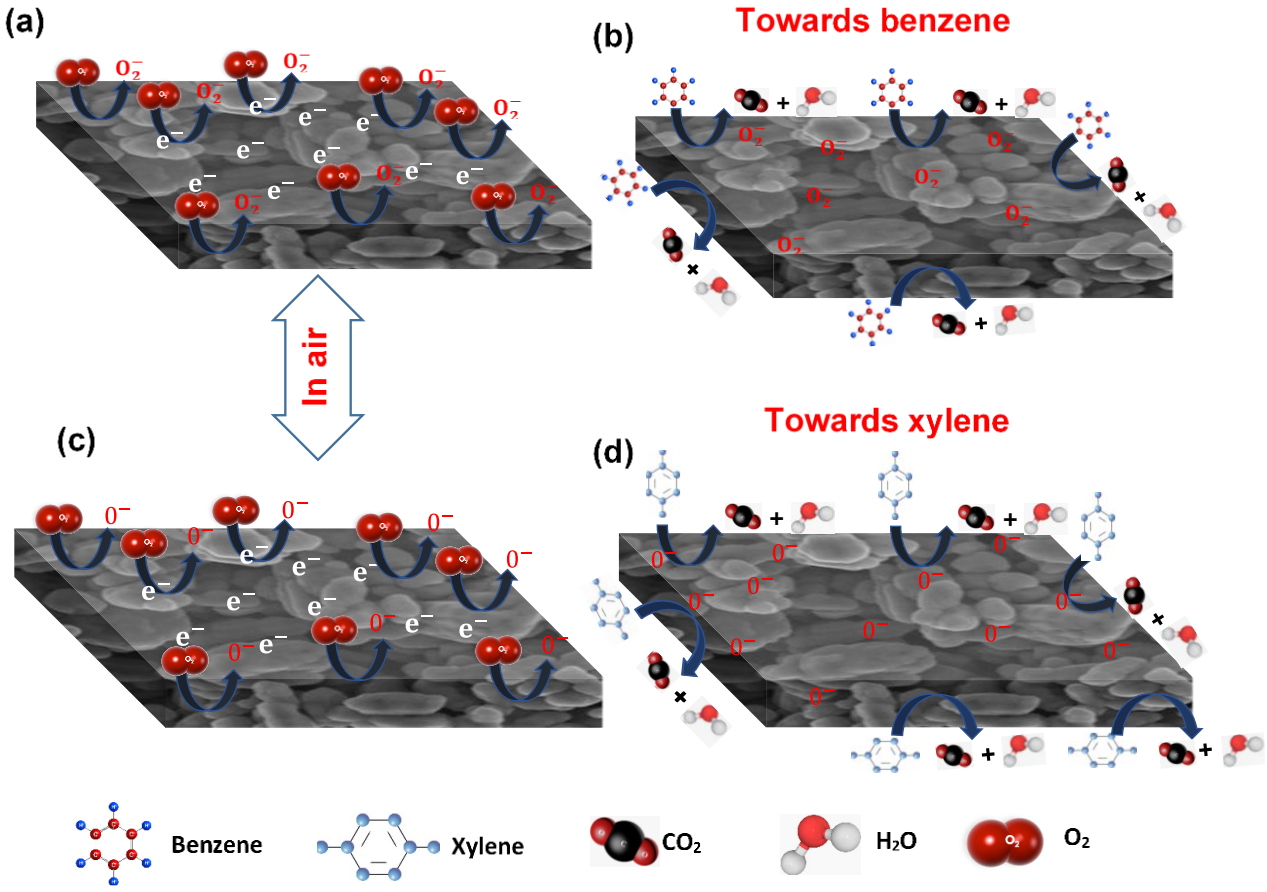

Scheme 4.2: Sensing mechanism of ZnO-NaOH-based sensor towards (a-b) Benzene at 75 °C, and (c-d) xylene at 150 °C.

Table 4.3 shows a summary of crystallite sizes, PL ratio (Vis/UV_O), UV-vis optical band gaps and number of spins, measured at room temperature. Thus, based on **Table 4.3**, the superior sensing characteristics of ZnO-NaOH towards benzene and xylene at 75

and 150 °C, respectively, could be attributed to smaller crystallite sizes, leading to higher PL ratio (i.e., surface defects, associated to V_O), which result into a higher sensing sensitivity **[35]**. Moreover, higher number of spins (i.e., paramagnetic defects, V_O), which are associated to amount of electron reaching the conduction band **[70]** of ZnO are observed for the ZnO-NaOH compared to its counterparts, justifying the observed improved sensing performance. Additionally, the ZnO-NaOH disclosed smaller bandgap compared to other ZnO materials. Smaller band gap denotes that, electrons can be more inclined to transition and can generate more photogenerated carriers that will result to the enhanced variation in resistance and as well as decrease in working temperature. Therefore, this validates the observed improved sensing characteristics for the ZnO-NaOH-based sensor.

Table 4.3: Summary of crystallite sizes, band gap, PL ratio and number of spins.

Materials	Crystallites sizes (nm)	Band gap (eV)	PL ratio	Number of Spins ($\times 10^7$)
ZnO-NaOH	21.0	3.09	1.02	1.11
ZnO-Urea	26.6	3.12	0.46	0.97
ZnO-NH_4OH	24.6	3.11	0.41	0.85
ZnO-KOH	38.3	3.13	0.45	0.44
CuO-NaOH	13.4	1.55	0.95	0.53
CuO-Urea	23.9	1.61	0.91	0.17
CuO-NH_4OH	14.8	1.58	0.64	0.28
CuO-KOH	19.9	1.60	0.76	0.22

For instance, at an *in-situ* temperature of 150 °C for both PL and EPR, which was correlated to the sensing temperature of 150 °C, the ZnO-NaOH based sensor disclosed a higher relative number of defects compared to other ZnO based sensors.

To validate these findings, we compared the response of the best performing sensors (i.e., ZnO-NaOH and ZnO-NH_4OH) towards 100 ppm xylene, based on their sensing performance with the PL ratio and number of spins at the in-situ temperature of 150 °C for both PL, and EPR, as shown in **Figure 4.11**. Remarkably, ZnO-NaOH shows a higher PL ratio and number of spins in comparison to ZnO-NH_4OH, which clearly correlates with the observed higher sensing response **[70]**.

This observation clearly confirms that among the used bases, NaOH has a strong influence on the gas-sensing properties of ZnO-based sensors, followed by NH_4OH and urea. For instance, studies have shown that NaOH is a proper base for creation of porous structures, which leads to improved gas adsorption/desorption, in turn leading to a superior sensing performance **[38]**. Though the KOH has a strong pH or basicity compared to NaOH, thus this clearly shows that a specific pH of basicity affects the structure of the nanostructures. Besides, ZnO structures prepared using KOH showed more selectivity towards methanol or ethanol instead of BTEX **[71-74]**. Furthermore, smaller crystallite sizes were observed when using NaOH, which led to a higher V_O and thus a higher sensing performance was observed. While the other bases showed bigger crystallite sizes leading to low surface defects, as a result, poor sensing performance was observed. This observation is in line with that of previous studies **[35, 42, 70,** and **75]**. Additionally, Motaung et al. **[26]** used various bases (LiOH, KOH, NaOH and NH_4OH) to probe the surface defects and ferromagnetic magnetic properties of ZnO. They observed that among the used bases, NaOH showed improved surface defects, leading to higher ferromagnetic magnetic properties.

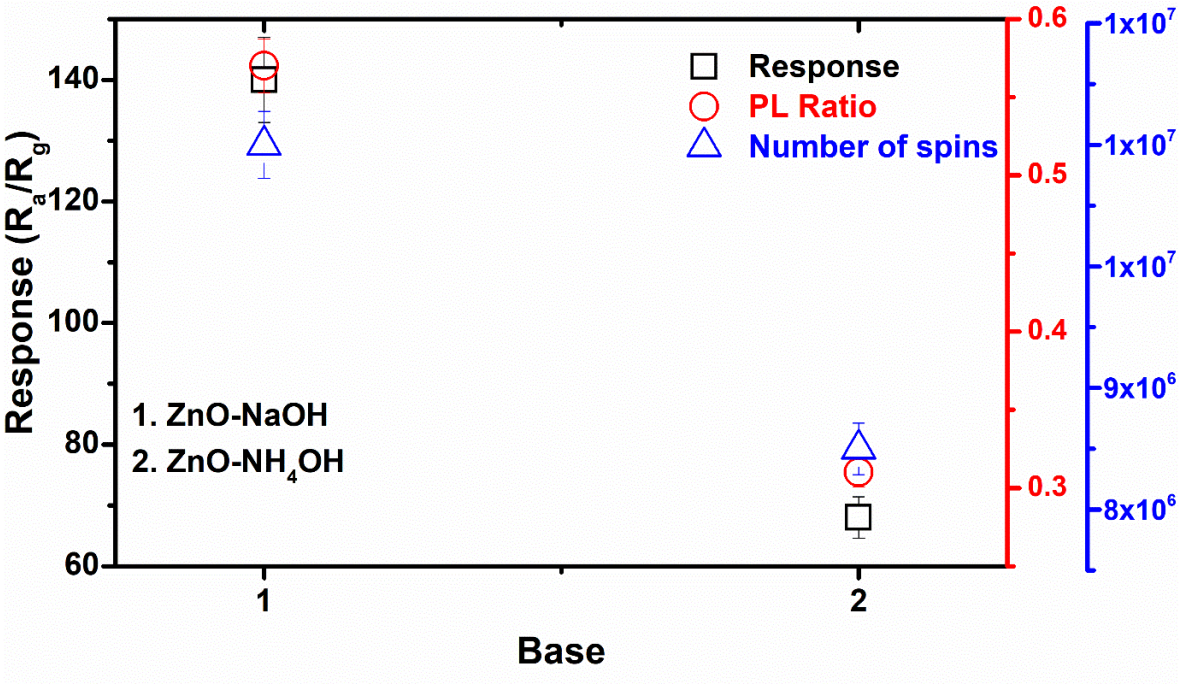

Figure 4.11: Response, PL and number of spins versus reaction base.

The detection of benzene at low operational temperature is quite unusual, because benzene is more stable than toluene, xylene and ethylbenzene. Thus, the selectivity of ZnO-NaOH towards benzene at 75 °C, could be due to the diversity of ZnO and benzene bond energies and molecular structures. The H-O bond strengthens the arrangement of the benzene molecule and the nanostructure. The exceptional bonding principle leads to enhanced selectivity toward benzene **[12, 76]**. The selectivity towards xylene could probably be due to the higher binding energy of xylene and the higher operational temperature (150 °C), which allows for better adsorption of xylene **[6]**. In addition, the selective detection of xylene could also be due to the change in enthalpy of dehydrogenation of VOCs analytes. For instance, refs **[77, 78]** display the standard enthalpies of the original molecules (HO) and dehydroradical

(HR), where the change in enthalpy of dehydrogenation (H = HR−HO) was estimated. The benzene discloses an enthalpy change of the dehydrogenation of 255.4 kJ/mol **[77, 78]**. While the toluene and xylene show the similar enthalpy changes of the dehydrogenation of about 157.4 and 157.8 J/mol **[75, 78]**, respectively. Consequently, the superior selectivity towards xylene compared to toluene may be due to the xylene molecule containing two more methyl groups. Furthermore, according to Russell's report, the oxidation rate of xylene at 90 °C (0.0039 mol h^{-1}) is superior to that of toluene (0.0013 mol h^{-1}) **[79]**, which may explain the superior selectivity observed for xylene.

REFERENCES

1. C. Zhang, G. Kwak, Y.J. Lee, K.W. Jun, R. Gao, H.G. Park, S. Kim, J.E. Min, S.C. Kang, G. Guan, Light hydrocarbons to BTEX aromatics over Zn-modified hierarchical ZSM-5 combined with enhanced catalytic activity and stability. Microporous Mesoporous Mater. 284 (2019) pp. 316-326.

2. J.G. Thangamani, S.K. Khadheer Pasha, Hydrothermal synthesis of copper (II) (oxide-nanoparticles with highly enhanced BTEX gas sensing performance using chemiresistive sensor, Chemosphere 277 (2021) pp. 130237.

3. A. Akhtar, W. Di, J. Liu, C. Fu, J. Wang, X. Chu, The detection of ethanol vapors based on a p-type gas sensor fabricated from heterojunction MoS_2–$NiCo_2O_4$, Materials Chemistry and Physics, 282 (2022) pp. 125-964.

4. G. Yurko, J. Roostaei, T. Dittrich, L. Xu, M. Ewing, Y. Zhang, G. Shreve, Realtime sensor response characteristics of 3 commercial metal oxide sensors for detection of BTEX and chlorinated aliphatic hydrocarbon organic vapors. Chemosensors 7 (2019) pp.40.

5. R. Nasreddine, Person, V., Serra, C.A., Le Calve, S. Development of a novel portable miniaturized GC for near real-time low level detection of BTEX. Sensor. Actuator. B Chem. 224 (2016) pp. 159-169.

6. Z.P. Tshabalala, T.P. Mokoena, M. Jozela, J. Tshilongo, T.K. Hillie, H.C. Swart, D.E. Motaung, TiO_2 Nanowires for Humidity-Stable Gas Sensors for Toluene and Xylene, ACS Applied Nano Materials, 4 (1) (2021) pp. 702-716.

7. A. Wei, L. Pan, W. Huang, Recent progress in the ZnO nanostructure-based sensors, Mater. Sci. Eng. B, 176 (2011) pp. 1409–1421.

8. J. Sithole, B.D. Ngom, S. Khamlich, E. Manikanadan, N. Manyala, M.L. Saboungi, D. Knoessen, R. Nemutudi, M. Maaza, Appl. Surf. Sci., 258 (2012) pp. 7839–7843.

9. D. Papadaki, S. Foteinis, G.H. Mhlongo, S.S. Nkosi, D.E. Motaung, S.S. Ray, T. Tsoutsos, G. Kiriakidis, Life cycle assessment of facile microwave-assisted zinc oxide (ZnO) nanostructures, Science of the Total Environment 586 (2017) pp. 566–575.

10. V. Gurylev, T.P. Perng, Defect engineering of ZnO: Review on oxygen and zinc vacancies, Journal of the European Ceramic Society, 41 (2021) pp. 4977–4996.

11. Y. Cao, P. Hu, W. Pan, Y. Huang, D. Ji, Methanal and xylene sensors based on ZnO nanoparticles and nanorods prepared by room-temperature solid-state chemical reaction, Sensors and Actuators B, 134 (2008) pp. 462–466.

12. A. Mirzaei, J.-H. Kim, H.W. Kim, S.S. Kim, Resistive-based gas sensors for detection of benzene, toluene and xylene (BTX) gases: a review, J. Mater. Chem. C, 6 (2018) pp. 4342-4370.

13. H.-S. Woo, C.-H. Kwak, J.-H. Chung, J.-H. Lee, Co-Doped Branched ZnO Nanowires for Ultraselective and Sensitive Detection of Xylene, ACS Appl. Mater. Interfaces, 6 (2014) pp. 22553−22560.

14. U. Godavartia, V.D. Mote, M.V.R Reddy, P. Nagarajua, Y.V. Kumard, K.T. Dasarie, M.P. Dasari, Precipitated cobalt doped ZnO nanoparticles with enhanced low temperature xylene sensing properties, Physica B: Condensed Matter, 553 (2019) pp. 151–160.

15. Z.U. Abideen, J.-H. Kim, A. Mirzaei, H.W. Kim, S.S. Kim, Sensing behavior to ppm-level gases and synergistic sensing mechanism in metal-functionalized rGO-loaded ZnO nanofibers, Sens. Actuators B Chem. 255 (2018) pp. 1884-1896.

16. M. Bonyani, J.K. Lee, G.-J. Sun, S. Lee, T. Ko, C. Lee, Benzene sensing properties and sensing mechanism of Pd-decorated Bi_2O_3-core/ZnO-shell nanorods, Thin Solid Films 636 (2017) pp. 257-266.

17. S.C. Hernandez, C.M. Hangarter, A. Mulchandani, N.V. Myung, Selective recognition of xylene isomers using ZnO–SWNTs hybrid gas sensors, Analyst, 137 (2012) pp. 25-49.

18. S.P. Choudhury, Z. Feng, C. Gao, X. Ma, J. Zhan, F. Jia, BN quantum dots decorated ZnO nanoplates sensor for enhanced detection of BTEX gases, Journal of Alloys and Compounds 815 (2020) pp.152-376.

19. J.S. Yang, W.Y. Jung, G.D. Lee, S.S. Park, E.D. Jeong, H.G. Kim, S.S. Hong, Catalytic combustion of benzene over metal oxides supported on SBA-15, J. Ind. Eng. Chem. 14 (2008) pp. 779–784.

20. R. Molinari, T. Poerio, P. Argurio, Liquid-phase oxidation of benzene to phenol using CuO catalytic polymeric membranes, Desalination 241 (2009) pp. 22–28.

21. T. Miyahara, H. Kanzaki, R. Hamada, S. Kuroiwa, S. Nishiyama, S. Tsuruya, Liquid-phase oxidation of benzene to phenol by CuO–Al_2O_3 catalysts prepared by co-precipitation method, J. Mol. Catal. A: Chem. 176 (2001) pp. 141–150.

22. Z.Y. Fei, P. Lu, X.Z. Feng, B. Sun, W.J. Ji, Geometrical effect of CuO nanostructures on catalytic benzene combustion, Catal. Sci. Technol. 2 (2012) pp. 1705–1710.

23. H.C. Genuino, S. Dharmarathna, E.C. Njagi, M.C. Mei, S.L. Sui, Gas-phase total oxidation of benzene, toluene, ethylbenzene, and xylenes using shape-selective manganese oxide and copper manganese oxide catalysts, J. Phys. Chem. C 116 (2012) pp. 12066–12078.

24. F. Ren, L. Gao, Y. Yuan, Y. Zhang, A. Alqrni, O.M. Al-Dossary, J. Xu, Enhanced BTEX gas-sensing performance of CuO/SnO_2 composite, Sensors and Actuators B 223 (2016) pp. 914–920.

25. Mohammad Vaseem, Ahmad Umar, Yoon-Bong Hahn, ZnO Nanoparticles: Growth, Properties, and Applications, Metal Oxide Nanostructures and Their Applications, 5: (2010) pp. 1–36.

26. D.E. Motaung, G.H. Mhlongo, S.S. Nkosi, G.F. Malgas, B.W. Mwakikunga, E. Coetsee, H.C. Swart, H.M.I. Abdallah, T. Moyo, S.S. Ray, Shape-Selective Dependence of Room Temperature Ferromagnetism Induced by Hierarchical ZnO Nanostructures, ACS Appl. Mater. Interfaces 6 (2014) pp. 8981−8995.

27. S. Xu, Z.L. Wang, One-dimensional ZnO nanostructures: Solution growth and functional properties, Nano Res., 4 (2011) pp. 1013 –1098.

28. E.Y. Shaba, J.O. Jacob, J.O. Tijani, M.A.T. Suleiman, A critical review of synthesis parameters afecting the properties of zinc oxide nanoparticle and its application in wastewater treatment, Applied Water Science 11 (2021) pp.48.

29. J.W. Mullin, Crystallization, Elsevier, London, 4th Edition - May 9, (2001).

30. Myo Thuya Thein, Swee-Yong Pung, Azizan Aziz & Mitsuru Itoh, The role of ammonia hydroxide in the formation of ZnO hexagonal nanodisks using sol–gel technique and their photocatalytic study, Journal of Experimental Nanoscience, 10 (2015) pp. 1068-1081.

31. Pung S-Y, Lee W-P, Aziz A. Kinetic study of organic dye degradation using ZnO particles with different morphologies as a photocatalyst. Int J Inorg Chem. 2012 (2012) pp. 608-183.

32. H. Yang, S.-Q. Ni, X. Jiang, W. Jiang, J. Zhan, *In situ* fabrication of single-crystalline porous ZnO nanoplates on zinc foil to support silver nanoparticles as a stable SERS substrate. Cryst.Eng.Comm 14 (2012) pp. 6023–6028.

33. J. Chang, M.Z. Ahmad, W. Wlodarski, E.R. Waclawik, Self-Assembled 3D ZnO Porous Structures with Exposed Reactive {0001} Facets and Their Enhanced Gas Sensitivity, Sensors 13 (2013) pp. 8445-8460.

34. M. Podlogar, A. Rečnik, G. Yilmazoglu, I. Özgur Özer, M. Mazaj, E. Suvaci, S. Bernik, The role of hydrothermal pathways in the evolution of the morphology of ZnO crystals, Ceramics International, 42 (2016) pp. 15358-15366.

35. A.L. Patterson, The Scherrer formula for x-ray particle size determination, Phys Rev, 56 (1939) pp. 978-982.

36. D.N. Oosthuizen, I. Korditis, H.C. Swart, D.E. Motaung, Facile control of room temperature nitrogen dioxide gas selectivity induced by copper oxide nanoplatelets, Journal of colloid and interface science 560 (2020) pp. 755-768.

37. A.B. Djurisič, Y. H. Leung, K. H. Tam, Y.F. Hsu, L. Ding,´ W. K. Ge, Y.C. Zhong, K.S. Wong, W.K. Chan, H.L. Tam, K.W. Cheah, W.M. Kwok, D.L. Phillips, Defect Emissions in ZnO Nanostructures. Nanotechnology 18 (2007) pp. 095702−095711.

38. M.S. Mamabolo, Z.P. Tshabalala, H.C. Swart, G.E. Mphaphuli, T.K. Hillie, D. E. Motaung, Low Temperature Tunability on CO Selectivity, Low Detection Limit Based on SnO_2-Hollowspheres Induced by Various Bases, Surfaces and Interfaces 31 (2022) pp. 101954.

39. B. Panigrahy, M. Aslam, D. Misra, M. Ghosh, D. Bahadur, Defect-Related Emissions and Magnetization Properties of ZnO Nanorods. Adv. Funct. Mater. 20 (2010) pp. 1161−1165.

40. Y.G. Wang, S.P. Lau, X.H. Zhang, H.H. Hng, H.W. Lee, S.F. Yu, B.K. Tay, Enhancement of Near-Band-Edge Photoluminescence from ZnO Films by Face-to-Face Annealing. J. Cryst. Growth 259 (2003) pp. 335−342.

41. A.V. Dijken, E.A. Meulenkamp, D. Vanmaekelbergh, A. Meijerink, the Luminescence of Nanocrystalline ZnO Particles: The Mechanism of the Ultraviolet and Visible Emission. J. Lumin. 87 (2000) pp. 454−456.

42. O. Mnethu, S.S. Nkosi, I. Kortidis, D.E. Motaung, R.E. Kroon, H.C. Swart, N.G. Ntsasa, J. Tshilongo, T. Moyo, Ultra-sensitive and selective p-xylene gas sensor at low operating temperature utilizing Zn doped CuO nanoplatelets: Insignificant vestiges of oxygen vacancies, Journal of Colloid and Interface Science 576 (2020) pp. 364–375.

43. A. B. Djurisič, W.C.H. Choy, V.A.L. Roy, Y.H. Leung, C.Y. Kwong, K.W. Cheah, T.K. Gundu Rao, W.K. Chan, H. Fei Lui, C. Surya, Photoluminescence and Electron Paramagnetic Resonance of ZnO Tetrapod Structures. Adv. Funct. Mater. 14 (2004) pp. 856−864.

44. A.L. Taylor, G. Filipovich, G.K. Lindeberg, Electron Paramagnetic Resonance Associated with Zn Vacancies in Neutron Irradiated ZnO. Solid State Commun. 8 (1970) pp. 1359−1361.

45. B.-Y. Kim, J.-W. Yoon, J.K. Kim, Y.C. Kang, J.-H. Lee, Dual role of multiroom-structured Sn-Doped NiO microspheres for ultrasensitive and highly selective detection of xylene, ACS Appl. Mater. Interfaces, 10 (2018) pp. 16605-16612.

46. T.P. Mokoena, H.C. Swart, K.T. Hillie, Z.P. Tshabalala, M. Jozela, J. Tshilongo, D.E. Motaung, Enhanced propanol gas sensing performance of p-type NiO gas sensor induced by exceptionally large surface area and crystallinity, Applied Surface Science, 571 (2022) pp. 151-121.

47. L. Liu, P. Zhou, X. Su, Y. Liu, Y. Sun, H. Yang, H. Fu, X. Qu, S. Liu, S. Zheng, Synergistic Ni single atoms and oxygen vacancies on SnO_2 nanorods toward promoting SO_2 gas sensing, Sensors and Actuators: B. Chemical 351 (2022) pp. 130-983.

48. T.-H. Kim, S.-Y. Jeong, Y. K. Moon, J.-H. Lee, Dual-mode gas sensor for ultrasensitive and highly selective detection of xylene and toluene using Nb-doped NiO hollow spheres. Sens. Actuators, B 301 (2019) pp. 127-140.

49. 1910.1028 App A - Substance safety data sheet, Benzene | Occupational Safety and Health Administration (osha.gov) (accessed on the 12th of May 2022).

50. https://nj.gov/health/eoh/rtkweb/documents/fs/2014.pdf (accessed on the 12th of May 2022).

51. Y.-M. Jo, T.-H. Kim, C.-S. Lee, K. Lim, C.W. Na, F. Abdel-Hady, A.A. Wazzan, J.-H. Lee, Metal−organic framework-derived hollow hierarchical Co_3O_4 nanocages with tunable size and morphology: ultrasensitive and highly selective detection of methylbenzenes, ACS Appl. Mater. Interfaces, 10 (2018) pp. 8860-8868.

52. H. Gao, D. Wei, P. Lin, C. Liu, P. Sun, K. Shimanoe, N. Yamazoe, G. Lu, The design of excellent xylene gas sensor using Sn-doped NiO hierarchical nanostructure, Sensors and Actuators B: Chemical, 253 (2017) pp. 1152-1162.

53. J. Guo, Y. Li, B. Jiang, H. Gao, T. Wang, P. Sun, F. Liu, X. Yan, X. Liang, Y. Gao, J. Zhao, G. Lu, Xylene gas sensing properties of hydrothermal synthesized SnO_2-Co_3O_4 microstructure, Sensors and Actuators B: Chemical, 310 (2020) pp. 127-780.

54. H. Wang, M. Chen, Q. Rong, Y. Zhang, J. Hu, D. Zhang, S. Zhou, X. Zhao, J. Zhang, Z. Zhu, Q. Liu, Ultrasensitive xylene gas sensor based on flowerlike SnO_2/Co_3

O_4 nanorods composites prepared by facile two-step synthesis method, Nanotechnology 31 (2020) pp. 255-501.

55. K. Xu, L. Yang, J.P. Zou, Y. Yang, Q.L. Li, Y.H. Qu, J.R. Ye, C.L. Yuan, Fabrication of novel flower-like Co_3O_4 structures assembled by single-crystalline porous nanosheets for enhanced xylene sensing properties, J. Alloys. Compd. 706 (2017) pp. 116–125.

56. C. Sun, X.T. Su, F. Xiao, C.G. Niu, J.D. Wang, Synthesis of nearly monodisperse Co_3O_4 nanocubes via microwave-assisted solvothermal process and their gas sensing properties, Sens. Actuator B Chem. 157 (2011) pp. 681–685.

57. L. Du, X. Song, X. Liang, Y. Liu, M. Zhang, Formation of $NiCo_2O_4$ hierarchical tubular nanostructures for enhanced xylene sensing properties, Appl. Surf. Sci., 526 (2020) pp. 146-706.

58. B. Zhang, F. Qu, X. Zhou, S. Zhang, T. Thomas, and M. Yang, Porous coral-like $NiCo_2O_4$ nanospheres with promising xylene gas sensing properties, Sens. Actuators B, Chem., 261 (2018) pp. 203–209.

59. V.S. Vaishnav, S. G. Patel and J. N. Panchal, Development of ITO thin film sensor for detection of benzene, Sens. Actuators, B, 206 (2015) pp. 381–388.

60. J.-H. Kim, A. Katoch, S.-H. Kim and S. S. Kim, Chemiresistive Sensing Behavior of SnO_2 (*n*)–Cu_2O (*p*) Core–Shell Nanowires, ACS Appl. Mater. Interfaces, 7 (2015) pp. 15351–15358.

61. J.-H. Kim, J.-H. Lee, A. Mirzaei, H. W. Kim, S.S. Kim, Optimization and gas sensing mechanism of n-SnO_2-p-Co_3O_4 composite nanofibers, Sens. Actuators, B, 248 (2017) pp. 500–511.

62. J.-H. Kim, P. Wu, H. W. Kim and S. S. Kim, Highly Selective Sensing of CO, C_6H_6, and C_7H_8 Gases by Catalytic Functionalization with Metal Nanoparticles, ACS Appl. Mater. Interfaces, 8 (2016) pp. 7173-7183.

63. Y. Vijayakumar, G.K. Mani, D. Ponnusamy, P. Shankar, A.J. Kulandaisamy, K. Tsuchiya, J. B.B. Rayappan, M.R. Reddy, J. Alloys Compd., 731 (2018) pp. 805–812.

64. L. Sui, X. Zhang, X. Cheng, P. Wang, Y. Xu, S. Gao, H. Zhao and L. Huo, ACS Appl. Mater. Interfaces, 9 (2017) pp. 1661–1670.

65. F. Zhang, X. Wang, J. Dong, N. Qin and J. Xu, Selective BTEX sensor based on a SnO_2/V_2O_5 composite, Sens. Actuators, B, 186 (2013) pp. 126–131.

66. F. Li, Q. Qin, N. Zhang, C. Chen, L. Sun, X. Liu, Y. Chen, C. Li, S. Ruan, Improved gas sensing performance with Pd-doped $WO_3 \cdot H_2O$ nanomaterials for the detection of xylene, Sens. Actuators, B, 244 (2017) pp. 837–848.

67. C. Feng, C. Wang, H. Zhang, X. Li, C. Wang, P. Cheng, J. Ma, P. Sun, Y. Gao, H. Zhang, Y. Sun, J. Zheng and G. Lu, Enhanced sensitive and selective xylene sensors using W-doped NiO nanotubes, Sens. Actuators, B, 221 (2015) pp. 1475–1482.

68. F. Qu, B. Zhang, X. Zhou, H. Jiang, C. Wang, X. Feng, C. Jiang and M. Yang, Metal-organic frameworks-derived porous ZnO/Ni0.9Zn0. 1O double-shelled nanocages as gas sensing material for selective detection of xylene, Sens. Actuators, B, 252 (2017) pp. 649–656.

69. S.-Y. Jeong, J.-W. Yoon, T.-H. Kim, H.-M. Jeong, C.-S. Lee, Y.C. Kang and J.-H. Lee, Ultra-selective detection of sub-ppm-level benzene using Pd–SnO_2 yolk–shell micro-reactors with a catalytic Co_3O_4 overlayer for monitoring air quality, Journal of Materials Chemistry A, 5 (2017) pp. 1446-1454.

70. R.G. Motsoeneng, I. Kortidis, S.S. Ray, D.E. Motaung, Designing SnO_2 Nanostructure-Based Sensors with Tailored Selectivity toward Propanol and Ethanol Vapors, ACS omega 4 (9) pp. 13696-13709.

71. J. Zhang, X. Jia, T. Liu, J. Yang, S. Wang, Y. Li, D. Shao, L. Feng, H. Song, Facile strategy to synthesize porous GO/ZnO heterostructure for enhanced acetone gas sensing properties, Sensors and Actuators: B. Chemical 359 (2022) pp.131-601.

72. C.M. Chang, M.H. Hon, I.C. Leu, Preparation of ZnO nanorod arrays with tailored defect-related characteristics and their effect on the ethanol gas sensing performance Sensors and Actuators B 151 (2010) pp. 15–20.

73. Y. Urfa, V. Çorumlu, A. Altındal, Gamma ray irradiation dose dependent methanol sensing with ZnO nanoparticles, Materials Chemistry and Physics 264 (2021) pp. 124-473.

74. C. Peng, J. Guo, W. Yang, C. Shi, M. Liu, Y. Zheng, J. Xu, P. Chen, T. Huang, Y. Yang, Synthesis of three-dimensional flower-like hierarchical ZnO nanostructure and its enhanced acetone gas sensing properties Journal of Alloys and Compounds 654 (2016) pp. 371-378.

75. M.E. Franke, T.J. Koplin, U. Simon, Metal and metal oxide nanoparticles in chemiresistors: does the nanoscale matter, Small 2 (2006) pp. 36–50.

76. M. Bonyani, J.K. Lee, G.-J. Sun, S. Lee, T. Ko, C. Lee, Benzene sensing properties and sensing mechanism of Pd-decorated Bi_2O_3-core/ZnO-shell nanorods, Thin Solid Films, 636 (2017) pp. 257–266.

77. L.B. Deng, X.H. Ding, D.W. Zeng, S.P. Zhang, C.S. Xie, High sensitivity and selectivity of C-doped gas sensors toward toluene and xylene, IEEE Sens. J., 12 (2012) pp. 2209-2214.

78. D.L. Baulch, C.T. Bowman, C.J. Cobos, R.A. Cox, T. Just, J.A. Kerr, M.J. Pilling, D. Stocker, J. Troe, W. Tsang, R.W. Walker, J. Warnatz, Evaluated kinetic data for combustion modeling: supplement II, J. Phys. Chem. Ref. Data, 34 (2005) pp. 757-1397.

79. G.A. Russell, the Rates of Oxidation of Aralkyl Hydrocarbons. Polar Effects in Free Radical Reactions. J. Am. Chem. Soc. 78 (1956) pp. 1047−1054.

CHAPTER FIVE

LOW-OPERATIONAL TEMPERATURE FOR SELECTIVE DETECTION OF XYLENE AND NO_2 GASES USING A p-n CuO-ZnO HETEROSTRUCTURE-BASED SENSOR

5.1. INTRODUCTION

With the rapid advancement of urbanization and industrialization over the years, monitoring outdoor and indoor pollution has become an important focal point for the science community as human health has strongly been affected by worsening air pollution. Globally, about 4 million people die annually because of poor air quality **[1]**. Amongst the volatile organic compounds (VOCs), benzene, toluene, ethylbenzene, and xylene (BTEX) are hazardous aromatic hydrocarbon compounds, which have become chronic environmental air polluters. These compounds are mostly utilized as organic solvents in factories of paint, leather and plastic, etc, however, it is also well-known that the use of heaters during the cold seasons to warm up indoor spaces tends to release significant amounts of BTEX **[2]**. Among the BTEX complexes, xylene is the most common indoor pollutant, with prolonged exposure having serious consequences for the human respiratory system **[3, 4]**. While several methods have been attempted to detect or monitor xylene vapour, they appear to be expensive to operate and maintain **[5, 6]**. Thus, cheaper methods that selectively, accurately and rapidly detect and monitor xylene vapour are urgently required.

Xylene gas sensors using various semiconductor metal oxides (SMOs) are well-reported **[7-12]**. Guo et al. **[13]** fabricated a SnO_2-Co_3O_4 heterostructure-based sensor

for selective detection of xylene at 100 ppm at 175 °C. Wang et al. **[14]** fabricated SnO_2/Co_3O_4 nanorods-based sensors for the detection of 100 ppm xylene at an operational temperature of 280 °C. Kim et al. **[15]** developed $Cr_2O_3/ZnCr_2O_4$ heterostructure-based sensor to detect 5 ppm xylene at 275 °C using a galvanic replacement reaction. Chan et al. **[16]** prepared a Fe_2O_3-$ZnFe_2O_4$ composite sphere-based sensor, which displayed vastly sensitive detection to 5 ppm xylene at an elevated temperature of 300 °C. Elsewhere, p-p-type $NiO/NiCr_2O_4$ heterostructures fabricated using a hydrothermal synthesis displayed a superior selectivity towards xylene, with minimal cross-sensitivity towards other interferences at the operational temperature of 225 °C **[17]**. A recent report by Li et al. **[18]** showed rapid response/recovery behaviour towards xylene using $ZnCo_2O_4$ hierarchical porous architectures-based sensor at an operational temperature of 260 °C. As shown, significant work has been done on xylene detection, with the sensors disclosing a rapid response and recovery times. However, the elevated sensing temperatures pose new challenges to these SMO-based sensors. Such high operating temperatures lead to higher power consumption and poor long-term stability. It is found that elevated operational temperature leads to the growth of SMO grains, thus influencing the gas diffusion at the grain boundaries that is accountable for the unwanted long-term drift issue induced by sintering **[19-20]**. Therefore, the present study reports on the selective detection of xylene and NO_2, as indoor air pollutants, at a low operational temperature of 100 °C and 25 °C, respectively, utilizing p-n CuO-ZnO heterostructure-based sensors prepared using a hydrothermal approach. The mechanism for improved xylene sensing characteristics was also deliberated from the synergistic influence of oxygen vacancies (V_O) and the creation of p-n CuO-ZnO heterostructure.

5.2. EXPERIMENTAL DETAILS

5.2.1. MATERIALS

All the reagents were utilized without any additional purification. Zinc (II) acetate dihydrate (Zn $(CH_3COO)_2.2H_2O$) (>98% purity), copper (II) acetate monohydrate ($C_4H_6CuO_4.H_2O$, >98%), ethanol, and sodium hydroxide (NaOH,) were purchased from Merck. Nine (9) primary reference gas mixtures (PRGMs) were used to test the fabricated sensor devices. The PRGMs were purchased from the National Metrology Institute of South Africa (NMISA) with a cylinder capacity of 5L. These included, toluene, ethylbenzene and xylene (BTEX), ethanol, methane (CH_4), sulphur dioxide (SO_2), carbon dioxide (CO_2), and nitrogen dioxide (NO_2).

5.2.2. SYNTHESIS OF CUO-ZNO HETEROSTRUCTURES

In a typical 250 ml Erlenmeyer flask, 2.5g $C_4H_6CuO_4.H_2O$ and different ratios (0.1, 0.25, 0.5 and 1 wt. %) of Zn $(CH_3COO)_2.2H_2O$ were added respectively. Equal amounts (40ml) of water and ethanol were also added to dissolve the precursors. A 0.5M NaOH was gradually added to the mixture using a pipette and the solution was stirred for 1 hour. Finally, the mixture was transferred into a lined autoclave Teflon vessel for 1 hour at 150 ºC. Then, the precipitates were washed with ethanol and water, then dried at 80 ºC in the oven and calcined at 400 °C for 2 hours.

5.2.3. CHARACTERIZATION TECHNIQUES

The structural characteristics were investigated utilizing X-ray diffraction (XRD, Bruker AXS D8 Advance x-ray diffractometer) fitted with a Cu-kα x-ray radiation source. A scanning electron microscope (SEM, Zeiss) was employed to investigate the surface

morphology. Structural and morphological analyses were done by high-resolution transmission electron microscope imaging (HR-TEM, FEI Tecnai G^2 20 FEG-TEM operated at 200 kV) and selected area electron diffraction (SAED) analysis. Spectral image (SI) maps of the different SMOs were collected by coupling the STEM probe with energy dispersive x-ray spectroscopy (EDS); so-called (STEM-EDS). The elemental composition measurements were conducted using x-ray photoelectron spectroscopy (PHI 5000 Scanning ESCA Microprobe).

5.2.4. FABRICATION AND TESTING OF THE SENSING DEVICES

To prepare and fabricate CuO-ZnO-based sensors, the nanomaterials were mixed with ethanol and ground in a mortar to form a paste, which was homogenously spread over the interdigital electrodes. The variation in the resistance of the sensors was measured by using a 4-channel Gas Mixing System (GMS) sensing station. The assembled sensing devices were placed in a chamber made of Teflon and exposed to nine different gases, which included BTEX, ethanol, CH_4, SO_2, CO_2, and NO_2. The measurements were conducted at four operational temperatures (25, 75, 100 and 150 °C). The sensors' temperatures were set by altering the heating voltage. Prior to the measurements, the sensors were exposed to dry air for 3 hrs to stabilize the resistance and during the measurements, the sensors were tested to analyte gases for 5 min and the dry air was also introduced for 5 min for recovery. The sensing response was specified as R_g/R_a and R_a/R_g, for the reducing and oxidizing gas, respectively, denoting the resistance ratio of the sensor exposed to air (R_a) and tested gases (R_g).

5.3. RESULTS AND DISCUSSION

5.3.1. STRUCTURAL AND MORPHOLOGICAL MEASUREMENTS

Figure 5.1:a illustrates the XRD patterns of the CuO-ZnO heterostructures synthesized by varying the concentration of ZnO. For the ZnO (0.1 wt. %) in CuO, the patterns indeed confirm the formation of CuO-ZnO heterostructure, where the (100), (002), (101), (102) and (110) planes associated with ZnO structure are observed. These peaks are also observed at higher concentrations (i.e., 0.25-1.0 wt. %) of ZnO. Moreover, peaks associated with CuO are also observed. Nonetheless, when increasing the concentration of ZnO, the (111) and (200) peaks associated with CuO became broad and their intensity reduced for the CuO-ZnO (1.0 wt. %). Additionally, the intensity of the (100), 002) and (101) peaks associated with ZnO increased for the CuO-ZnO (1.0 wt. %) heterostructure.

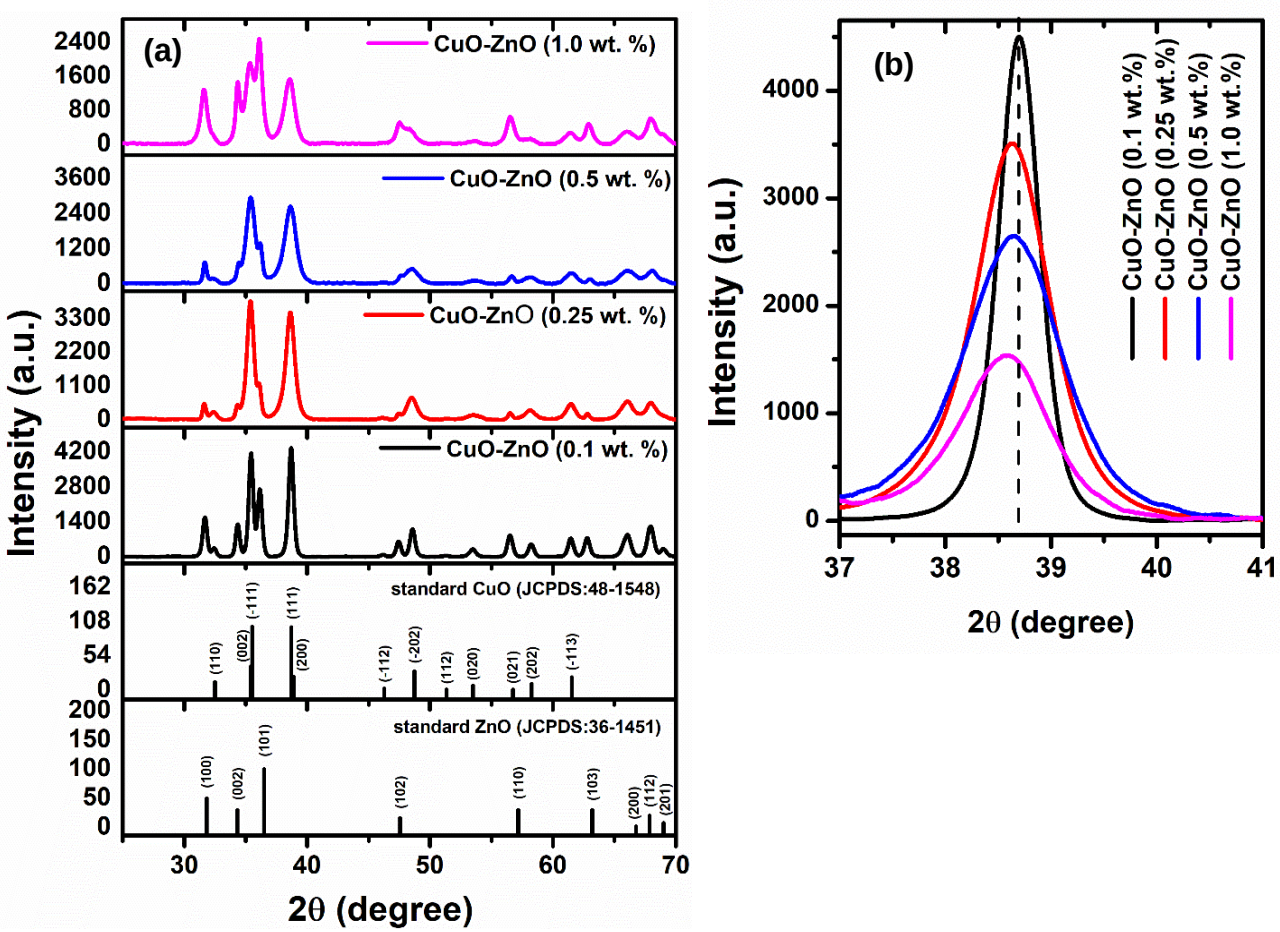

Figure 5.1: (a) XRD patterns of CuO-ZnO heterostructures prepared by varying ZnO wt. %, (b) crystallite sizes versus the ZnO wt. %, (b) Magnified CuO (111) peak for the CuO-ZnO heterostructures.

A shifting of the CuO (111) peak to lower angles and a reduction in peak intensity are also witnessed when increasing the ZnO content on the CuO matrix as shown in Figure 5.1: b. This shift could be associated with a higher ionic radius of Zn^{2+} (0.74 Å) in comparison to that of Cu^{2+} (0.73 Å) **[21]**. The crystallite sizes associated with (111) peak of CuO were calculated using the Scherrer formula, shown in eq.1 **[21]**.

$$D = \frac{k\lambda}{\beta cos\theta} \quad \textbf{(1)}$$

where $k, \lambda\ \theta\ and\ \beta$ are constants, the wavelength of the X-ray, full width at half maximum and the Bragg's angle, respectively. As depicted in **Table 5.1**, crystallite sizes decrease with an increase in ZnO concentration. While the lattice strain, which was computed using eq. 2 **[21]** increases with an increase in ZnO concentration.

$$\varepsilon = \frac{\beta cos\theta}{4} \quad \textbf{(2)}$$

The quantity of crystal defects, or the irregularity, which exists within a crystal structure, was utilized to calculate the dislocation density. A dislocation is a certain type of topological imperfection existing in the material. The dislocation density was computed using the formula shown in eq. 3 **[21]**:

$$\delta = \frac{1}{D^2} \quad \textbf{(3)}$$

As listed in **Table 5.1**, the dislocation density increases with an increase in ZnO concentration in the CuO matrix. Thus, it can be anticipated that the CuO-ZnO (1.0 wt. %), which has the minimal crystallite size, the highest strain, and dislocation density could lead to superior sensor sensitivity towards gas adsorption. Since larger dislocation density and strain result in improved surface defects, thus this leads to higher gas molecules adsorption on the sensor surface, hence improving the sensor response **[22, 23]**.

Table 5.1: Calculation of crystallite size, dislocation density, and strain.

Samples name	Crystal plane (111)		
	Crystallite size (D)	**Dislocation density, δ ($\times 10^{-2}$ nm^{-2})**	**Strain, ε ($\times 10^{-3}$)**
CuO-ZnO (0.1 wt. %)	17.95	0.310	3.00
CuO-ZnO (0.25 wt. %)	9.9	1.00	3.50
CuO-ZnO (0.5 wt. %)	8.45	1.40	4.10
CuO-ZnO (1.0 wt. %)	7.7	1.70	4.50

Figure 5.2: depicts the SEM samples of CuO-ZnO heterostructures with different concentrations of ZnO (0.1- 1 wt. %). At lower ZnO incorporation on CuO matrix, i.e., 0.1-0.25 wt.%, larger sharp nano-needles/spear structure with an estimated average thickness of 28 nm associated to ZnO were observed, see the low resolution (LR) image in **Figure 5.2: a and c**. Thus, in LR and high resolution (HR) images in **Figure 5.2: a and b**, flower-like structures are surrounded by larger sharp nano-needles/spear structures. This was validated by the higher XRD peaks intensity detected at low ZnO concentration, justifying unregularly formation of ZnO at low concentration.

This justifies that the formation of ZnO nuclei at lower concentrations was quicker than that of CuO. Nonetheless, when increasing the ZnO concentration, **Figure 5.2: c and d**, the nanorods stacked on top of nanoplatelets with a projected average diameter of 1.0 µm are observed. At higher ZnO concentration (i.e., CuO-ZnO (1.0 wt.%), **Figure 5.2: e and f**, the cluster of “nanocrumbs-like” structures arranged in a scattered formation are observed. Moreover, the shape of the “nano-needles/spear-like” structure began to fade and cracks with rough wrinkles began to appear with a rough surface. Therefore, the variation in weight ratio had indeed an effect on the structure and morphologies of the material.

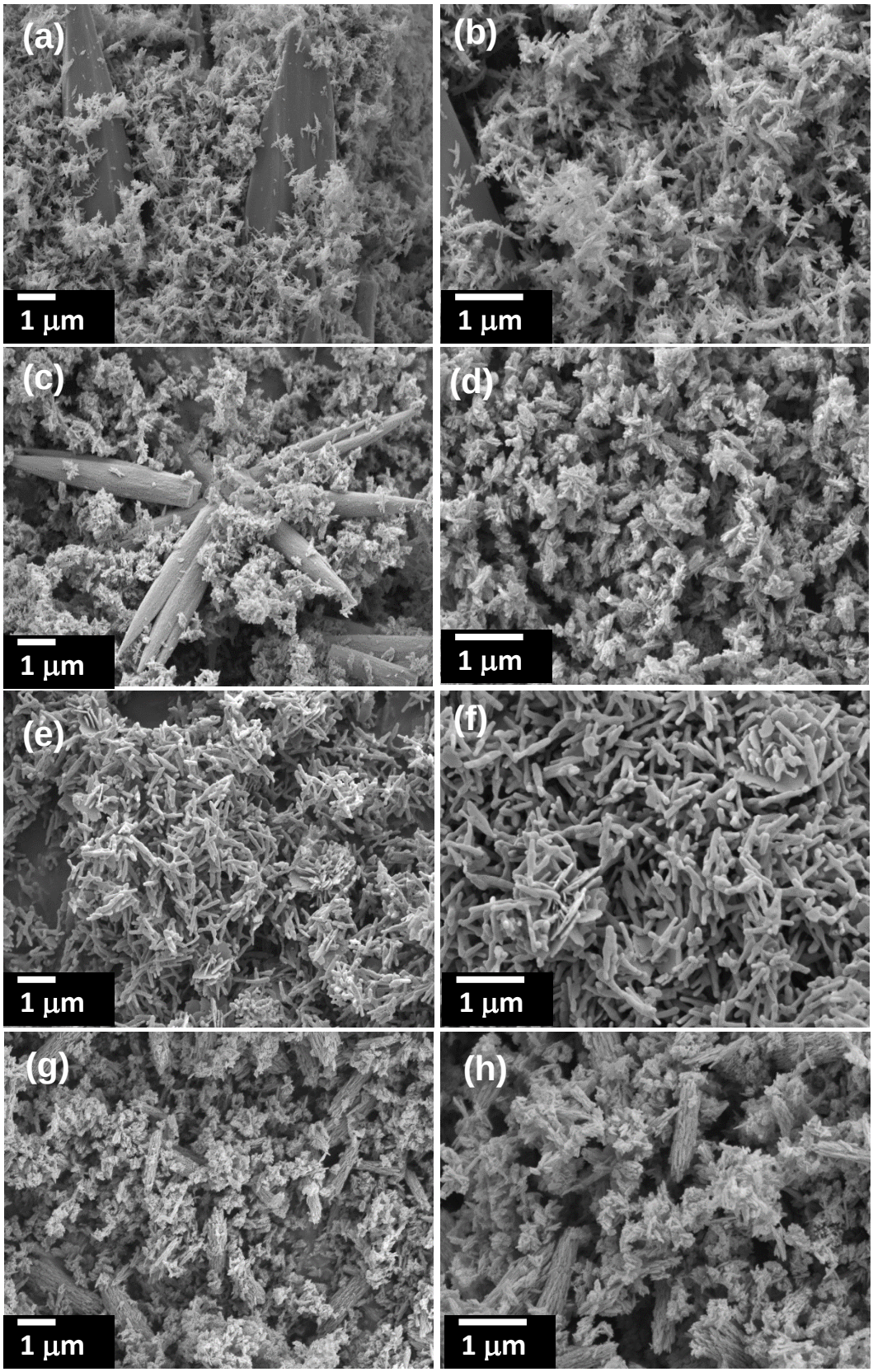

Figure 5.2: LR- and HR-SEM micrographs of (a-b) CuO-ZnO (0.1 wt. %), (c-d) CuO-ZnO (0.25 wt. %), (e-f) CuO-ZnO (0.5 wt. %), (g-h) CuO-ZnO (1.0 wt. %).

TEM analyses were further carried out to probe the internal structure of the heterostructures. **Figure 5.3: a and b** illustrates the low- and high-resolution TEM micrographs and the SAED patterns (**Figure 5.3: c**) of the p-n CuO-ZnO (1.0 wt. %) heterostructures. The low resolution (LR)-TEM analyses in **Figure 5.3: a** and **Appendix A2,** shows rods like structures. While the higher resolution (HR) in **Figure 5.3: b** shows lattice fringes of 0.208 nm corresponding to (111) lattice plane of CuO. Additionally, the lattice spacing of 0.247 nm associated with ZnO was also observed. As presented in **Figure 5.3: b**, the incorporation of ZnO into CuO lattice produced strain in the system that is released by generating lattice distortions, such as stacking faults in the crystal planes **[24]**. As observed from the SAED patterns in **Figure 5.3: c-f**, the materials are polycrystalline. The (100), (002), (102), and (111), (020), and (022) planes shown from the SAED patterns correspond to ZnO and CuO structures, respectively. These findings are in-line with the XRD results. Furthermore, it is clear from the SAED patterns in **Figure 5.3: c-f** that when increasing the loading of ZnO in the CuO lattice, diffused diffraction patterns are observed. This behaviour is consistent with the XRD analyses. STEM- EDS SI maps in **Figure 5.3: g** and **Appendix A2** show different colour maps, which display the elemental composition of the individual heterojunctions and confirms the dual composition of each nanostructure. This confirms a uniform distribution of ZnO in the CuO matrix.

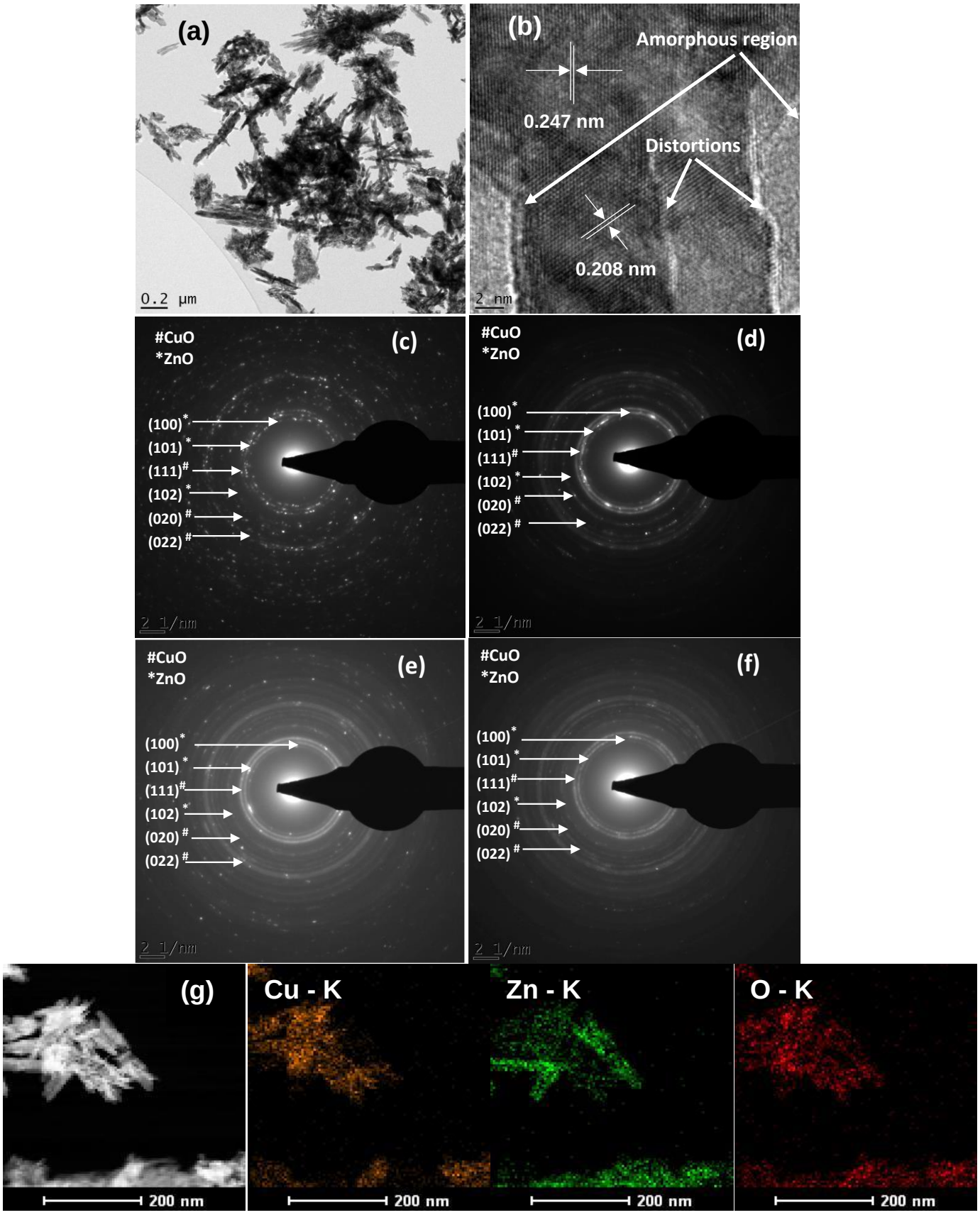

Figure 5.3: (a, b) LR and HR-TEM of CuO-ZnO (1.0 wt. %). Note that (c-f) corresponds to SAED patterns of (c) CuO-ZnO (0.1 wt. %), (d) CuO-ZnO (0.25 wt. %), (e) CuO-ZnO (0.5 wt. %), (f) CuO-ZnO (1.0 wt. %). (g) STEM-EDS maps of (d) CuO-ZnO (1.0 wt. %).

5.3.2. GAS SENSING PERFORMANCE TOWARDS XYLENE

To regulate an optimal operational temperature, the sensor resistance towards various gases was probed. The sensor resistance of all the sensors shows a clear decrease when increasing the operational temperature, see **Figure 5.4: a**. This behavior is regulated by the intrinsic characteristic of SMO **[25]**. The plot of the response versus the operational temperature is depicted in **Figure 5.4: b**. Indeed, the sensor response of all the sensors increases with operational temperature. Among the sensors, the CuO-ZnO (1.0 wt. %) showed a greater response of 10.9 towards 100 ppm of xylene vapour in comparison to other sensors.

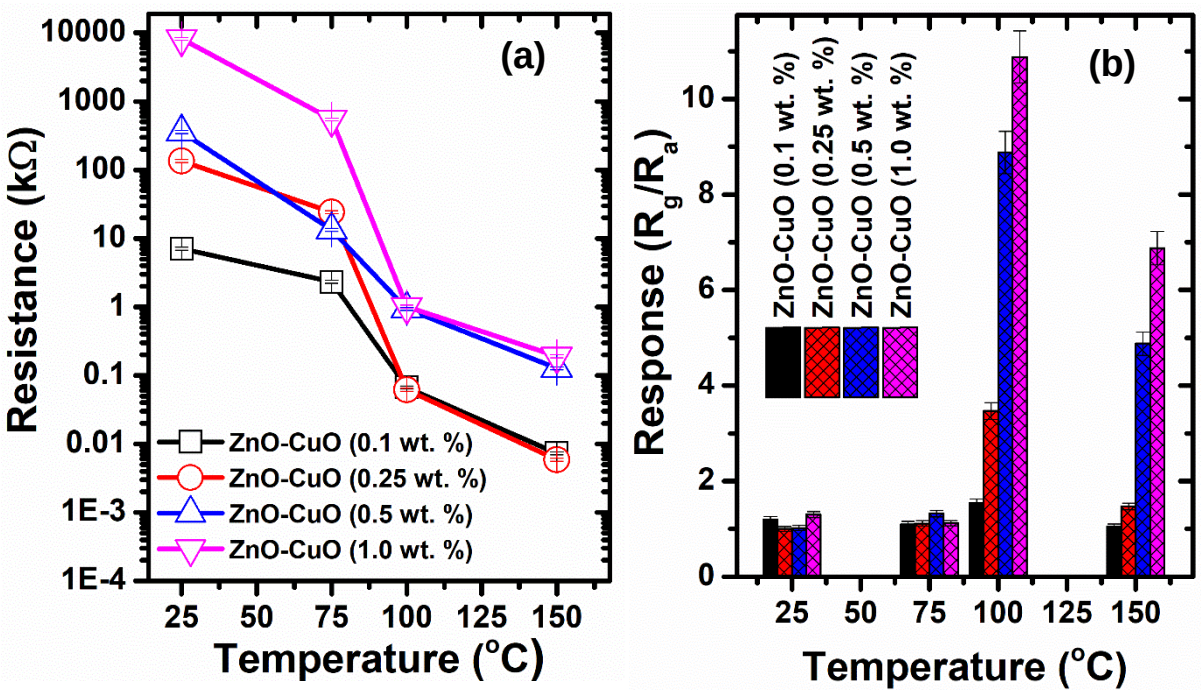

Figure 5.4: (a) R_a versus the operational temperature, (b) response of various sensors towards 100 ppm xylene vapour versus the operational temperature.

The dynamic resistance plots of various sensors towards 100 ppm xylene measured at 100 °C are exhibited in **Figure 5.5: a**. The sensors clearly show continuous change

in resistance towards various concentrations of xylene, displaying a continuous response/recovery behaviour. This behaviour is validated by the sensor response plot illustrated in **Figure 5.5: b**, where the sensor response increases with increased xylene concentration. The plots of the response versus the xylene concentration depicted in **Figure 5.5: c**, show that the sensor's response indeed increases with the gas concentration (5- 100 ppm), where the CuO-ZnO (0.5 wt. %) and CuO-ZnO (1.0 wt. %) disclosed an exponential growth with increased xylene concentration. Though the CuO-ZnO (1.0 wt. %)-based sensor demonstrated improved response in comparison to its counterparts. The sensor disclosed responses of 1.87 and 10.88 at 5 ppm and 100 ppm xylene concentrations, respectively.

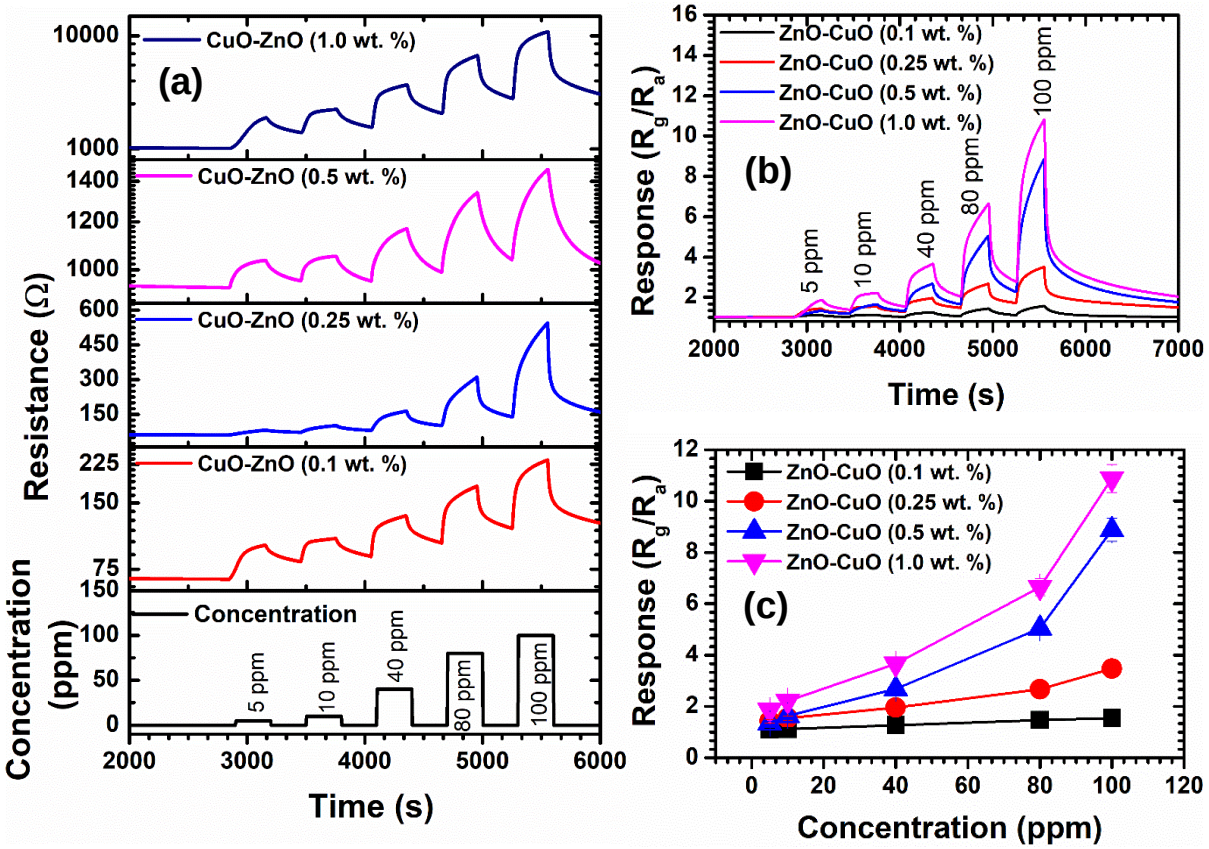

Figure 5.5: (a) Dynamic resistance plot, (b) transient response plot and (c) response against the xylene concentration measured at 100 °C.

Figure 5.6: a displays the calibration curves (linear fit) of various sensors towards 5-80 ppm xylene vapour at 100 °C. As revealed in **Figure 5.6: a**, the ZnO-CuO (1.0 wt. %) heterostructure-based sensor shows higher sensitivity (slope=0.063 ppm^{-1}) towards xylene as other sensors. Moreover, the correlation coefficients (R^2) of roughly 0.98–1 were realized for all the sensors, which confirmed the consistent detection of the sensors towards xylene.

The limit of detection (LoD) is also another vital parameter to show the lowest concentration level, which the sensors can detect the target, more especially in the case of a leak. Thus, the LoD was computed using the following expression: $LoD = 3\left(\frac{RMS_{noise}}{Slope}\right)$, and the $RMS_{noise} = \sqrt{\sum_i (x_i - x)^2 / N}$, which is associated with the root mean square that is taken from the fluctuation of the sensor resistance prior to the introduction of the target gas in the chamber. Note that the x_i and x are the experimental data point, and N is the average of the data points. As a result, from the expression above, the LoD of 0.111, 0.039, 0.011 and 0.0095 ppm were realized for the CuO-ZnO (0.1 wt.%), CuO-ZnO (0.25 wt.%), CuO-ZnO (0.5 wt.%), and CuO-ZnO (1.0 wt.%), respectively. The minimal LoD of 9.5 ppb may be influenced by abundant oxygen vacancy, enhancing the gas sensing capabilities. This indeed confirms that CuO-ZnO (1.0 wt. %) sensor can detect an ultra-low xylene vapour of 9.5 ppb, indicating that the CuO-ZnO (1.0 wt. %) heterostructure-based sensor can realize sub-ppb-level concentration.

Another vital parameter of the sensors for real-world application is the response/recovery times. The response/recovery times denote the times the sensor is obligated to fulfil 90% of the resistance variation when exposed to analyte gas and /

10 % when recovered in air, respectively. **Figure 5.6: b** shows the plot of the response/recovery times of the CuO-ZnO (1.0 wt. %)-based sensor to various xylene concentrations. Though the response time increases with xylene concentration, nonetheless, at 100 ppm, the sensor still revealed a response time of 87 s, while the recovery time was slightly longer (216 s) at 100 ppm. The rapid response can be associated with improved surface defects, which hastens the reaction of xylene and energetic oxygen species.

The capability of SMO-based sensors to classify the target gas within other interference gases is a critical principle to assess the gas sensor performance **[26, 27]**. As a result, in the current work, the sensors were exposed to different gases at 100 ppm, which included BTX, CH_4, SO_2, NO_2 and CO_2 as shown in the radar plot. It is evident that among the tested sensors, the sensor based on CuO-ZnO (1.0 wt. %) heterostructure established a greater response of 10.88 and improved selectivity towards 100 ppm xylene compared to other interference gases. The detected 100 ppm concentration of xylene agrees with the endorsed permissible exposure level set by Occupational Safety and Health Administration (OSHA) for an 8-hour time-weighted average (TWA) concentration **[28]**. Thus, the selective detection of xylene at 100 ppm illustrates the potential application of the CuO-ZnO (1.0 wt. %) heterostructure-based sensor for indoor quality monitoring.

Furthermore, the ZnO-CuO (1.0 wt. %) heterostructure-based sensor showed superior selectivity with low cross-sensitivity to interfering gases (see **Figure 5.6: c**), such as benzene ($S_{xylene}/S_{benzene}$= 8.5) and toluene ($S_{xylene}/S_{toluene}$ = 2.7). The current cross-sensitivity value is lower than that reported by Woo et al. **[29],** which was $S_{xylene}/S_{toluene}$ = 2.3. It is further observed from the Figure that the SO_2 has the most insignificant

cross sensitivity (S_{xylene}/S_{SO2}= 135.25) towards xylene detection. Basically, the cross-sensitivity ratios ranged from 2.7 (toluene) to 135 (SO_2). This served to demonstrate the outstanding selectivity of the sensor that is critical for its discriminability to xylene in real conditions. Though we should point out that the dissimilarity between the alike chemistry of xylene and toluene utilizing SMO-based sensors is reflected as the most challenging issue in the gas sensing fraternity to selectively detect one in the presence of the other.

From this standpoint, the current CuO-ZnO (1.0 wt. %) based sensor can be adopted as an excellent device for selective detection of xylene vapour at lower operational temperatures. The current selectivity towards xylene over other interference gases, such as BTE, could be justified based on the following points:

(1) The difference in the number of methyl groups has a significant influence on selectivity. For instance, xylene has one additional methyl group compared to toluene, as a result, it is very reactive with a higher oxidation rate **[30, 31]**. A previous study by Russell's reported a higher oxidation rate of 0.0039 mol h^{-1} for xylene at 90 °C in comparison to 0.0013 mol h^{-1} for toluene **[32].**

(2) The bond energy of the BTEX also plays vital role in the gas sensing performance **[33]**. Generally, bond energies (BE) of toluene and xylene are the lowest and differ slightly, which are respectively, 356 and 375 kJ/mol. While both benzene and ethylbenzene have the highest BE of 431 and 435 kJ/mol, respectively **[34, 35]**. Though toluene has the lowest BE, nonetheless it possesses exceptional chemical stability under distinctive conditions and CH_3 is much more stable than OH and CHO. As a result, this makes it difficult to react, though it can react radically with an oxidant or acid.

(3) The other reason could be due to the enthalpy change of the dehydrogenation process **[36, 37]**. For instance, among the BTEX, the enthalpy variation of the dehydrogenation of both toluene and xylene only differs by 0.4 J/mol, and which is about 157.8 and 157.4 J/mol for toluene and xylene, respectively **[38, 39].** Nonetheless, the enthalpy change of benzene is almost higher by a value of 100, than those of toluene and xylene, which is 255.4 kJ/mol.

(4) As shown from the XRD and TEM analyses, the CuO-ZnO (0.1 wt. %), CuO-ZnO (0.5 wt. %) and CuO-ZnO (1.0 wt. %) show higher exposed (100) facets for the ZnO, which showed better selectivity towards xylene. Though, it is observed that for CuO-ZnO (1.0 wt. %), the selectivity towards xylene is more improved, due to enhanced exposed (100) facets **[40-42]**. Nonetheless, more work is needed to verify our assumptions.

(5) The CuO-ZnO (1.0 wt. %.), has a higher number of heterojunctions compared to those with lower ZnO wt. %. More p-n heterojunctions resulted in improved sensing response **[43]**. Nonetheless, studies have shown that increasing the doping or loading concentration could result in poor performance. Such decrease could be associated with the percolation influence, where additional p-CuO-n-ZnO homojunctions are developed in the sensing layer, thus reducing the number of p-n heterojunctions that are more active for modulation of the resistance as reported by previous studies **[44-46]**.

Therefore, though toluene showed slightly lower BE and change in enthalpy of dehydrogenation, however, the additional methyl group and higher oxidation rate of xylene justify the higher selectivity of CuO-ZnO (1.0 wt.%) heterostructure-based

sensor towards xylene vapour. Moreover, as observed from the selectivity plot, the order of response is xylene>toluene>benzene, justify the above observation.

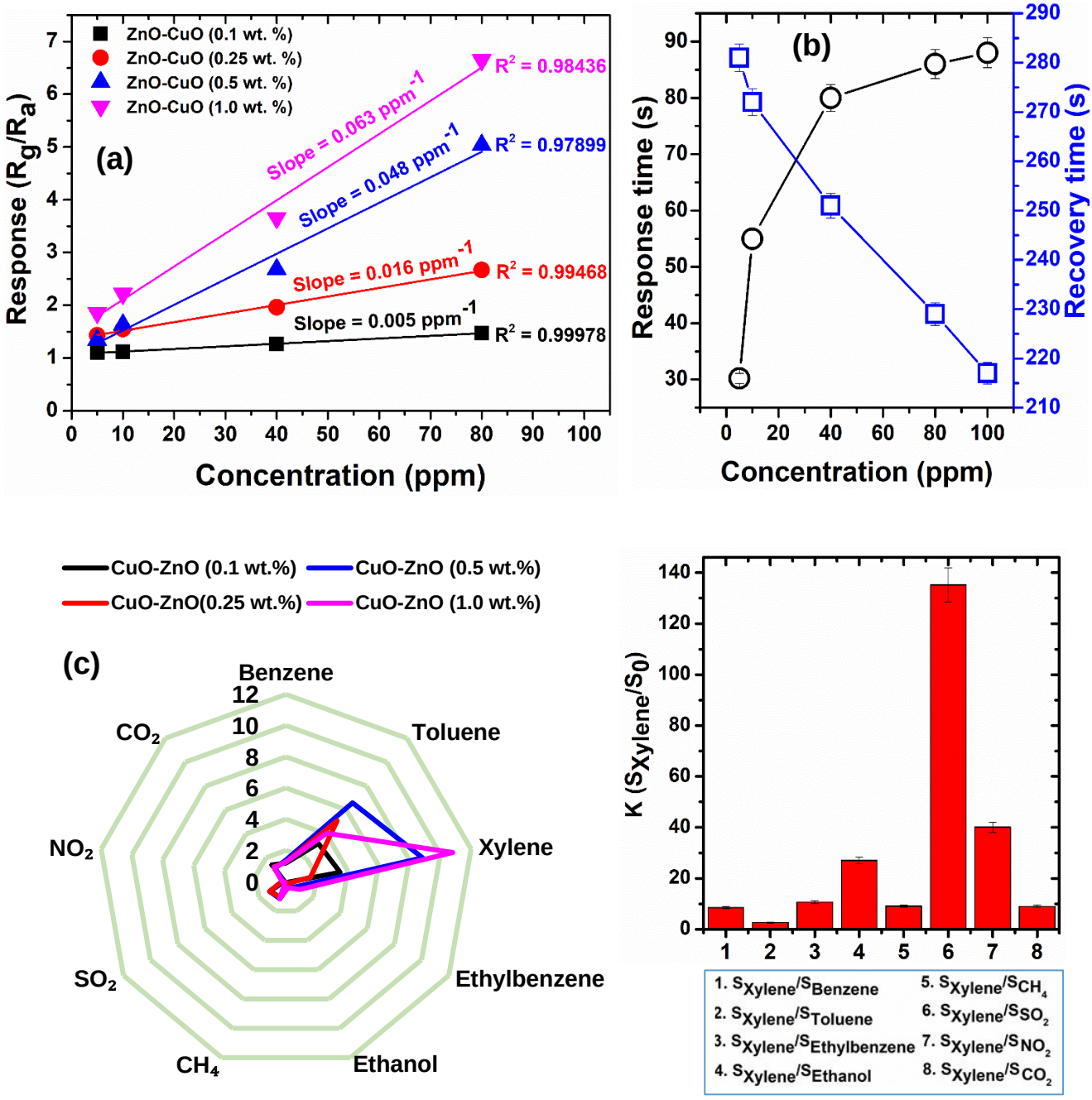

Figure 5.6: (a) Calibration curves for the sensitivity and LOD calculations, (b) response /recovery times at various xylene concentrations, (c) The radar graph and (d) cross-sensitivity plot towards xylene over other interference gases.

In addition to selectivity, the repeatability, as well as the sensor durability (i.e., long-term stability) are also vital parameters for the practical application and commercialization of SMO-based gas sensors. **Figure 5.7: a** shows the repeatability plot of the CuO-ZnO (1.0 wt. %) heterostructure-based sensor tested towards fixed xylene concentration of 100 ppm at 100 °C, showing 8 successive response and recovery cycles. The sensor displays almost identical responses/recovery cycles, confirming its possible usage for the detection of xylene for indoor air quality.

The influence of humidity on the sensor characteristics was then studied. The change in the CuO-ZnO (1.0 wt.%) sensor resistance was tested towards five successive cycles of 100 ppm xylene under 20 and 40 % RH at 100 °C, see **Figure 5.7: b**. Indeed, the response was slightly reduced by 30 and 22 % in the presence of 20 and 40% RH, respectively (**Figure 5.7: c**). This justifies that RH hampers the adsorption of oxygen and leads to fewer oxygen ions. It is evident that at 40 % RH, the response slightly increased in comparison to that of 20% RH. This behavior has also been witnessed by previous researchers **[47-49]**. This is probably due to that at higher RH conditions, the interaction of the CuO-ZnO-based sensor with xylene is stimulated by humidity. To validate this, the t_{res} and t_{rec} were calculated for dry air and RH analyses, see **Appendix A3.** Remarkably, the t_{res} increases with an increase in RH, while the t_{rec} decreases, denoting that humidity acts as a catalyst towards t_{rec}. This behavior was previously reported by Tshabalala et al. **[48]**, where they observed a decrease in t_{res} and t_{rec} with an increase in RH conditions.

Long-term stability is also another vital parameter required for real-time application. Thus, the stability of the CuO-ZnO (1.0 wt.%) heterostructure-based sensor towards xylene vapour was tested for a period of 30 days in dry air and under the existence of

40 % RH, see **Figure 5.7: d**. It is evident that the response of the sensor towards xylene only reduced by 4.8% and 6.3% in dry and 40% RH. This trivial variation indeed shows that the CuO-ZnO (1.0 wt. %) heterostructure-based sensor possesses good long-term stability detection of xylene and can be utilized for real-time application.

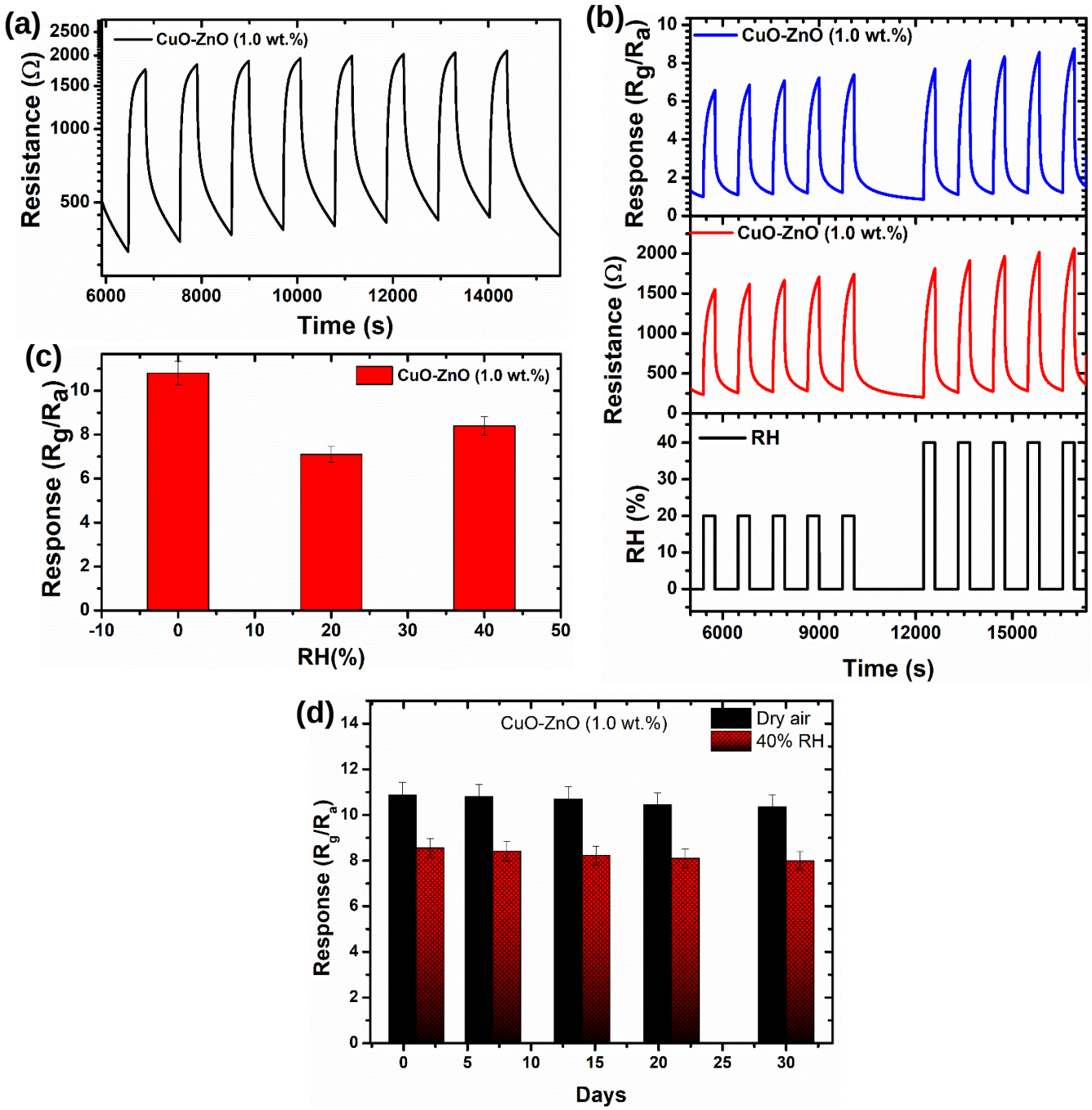

Figure 5.7: (a) Repeatability, (b) resistance and response plots at various RH percentages, (c) Response versus RH (%) and (d) Long-term stability plot in dry air and 40% RH. Note all the measurements in this Figure were done at 100 °C.

Table 5.2 compares the xylene sensing characteristics of the current work and that of other published studies. Most of the fabricated sensors were achieved using the hydrothermal approach, due to its exceptional advantages such as low synthesis temperature and providing large production of nanomaterials. As observed in **Table 5.2**, the current sensor displays a lower operational temperature of 100 °C, in comparison to the published studies, indicating the benefit of low power consumption. Moreover, the low operational temperature could reduce the crystal growth and prolong the sensor lifetime and benefit the practical application. Certainly, our current sensor also shows a better response time than $NiO/NiCr_2O_4$ **[51]**, Sn-NiO **[52]** and SnO_2-Co_3O_4 **[53]**.

Table 5.2: Summary of published work on xylene sensor compared to the current work.

Sensing element	Method	Conc. (ppm)	T_{res}/T_{rec} (s)	Response	Temp. (°C)	LOD (ppm)	Refs.
CuO-ZnO	**Hydrothermal**	**100**	**87/216**	**10.88**	**100**	**0.0095**	**This work**
Pt- Cr_2O_3-WO_3	Hydrothermal	10	5/736	75.3	225	0.50	**[47]**
TiO_2-Nanowires	Hydrothermal	100	45/95	37	125	0.937	**[48]**
Ni/Al_2O_3	RF sputtering	100	20/300	10.0	340	0.07	**[49]**
SnO_2/Co_3O_4	Hydrothermal	100	98/107	47.8	280	-	**[50]**
NiO/$NiCr_2O_4$	Hydrothermal	100	1217/597	66.2	225	0.05	**[51]**
Sn-NiO	Hydrothermal	100	298/223	20.2	225	0.30	**[52]**
SnO_2- Co_3O_4	Hydrothermal	100	204/367	101	175	0.05	**[53]**

5.3.3. XYLENE GAS SENSING MECHANISM

Currently, the mechanism of gas sensing for SMO is built on the variation of sensor resistance due to the adsorption/desorption process. Since p-n CuO-ZnO

heterostructure-based sensor acts as a p-type semiconductor, thus, the holes are the major carriers. When exposing the CuO-ZnO heterostructure-based sensor to air at an operational temperature of 100 °C, oxygen molecules are adsorbed on the sensor surface, hence creating adsorbed oxygen anion species (O^-), see **Scheme 5.1(a)** and **reaction (1-2)** by interacting with free electrons (e^-) from conductance. As a result, the charge carriers increase, leading to the creation of a thick hole accumulation layer (HAL) **[54-55]**.

$$O_{2(gas)} \rightarrow O_{2(ads)} \quad \textbf{(1)}$$

$$O_2(gas) + e^- \rightarrow 2O^-(ads) \quad (100\,^oC < 300\,^oC) \quad \textbf{(2)}$$

However, once the CuO-ZnO (1.0 wt. %) is tested towards analyte gas, like xylene, xylene vapour, it would interact with the adsorbed oxygen anion species (O^-), leading to the release of the electrons of the captured into the material. The electrons that are free will consume the holes in CuO and result in surplus electrons in ZnO, as a result, the depletion layer width will reduce. Owing to the formed p-n nanojunctions, the holes that are consumed in CuO would hastily be added from the electron depletion layer at p-n junctions. Then, the holes in the CuO-ZnO heterojunction will move to CuO across the interface and the electrons migrate to the conduction band, leading in an increase of the charge carrier concentration, resulting in a reduced resistivity. Therefore, the CO_2, H_2O and electrons will be released as shown in **Scheme 5.1(b)** and **reaction (3-4)**.

$$(C_6H_4CH_3CH_3)_{gas} \leftrightarrow (C_6H_4CH_3CH_3)_{ads} \quad \textbf{(3)}$$

$$(C_6H_4CH_3CH_3)_{ads} + 21O^- \rightarrow 8CO_2 + 5H_2O + 21e^- \quad \textbf{(4)}$$

While the superior selectivity was justified above, thus the improved sensitivity of CuO-ZnO (1.0 wt.%) compared to other sensors could be justified by the formation of depletion layer induced by adsorption of oxygen species at interface of p-n heterojunction between the CuO and ZnO surface as depicted in **Scheme 5.1(c)**. In general oxygen deficient ZnO displays an n-type, while an oxygen excess CuO displays a p-type conductivity. Generally, ZnO contains a higher bandgap (3.4 eV), as well as higher electron affinity of 4.35 eV compared to CuO (1.35 eV) and 4.07 eV. Thus, difference in a Fermi level shown in **Scheme 5.1(c)**, will lead to electrons movement from the conduction band of ZnO to CuO, whereas holes will move from the valence band of CuO to ZnO, leading to the formation of heterojunction (**Scheme 5.1: d**). Thus, the existence of number of p–n nanojunctions at the interface of CuO and ZnO leads in an extraordinary increase in the heterostructure resistance in comparison to pure ZnO or CuO.

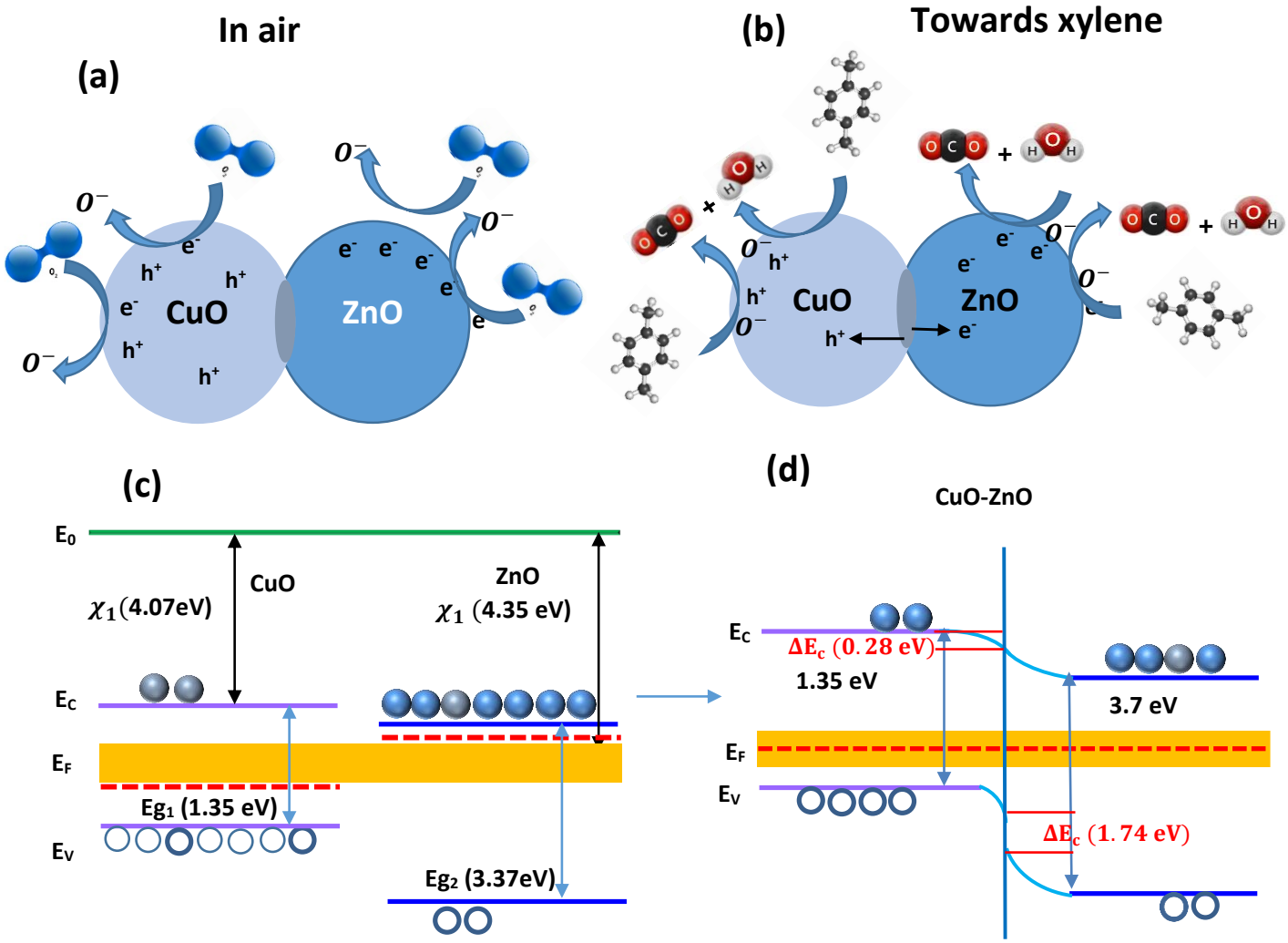

Scheme 5.1: Sensing mechanism of CuO-ZnO-NaOH-based sensor (a) in air and (b) towards xylene vapour at 100 °C, (c-d) energy band diagram in air and towards xylene vapour.

To further justify the superior sensing performance of CuO-ZnO (1.0 wt. %) heterostructure, UV/vis measurements of the various CuO-ZnO nanostructures, prepared using various concentrations of ZnO were conducted, as shown in **Figure 5.8: a**. The bandgaps of the CuO-ZnO (0.1 wt. %), CuO-ZnO (0.25 wt. %), CuO-ZnO (0.5 wt. %) and CuO-ZnO (1.0 wt. %) were estimated on the reflectance data using Kubelka–Munk illustration as 3.08, 3.03, 2.82 and 2.75 eV, respectively. Indeed, the CuO-ZnO (1.0 wt. %), displayed the lowest bandgap in comparison to other materials.

This behavior is consistent with the XRD and TEM analyses, which showed a crystalline behavior of the CuO reducing with increasing the ZnO concentration, leading to a defused Debye on the SAED patterns and distortion or reduced (111) plane of the CuO for the CuO-ZnO (1.0 wt.%). Generally, the smaller bandgap of CuO-ZnO (1.0 wt.%) points out that electrons can be more prone to transition and can produce more photogenerated carriers, which will result to improved change in sensor resistance and reduced operational temperature. Thus, this justifies the higher sensing performance of the CuO-ZnO (1.0 wt. %) heterostructure-based sensor.

To further explore the relationship between the microstructure and the sensing parameters, the behaviour of the maximum response versus crystallite sizes, dislocation density and strain is shown in **Figure 5.8: b**. Remarkably, the response increases with an increase in strain and dislocation density, while the crystallite sizes decrease, showing a maximum response of 10.88 for the CuO-ZnO (1.0 wt. %) heterostructure. Therefore, the addition of ZnO in CuO has a substantial effect on the dislocation density, lattice strain, and the crystallite size, which leads to a superior performance on the sensing characteristics of CuO-ZnO (1.0 wt.%) heterostructure based sensor.

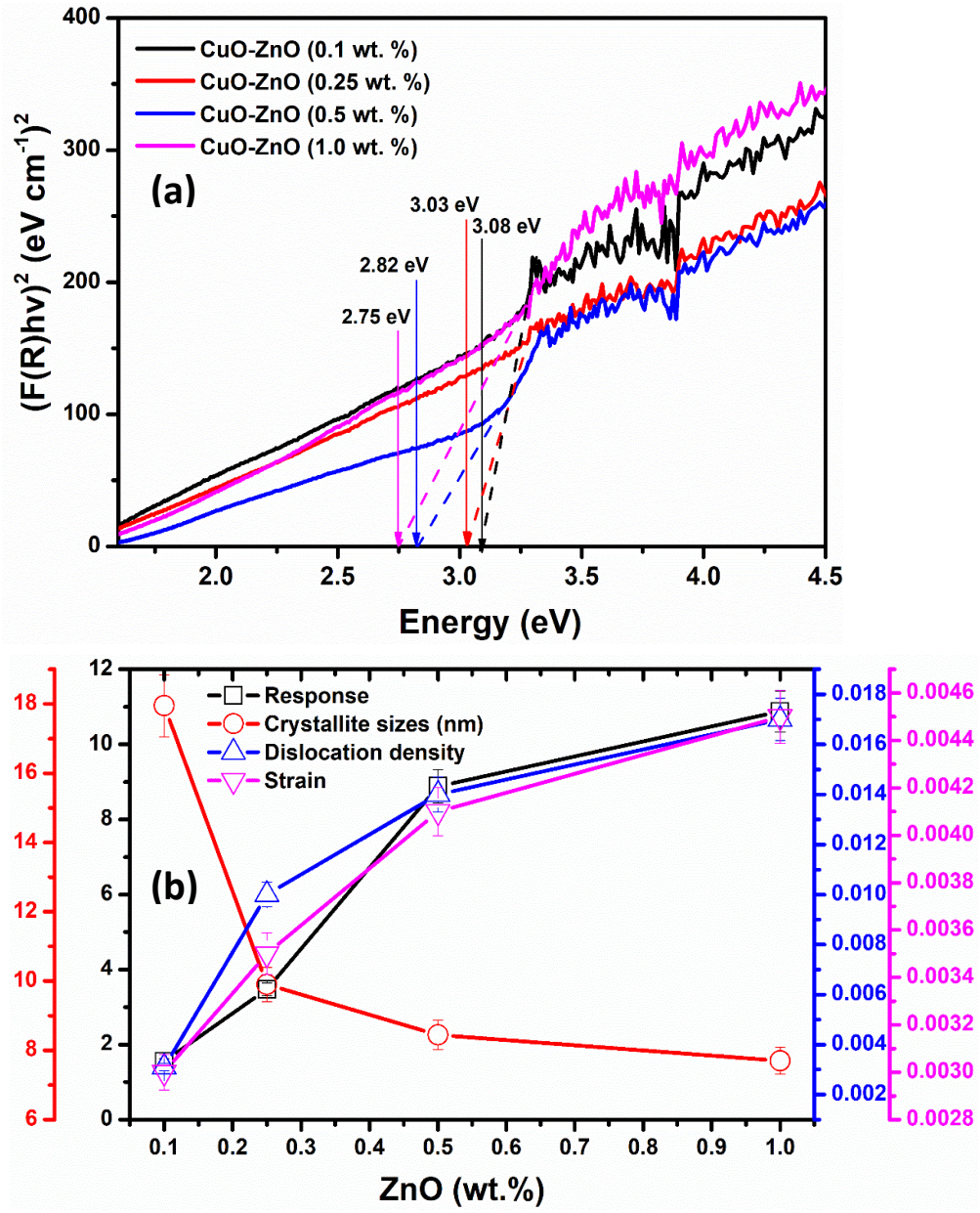

Figure 5.8: (a) Kubelka–Munk function figure utilized for estimation of the band gap, (b) Relationship between the response, crystallite size and dislocation density and strain of CuO-ZnO at various ZnO concentrations.

5.3.4. ROOM TEMPERATURE NO2 GAS SENSING

Figure 5.9 depicts the responses versus the CuO-ZnO various concentrations at 25 °C, 75 °C and 150 °C, respectively. When the heterostructure CuO-ZnO samples are

exposed to NO_2 the CuO-ZnO nanocomposites exhibits a linear and highest increase in the response of 0.16 to 5-100 ppm of CuO-ZnO (0.5 wt. %) at 25 °C. While at 300 °C, the sensor shows a response of 0.71. In comparison to other molarities, this indicates good repeatability and reproducibility. At 75 °C, all molarities exhibits similar behaviour, with responses increasing linearly from 5 ppm to 300 ppm but gradually levelling off after 300 ppm, with only 0.18 CuO-ZnO (0.1 wt.%) exhibiting the best response at 100 ppm. At 150°C, the response of CuO-ZnO (0.1, 0.25, 1.0 wt. %) shows a linearly increasing response with the increase of concentration from 5 ppm to 100 ppm with maximum responses of 0.12, 0.15, and 0.26, respectively (**Figure 5.10**), but CuO-ZnO (0.5 wt. %) shows a larger sensor response of 0.27 at 5 ppm as the concentration increases until 100 ppm, when it drops.

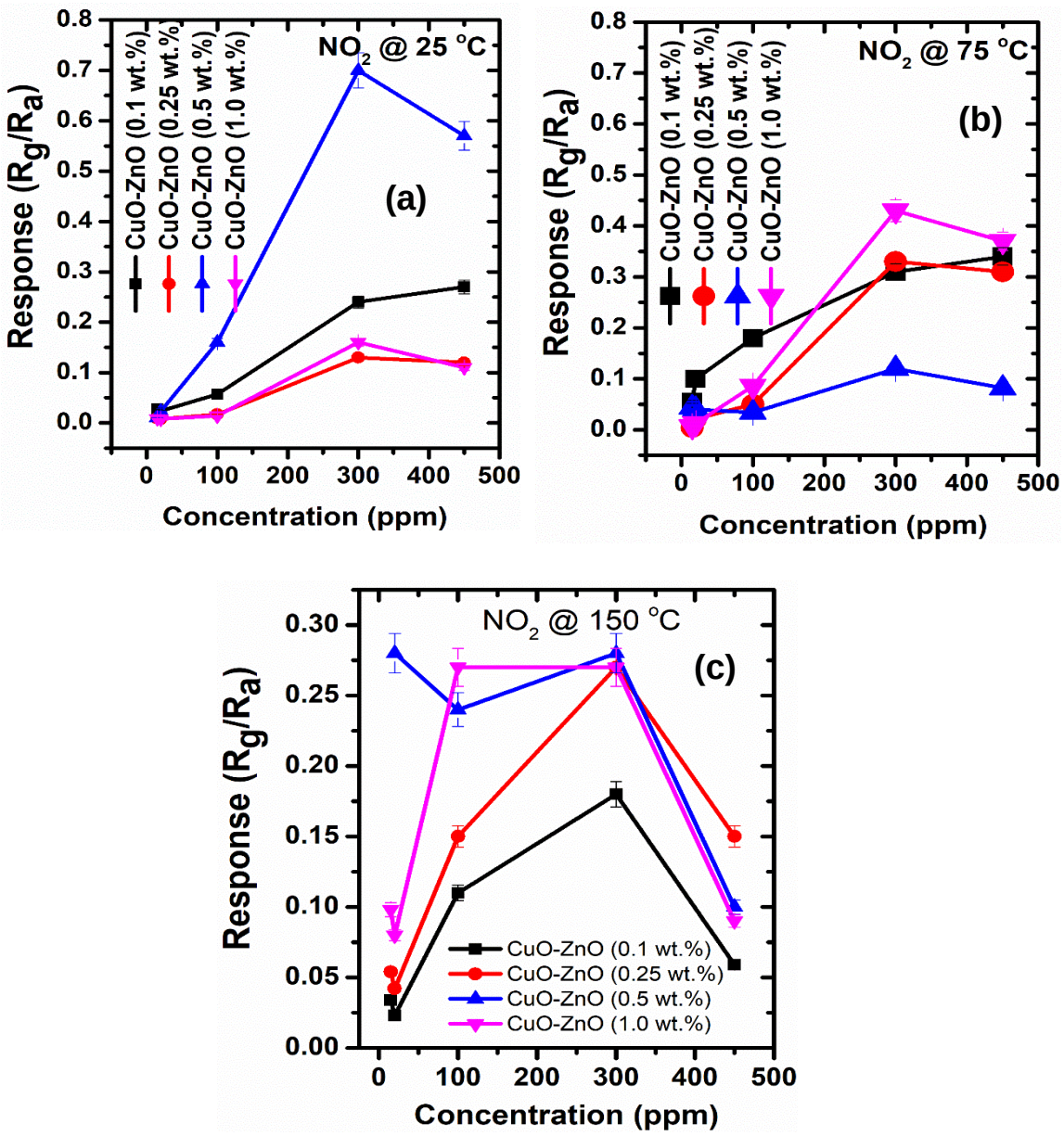

Figure 5.9: Response versus gas concentrations of CuO-ZnO (a) 25 °C and (b) 75 °C and (c) 150 °C, respectively.

Table 5.3 shows a comparison of the current work and that in the literature. In terms of performance, our sensor shows comparably good response and recovery times. Besides, most of the sensors show responses at higher operational temperatures in comparison to our current study.

Table 5.3: Summary of various sensors in the literature used to detect nitrogen oxide.

Sensing element	Concentration (ppm)	T_{res}/T_{rec} (s)	Response	Temp. (°C)	Refs.
CuO-ZnO (0.5 wt. %)	**100 300**	**40/120 45/133**	**0.16 0.7**	**25**	**This work**
SnO_2 nanotubes	100	1.33/22.6	15.2	25	**[56]**
SnO_2–$BiVO_4$ composite	0.1	13/9		25	**[57]**
p-type NiO nanoparticle	60	122	<60	75	**[58]**
MoS_2 NW network	5	25/150	7	100	**[59]**
$Ti_3C_2Tx@TiO_2@MoS_2$	50	1.8/70	55.1	25	**[60]**
MoS2/Ti3C2Tx	20	525/155	40.1	25	**[61]**

Figure 5.10 shows the radar selectivity of the various sensors tested towards six gases. It is clear that the current sensor has proper selectivity, where only minimal cross-sensitivity is observed for toluene. Our future work will focus on study the long-term stability towards NO_2 in various conditions.

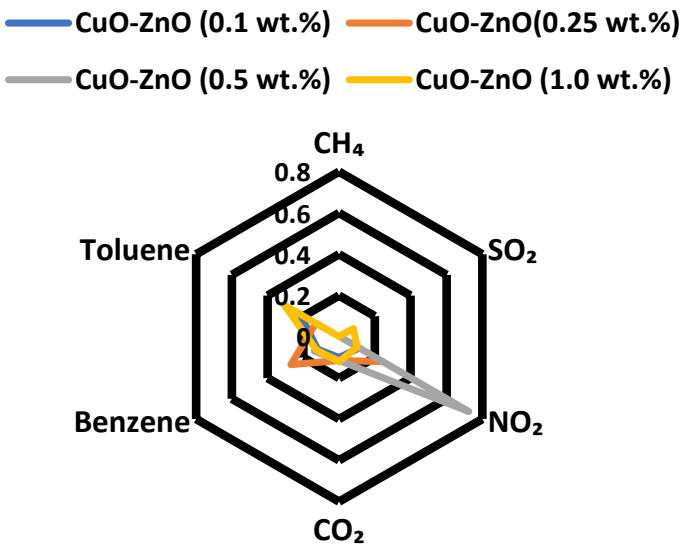

Figure 5.10: Selectivity radar plot of the various sensors tested to several toxic gases.

Furthermore, it is well known that the mechanism of the gas sensing is associated to redox reaction between the adsorbed oxygen species and the analyte gas. Therefore, we performed XPS analyses on the CuO-ZnO (1.0 wt. %) heterostructure, including its counterparts' materials. The survey spectra of CuO-ZnO heterostructures shown in **Appendix A4: a** confirm the existence of Cu, O, Zn and C elements. **Figure 5.11** demonstrates high resolution of Cu2p, which illustrates the binding energies of Cu $2p_{1/2}$ and Cu $2p_{3/2}$ at 953.4 eV and 933.4 eV respectively, which are comparable to the typical peaks of Cu^{2+} and established the presence of CuO **[62, 63]**. Clearly, the incorporation of ZnO did not much alter the peaks of CuO, instead the CuO-ZnO heterostructure formed as validated by the Zn2p peaks of ZnO on the supporting information, **Appendix A4: b**.

Generally, the asymmetric O 1s peaks may be assigned to three distinctive peaks, such as lattice oxygen (O_L), O^{2-} in CuO or ZnO, oxygen vacancies (V_O), and chemisorbed oxygen species (O_C), which correspond to binding energies of 529.9 eV, 530.5 eV, 531.8 eV, and 532 eV, respectively **[63-65]**. As depicted in **Figure 5.11**, other samples could only be fitted into three peaks, while the CuO-ZnO (1.0 wt. %) sample could be fitted into four peaks centered at 529.4, 530.5, 531.8 and 533.3 eV, which could be due to degree of lattice mismatch at the CuO and ZnO interface **[66]**, leading to increased V_O and the observed peak at 533 eV. Thus, this peak (at 533 eV) could be associated with O_C. The degree of lattice mismatch regulates the V_O content. In **Table A1**, the V_O concentration in the CuO-ZnO (1.0 wt.%) heterostructure was as high as 54.2 %, indicating more adsorbed oxygen species participate in the gas sensing reaction. This correlates well with XRD findings. Generally, the V_O content is valuable to yield additional energetic surface sites and creates extra negatively charge oxygen species on the surface that are valuable for enhanced sensing properties.

Nonetheless, the O_L are considered as low-active oxygen species that do not play any role in gas sensing reactions, hence poor sensing performance is observed for samples with higher amount of O_L. Whereas the O_C are strongly vigorously involved in the redox reactions with the gas molecule adsorbed on the sensing materials. These findings coincided well with the gas sensing characteristics and established the viability of fabricating CuO-ZnO (1.0 wt. %), heterostructure to realize admirable gas sensing performance as further observed in **Appendix A5**, demonstrating a clear correlation between the gas sensing and V_O/O_L ratio.

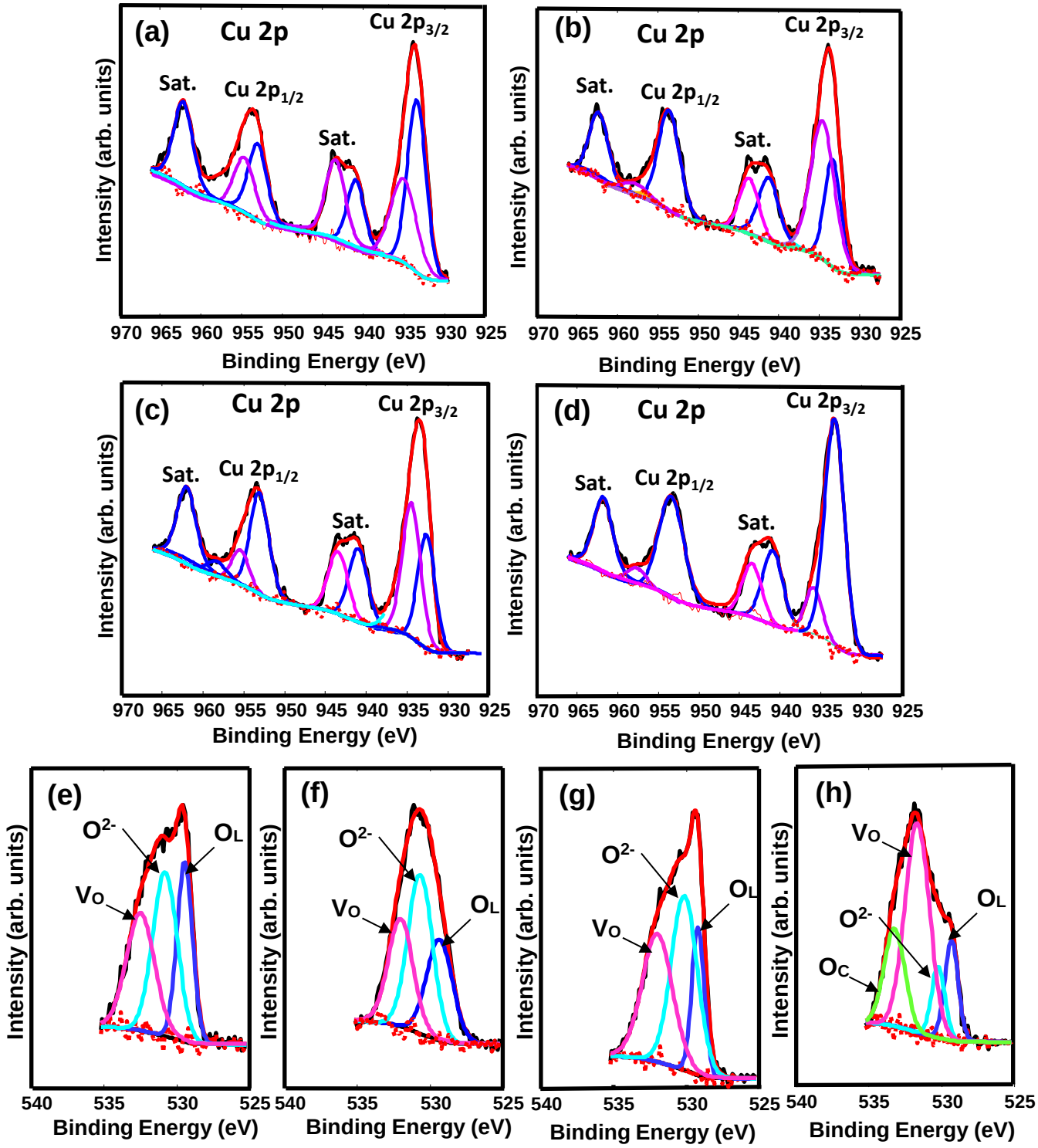

Figure 5.11: (a and b) Cu2p XPS spectra of (a) CuO-ZnO (0.1 wt. %), b) CuO-ZnO (0.25 wt. %), (c) CuO-ZnO (0.5 wt. %), (d) CuO-ZnO (1.0 wt. %). O 1s XPS spectra of (e) CuO-ZnO (0.1 wt. %), (f) CuO-ZnO (0.25 wt. %), (g) CuO-ZnO (0.5 wt. %), (h) CuO-ZnO (1.0 wt. %).

REFERENCES

1. WHO, Household Air Pollution and Health, 2018 (accessed on the 18th of July 2022).

2. E.M. Alsbou, K.W. Omari, BTEX indoor air characteristic values in rural areas of Jordan: Heaters and health risk assessment consequences in winter season, Environmental Pollution 267 (2020) pp. 115-464. https://doi.org/10.1016/j.envpol.2020.115464.

3. E. Gallego, X. Roca, J.F. Perales, X. Guardino, Determining indoor air quality and identifying the origin of odour episodes in indoor environments, J. Environ. Sci. 21 (2009) pp. 333-339. https://doi.org/10.1016/S1001-0742(08)62273-1.

4. S.-W. Choi, J. Zhang, K. Akash, S.S. Kim, H_2S sensing performance of electrospun CuO-loaded SnO_2 nanofibers, Sens. Actuators B Chem. 169 (2012) pp. 54–60. https://doi.org/10.1016/j.snb.2012.02.054.

5. G. Yurko, J. Roostaei, T. Dittrich, L. Xu, M., Ewing, Y. Zhang, G. Shreve, Realtime sensor response characteristics of 3 commercial metal oxide sensors for detection of BTEX and chlorinated aliphatic hydrocarbon organic vapors. Chemosensors 7, (2019) pp. 40. DOI:10.3390/chemosensors7030040.

6. R. Nasreddine, V. Person, C.A. Serra, S. Le Calve. Development of a novel portable miniaturized GC for near real-time low level detection of BTEX. Sensor. Actuator. B Chem. 224 (2016) pp. 159-169. https://doi.org/10.1016/j.snb.2015.09.077.

7. F. Li, S. Guo, J. Shen, L. Shen, D. Sun, B. Wang, Y. Chen, S. Ruan, Xylene gas sensor based on Au-loaded $WO_3 \cdot H_2O$ nanocubes with enhanced sensing

performance Sensors and Actuators B 238 (2017) pp. 364–373. http://dx.doi.org/10.1016/j.snb.2016.07.021.

8. H.-S. Woo, C.-H. Kwak, J.-H. Chung, J.-H. Lee, Co-Doped Branched ZnO Nanowires for Ultraselective and Sensitive Detection of Xylene, ACS Appl. Mater. Interfaces 6 (2014) pp. 22553−22560, http://dx.doi.org/10.1021/am506674u

9. Y. Cao, P. Hu, W. Pan, Y. Huang, D. Ji, Methanal and xylene sensors based on ZnO nanoparticles and nanorods prepared by room-temperature solid-state chemical reaction, Sensors and Actuators B 134 (2008) pp. 462–466. http://doi:10.1016/j.snb.2008.05.026.

10. A. Mirzaei, J.-H. Kim, H.W. Kim, S.S. Kim, Resistive-based gas sensors for detection of benzene, toluene and xylene (BTX) gases: a review, J. Mater. Chem. C, 6 (2018) pp. 4342-4370. https://doi.org/10.1039/C8TC00245B.

11. W. Xu, M. Li, R. Jiang, L. Zhang, M. Du, S. Wang, J. Cao, Facile synthesis of discus-like porous CuO architectures and their enhanced xylene gas sensing performances, Materials Letters 324 (2022) pp. 132-657. https://doi.org/10.1016/j.matlet.2022.132657.

12. C. Wang, S. Zhang, L. Qiu, S.A. Rasaki, F. Qu, T. Thomas, Y. Liu, M. Yang, Ru-decorated WO_3 nanosheets for efficient xylene gas sensing application, Journal of Alloys and Compounds 826 (2020) pp. 154-196. https://doi.org/10.1016/j.jallcom.2020.154196.

13. J. Guo, Y. Li, B. Jiang, H. Gao, T. Wang, P. Sun, F. Liu, Xu Yan, X. Liang, Y. Gao, J. Zhao, G. Lu, Xylene gas sensing properties of hydrothermal synthesized SnO_2-Co_3O_4 microstructure, Sensors & Actuators: B. Chemical 310 (2020) pp. 127-780. https://doi.org/10.1016/j.snb.2020.127780.

14. H. Wang, M. Chen, Q. Rong, Y. Zhang, J. Hu, D. Zhang, S. Zhou, X. Zhao, J. Zhang, Z. Zhu, Q. Liu, Ultrasensitive xylene gas sensor based on flower-like SnO_2/Co_3O4 nanorods composites prepared by facile two-step synthesis method, Nanotechnology 31 (2020) 255501 (13pp). https://doi.org/10.1088/1361-6528/ab70d1.

15. J.-H. Kim, H.-M. Jeong, C.W. Na, J.-W. Yoon, F. Abdel-Hady, A.A. Wazzan, J.-H. Lee, Highly selective and sensitive xylene sensors using Cr_2O_3-$ZnCr_2O_4$ hetero-nanostructures prepared by galvanic replacement, Sensors and Actuators B 235 (2016) pp. 498–506. http://dx.doi.org/10.1016/j.snb.2016.05.104.

16. J.F. Chan, J.K. Jeon, Y.K. Moon, J.-H. Lee, Highly sensitive xylene sensors using Fe_2O_3-$ZnFe_2O_4$ composite spheres, Journal of Sensor Science and Technology Vol. 30, No. 4 (2021) pp. 191-195. http://dx.doi.org/10.46670/JSST.2021.30.4.191.

17. H. Gao, J. Guo, Y. Li, C. Xie, X. Li, L. Liu, Y. Chen, P. Sun, F. Liu, X. Yan, F. Liu, G. Lu, Highly selective and sensitive xylene gas sensor fabricated from NiO/ $NiCr_2O_4$ p-p nanoparticles, Sensors & Actuators: B. Chemical 284 (2019) pp. 305–315. https://doi.org/10.1016/j.snb.2018.12.152.

18. M. Li, W. Xu, R. Jiang, M. Du, L. Zhang, S. Yang, S. Wang, J. Cao, Colloids and Surfaces A: Physicochemical and Engineering Aspects 649 (2022) pp. 129-522. https://doi.org/10.1016/j.colsurfa.2022.129522.

19. X.-T. Xue, L.-Y. Zhu, K.-P. Yuan, C. Zeng, X.-X. Li, H.-P. Ma, H.-L. Lu, D.W. Zhang, ZnO branched p-CuxO@n-ZnO heterojunction nanowires for improving acetone gas sensing performance, Sensors and Actuators: B. Chemical 324 (2020) pp. 128-729. https://doi.org/10.1016/j.snb.2020.128729.

20. D.R. Miller, S.A. Akbar, P.A. Morris, Nanoscale metal oxide-based heterojunctions for gas sensing: a review, Sens. Actuators B, 204 (2014) pp. 250-272. https://doi.org/10.1016/j.snb.2014.07.074.

21. V.S. Kamble, R.K. Zemase, R.H. Gupta, B.D. Aghav, S.A. Shaikh, J.M. Pawara, S.K. Patil, S.T. Salunkh, Improved toxic NO_2 gas sensing response of Cu-doped ZnO thin-film sensors derived by simple co-precipitation route. Optical Materials 131 (2022) pp. 112-706. https://doi.org/10.1016/j.optmat.2022.112706.

22. F. Kheiri, V. Soleimanian, M. Ghasemi, A. Mokhtari, The microstructure, optical and gas sensing properties of bilayer TiO_2/ZnO systems in terms of annealing temperature, Mater. Sci. Semicond. Process. 121 (2021) pp. 105-462. https://doi.org/10.1016/j.mssp.2020.105462.

23. N. Jamalpoor, M. Ghasemi, V. Soleimanian, Investigation of the role of deposition rate on optical, microstructure and ethanol sensing characteristics of nanostructured Sn doped In_2O_3 films, Mater. Res. Bull. 106 (2018) pp. 49–56. https://doi.org/10.1016/j.materresbull.2018.05.028.

24. R.N. Mariammal, K. Ramachandran, Study on gas sensing mechanism in p-CuO/n-ZnO heterojunction sensor, Materials Research Bulletin 100 (2018) pp. 420–428. https://doi.org/10.1016/j.materresbull.2017.12.046.

25. R.G. Motsoeneng, I. Kortidis, R. Rikhotso, H.C. Swart, S.S. Ray, D.E. Motaung, Temperature-dependent response to C_3H_7OH and C_2H_5OH vapors induced by deposition of Au nanoparticles on SnO_2/NiO hollow sphere-based conductometric sensors, Sensors and Actuators B: Chemical 316 (2020) pp. 128-041. https://doi.org/10.1016/j.snb.2020.128041.

26. H.R. Yang, X.J. Bai, P. Hao, J. Tian, Y.Y. Bo, X.Z. Wang, H. Liu, A simple gas sensor based on zinc ferrite hollow spheres: highly sensitivity, excellent selectivity and

long-term stability, Sens. Actuators B Chem. 280 (2019) pp. 34-40. https://doi.org/10.1016/j.snb.2018.10.056.

27. X.W. Li, X. Zhou, H. Guo, C. Wang, J.Y. Liu, P. Sun, F.M. Liu, G.Y. Lu, Design of Au@ZnO yolk-shell nanospheres with enhanced gas sensing properties, ACS Appl. Mater. Interfaces 6 (2014) pp. 18661–18667. https://dx.doi.org/10.1021/am5057322.

28. K. Xu, J.P. Zou, S.Q. Tian, Y. Yang, F.Y. Zeng, T. Yu, Y.T. Zhang, X.M. Jie, C. L. Yuan, Single-crystalline porous nanosheets assembled hierarchical Co_3O_4 microspheres for enhanced gas-sensing properties to trace xylene, Sens. Actuators B Chem. 246 (2017) pp. 68–77. https://doi.org/10.1016/j.snb.2017.02.071.

29. H. Gao, J. Guo, Y. Li, C. Xie, X. Li, L. Liu, Y. Chen, P. Sun, F. Liu, X. Yan, F. Liu, G. Lu, Highly selective and sensitive xylene gas sensor fabricated from NiO/$NiCr_2O_4$ p-p nanoparticles, Sensors & Actuators: B. Chemical 284 (2019) pp. 305–315. https://doi.org/10.1016/j.snb.2018.12.152.

30. C. Sun, X. Su, F. Xiao, C. Niu, J. Wang, Synthesis of nearly monodisperse Co_3O_4 nanocubes via a microwave-assisted solvothermal process and their gas sensing properties, Sensors and Actuators B: Chemical, 157 (2011) pp. 681-685. https://doi.org/10.1016/j.snb.2011.05.039.

31. C.Q. Ge, C.S. Xie, S.Z. Cai, Preparation and gas-sensing properties of Ce-doped ZnO thin-film sensors by dip-coating, Mater. Sci. Eng. B, 137 (2007) pp. 53-58 06. https://doi:10.1016/j.mseb.2006.10.006.

32. G. A. Russell, the Rates of Oxidation of Aralkyl Hydrocarbons. Polar Effects in Free Radical Reactions. J. Am. Chem. Soc. 78 (1956) pp. 1047−1054. https://pubs.acs.org/doi/pdf/10.1021/ja01586a047.

33. Z.P. Tshabalala, T.P. Mokoena, K.T. Hillie, H.C. Swart, D.E. Motaung, Improved BTEX gas sensing characteristics of thermally treated TiO_2 hierarchical

spheres manifested by high-energy {001} crystal facets, Sensors and Actuators B: Chemical, 338 (2021) pp. 129-774. https://doi.org/10.1016/j.snb.2021.129774.

34. P.C. Nam, V.V. Quan, N.M. Thong, P.T.T. Thao, Bond dissociation enthalpies in benzene derivatives and effect of substituents: an overview of density functional theory (B3LYP) based computational approach, Vietnam J. Chem., 55 (6) (2017) pp. 679-691, International Edition. https://doi.org/10.15625/2525-2321.2017-00527.

35. J M. Szwarc, The C - C bond energy in ethylbenzene, J. Chem. Phys., 17 (1949) pp. 431-435. https://doi.org/10.1063/1.1747283.

36. L.B. Deng, X.H. Ding, D.W. Zeng, S.P. Zhang, C.S. Xie, High sensitivity and selectivity of C-doped gas sensors toward toluene and xylene, IEEE Sens. J., 12 (2012) pp. 2209-2214. 10.1109/JSEN.2011.2179980.

37. D.L. Baulch, C.T. Bowman, C.J. Cobos, R.A. Cox, T. Just, J.A. Kerr, M.J. Pilling, D. Stocker, J. Troe, W. Tsang, R.W. Walker, J. Warnatz, Evaluated kinetic data for combustion modeling: supplement II, J. Phys. Chem. Ref. Data, 34 (2005) pp. 757-1397. https://doi.org/10.1063/1.1748524.

38. M.E. Franke, T.J. Koplin, U. Simon, Metal and metal oxide nanoparticles in chemiresistors: does the nanoscale matter, Small 2 (2006) pp. 36–50. https://doi.org/10.1002/smll.200500261.

39. K. Dutta, P. P. Chattopadhyay, C. W. Lu, M. S. Ho and P. Bhattacharyya, A highly sensitive BTX sensor based on electrochemically derived wall connected TiO_2 nanotubes, Appl. Surf. Sci., 354 (2015) pp. 353-361. https://doi.org/10.1016/j.apsusc.2015.05.077.

40. Y. Xiao, L. Lu, A. Zhang, Y. Zhang, L. Sun, L. Huo, F. Li, Highly Enhanced Acetone Sensing Performances of Porous and Single Crystalline ZnO Nanosheets: High Percentage of Exposed (100) Facets Working Together with Surface Modification

with Pd Nanoparticles, ACS Appl. Mater. Interfaces 4 (2012) pp. 3797−3804. https://dx.doi.org/10.1021/am3010303.

41. M. Breedon, M.J.S. Spencer, I. Yarovsky, Adsorption of NO_2 on Oxygen Deficient ZnO ($2\bar{1}\bar{1}0$) for Gas Sensing Applications: A DFT Study, J. Phys. Chem. C 114 (2011) pp. 16603- 16610. https://doi.org/10.1021/jp105733p.

42. Z. Lin, M. Xu, P. Fu, Q. Deng, Crystal plane control of 3D iron molybdate and the facet effect on gas sensing performances, Sensors and Actuators B: Chemical, 254 (2018) pp. 755-762. https://doi.org/10.1016/j.snb.2017.07.101.

43. T.L.H. Doan, J.-Y. Kim, J.-H. Lee, L.H. Thuy Nguyen, H.T. Thu Nguyen, A.T. Thanh Pham, T.B. Nguyen Le, A. Mirzaei, T.B. Phan, S.S. Kim, Facile synthesis of metal-organic framework-derived ZnO/CuO nanocomposites for highly sensitive and selective H_2S gas sensing, Sensors and Actuators: B. Chemical 349 (2021) pp. 130-741. https://doi.org/10.1016/j.snb.2021.130741.

44. J.-H. Lee, J.-Y. Kim, J.-H. Kim, A. Mirzaei, H.W. Kim, S.S. Kim, Co3O4-loaded ZnO nanofibers for excellent hydrogen sensing, Int. J. Hydrog. Energy 44 (2019) pp. 27499–27510, https://doi.org/10.1016/j.ijhydene.2019.08.226.

45. A. Katoch, S.-W. Choi, J.-H. Kim, J.H. Lee, J.-S. Lee, S.S. Kim, Importance of the nanograin size on the H2S-sensing properties of ZnO–CuO composite nanofibers, Sens. Actuators B: Chem. 214 (2015) pp. 111–116, https://doi.org/10.1016/j.snb.2015.03.012.

46. Y. Lin, C. Norman, D. Srivastava, F. Azough, L. Wang, M. Robbins, K. Simpson, R. Freer, I.A. Kinloch, Thermoelectric power generation from lanthanum strontium titanium oxide at room temperature through the addition of graphene, ACS Appl. Mater. Interfaces 7 (2015) pp. 15898–15908, https://doi.org/10.1021/ acsami.5b03522.

47. C.H. Feng, Z.W. Jiang, J.X. Wu, B. Chen, G.Y. Lu, C.Z. Huang, Pt-Cr_2O_3-WO_3 composite nanofibers as gas sensors for ultra-high sensitive and selective xylene detection, Sens. Actuators B 300 (2019) pp. 127-008. https://doi.org/10.1016/j.snb.2019.127008.

48. Z.P. Tshabalala, T.P. Mokoena, M. Jozela, J. Tshilongo, T. Hillie, H.C. Swart, D.E. Motaung, TiO_2 Nanowires for Humidity-Stable Gas Sensors for Toluene and Xylene. ACS Applied Nano Materials 4 (2021) pp. 702-716. https://doi.org/10.1021/acsanm.0c02963.

49. T. Akiyama, Y. Ishikawa, K. Hara, Xylene sensor using double-layered thin film and Ni-deposited porous alumina, Sens. Actuators B 181 (2013) pp. 348–352. https://doi.org/10.1016/j.snb.2013.01.024.

50. H.P. Wang, M.P. Chen, Q. Rong, Y.M. Zhang, J.C. Hu, D.M. Zhang, S.Q. Zhou, X. B. Zhao, J. Zhang, Z.Q. Zhu, Q.J. Liu, Ultrasensitive xylene gas sensor based on flower-like SnO_2/Co_3O_4 nanorods composites prepared by facile two-step synthesis method, Nanotechnology, 31 (2020), pp. 255-501. https://doi.org/10.1088/1361-6528/ab70d1.

51. H.Y. Gao, J. Guo, Y.W. Li, C.L. Xie, X. Li, L. Liu, Y. Chen, P. Sun, F.M. Liu, X. Yan, F. M. Liu, G.Y. Lu, Highly selective and sensitive xylene gas sensor fabricated from NiO/$NiCr_2O_4$ p-p nanoparticles, Sens. Actuators B 284 (2019) pp. 305–315. https://doi.org/10.1016/j.snb.2018.12.152.

52. H.Y. Gao, D.D. Wei, P.F. Lin, C. Liu, P. Sun, K. Shimanoe, N. Yamazoe, G.Y. Lu, The design of excellent xylene gas sensor using Sn-doped NiO hierarchical nanostructure, Sens. Actuators B 253 (2017) pp. 1152-1162. https://doi.org/10.1016/j.snb.2017.06.177.

53. J. Guo, Y.W. Li, B. Jiang, H.Y. Gao, T.S. Wang, P. Sun, F.M. Liu, X. Yan, X.S. Liang, Y. Gao, J. Zhao, G.Y. Lu, Xylene gas sensing properties of hydrothermal synthesized SnO2-Co_3O_4 microstructure, Sens. Actuators B 310 (2020), pp. 127-780. https://doi.org/10.1016/j.snb.2020.127780.

54. Y. Shi, T. Liu, Y. Zhao, J. Su, S. Zeb, Y. Nie , C. Qin, B. Wang, X. Jiang, Tunable oxygen vacancies of cobalt oxides for efficient gas sensing application, Sensors and Actuators: B. Chemical 350 (2022) pp. 130-860. https://doi.org/10.1016/j.snb.2021.130860.

55. O. Mnethu, S.S. Nkosi, I. Kortidis, D.E. Motaung, R.E. Kroon, H.C. Swart, N.G. Ntsasa, J. Tshilongo, T. Moyo, Ultra-sensitive and selective p-xylene gas sensor at low operating temperature utilizing Zn doped CuO nanoplatelets: Insignificant vestiges of oxygen vacancies, Journal of Colloids and Interface Science, 576 (2020) pp. 364-375. https://doi.org/10.1016/j.jcis.2020.05.030.

56. L. Teng, Y. Liu, M. Ikram, Z. Liu, M. Ullah, L. Ma, X. Zhang, H. Wu, L. Li, K. Shi. One-step synthesis of palladium oxide-functionalized tin dioxide nanotubes: Characterization and high nitrogen dioxide gas sensing performance at room temperature. Journal of Colloid and Interface Science 537 (2019) pp. 79–90. https://doi.org/10.1016/j.jcis.2018.11.001.

57. Z. Zhu, Z.-X. Chiang, R.-J. Wu, U. Kumar, C.-H. Wu. A combined experimental and theoretical study of composite SnO_2–$BiVO_4$ for selective NO_2 sensing. Materials Chemistry and Physics 292 (2022) pp. 126-868. https://doi.org/10.1016/j.matchemphys.2022.126868.

58. T.P. Mokoena, H.C. Swart, K.T. Hillie, Z.P. Tshabalala, M. Jozela, J. Tshilongo, DE. Motaung. Enhanced propanol gas sensing performance of p-type NiO gas sensor

induced by exceptionally large surface area and crystallinity. Applied Surface Science 571 (2022) pp. 151-121. https://doi.org/10.1016/j.apsusc.2021.151121.

59. R. Kumar, N. Goel, M. Kumar, High performance NO_2 sensor using MoS2 nanowires network, Appl. Phys. Lett. 112 (2018) pp. 53-502. https://doi.org/10.1063/1.5019296.

60. Z. Liu, H. Lv, Y. Xie, J. Wang, J. Fan, B. Sun, L. Jiang, Y. Zhang, R. Wang, K. Shi, A, 2D/2D/2D $Ti_3C_2Tx@TiO_2@MoS_2$ heterostructure as an ultrafast and high sensitivity NO_2 gas sensor at room-temperature, J. Mater. Chem. A. (2022). https://doi.org/10.1039/D1TA09369J.

61. Qui Thanh Hoai Ta, Nguyen Ngoc Tri, Jin-Seo Noh. Improved NO_2 gas sensing performance of 2D MoS_2/Ti_3C_2Tx MXene nanocomposite. Applied Surface Science 604 (2022) pp. 154-624. https://doi.org/10.1016/j.apsusc.2022.154624.

62. H. Fang, S. Li, H. Zhao, J. Deng, D. Wang, J. Li, Enhanced NO_2 gas sensing performance by hierarchical $CuO–Co_3O_4$ spheres, Sensors and Actuators: B. Chemical, 352 (2022) pp. 131-068. https://doi.org/10.1016/j.snb.2021.131068.

63. D.N. Oosthuizen, I. Kortidis, H.C. Swart, D.E. Motaung, Facile control of room temperature nitrogen dioxide gas selectivity induced by copper oxide nanoplatelets, Journal of colloid and interface science, 560 (2020) pp. 755-768. https://doi.org/10.1016/j.jcis.2019.10.036.

64. A. Katoch, S.W. Choi, J.H. Kim, J.H. Lee, J.S. Lee, S.S. Kim, Importance of the nanograin size on the H_2S-sensing properties of ZnO-CuO composite nanofibers, Sens. Actuators B: Chem 214 (2015) pp. 111–116.https://doi.org/10.1016/j.snb.2015.03.012.

65. X.H. Yang, H.T. Fu, Y. Tian, Q. Xie, S.X. Xiong, D.Z. Han, et al., Au decorated In2O3 hollow nanospheres: a novel sensing material toward amine, Sens. Actuators B: Chem 296 (2019) pp. 126696. https://doi.org/10.1016/j.snb.2019.126696.

66. M. Al-Hashem, S. Akbar, P. Morris. Role of oxygen vacancies in nanostructured metal-oxide gas sensors: a review, Sens. Actuator B: Chem 301 (2019) pp. 24. https://doi.org/10.1016/j.snb.2019.126845.

CHAPTER SIX

Summary

In summary, n-type ZnO and p-type CuO nanostructures were successfully synthesized utilizing various bases. SEM images demonstrated that ZnO-NaOH, ZnO-NH_4OH, and ZnO-urea, were made of rods and nanoplatelets that were directed radially outwards displaying a tetragonal shape with sharp/pointy tops and nanoplates, which were randomly arranged to form a spherical shape, respectively. The CuO-NaOH, ZnO-NH_4OH, and CuO-urea were made of nanorods, which are arranged randomly, irregular shaped with nanoplatelets, showing an almost uniform shape and hollow sphere-like shape that are built up of hierarchical arrangements, respectively. While the ZnO-KOH and CuO-KOH displayed nanoplatelets like structures. The XRD confirmed the pure phases of ZnO and CuO, respectively and their crystalline sizes increased based on the reduction in the strength of the base (i.e., NaOH > NH_4OH > urea). While that of ZnO-KOH showed higher crystalline sizes in comparison to other bases. ZnO-NaOH demonstrated a superior response among the tested sensors, displaying a dual-mode temperature selectivity towards benzene and xylene at effective temperatures of 75 and 150 °C, respectively. Additionally, the sensor displayed excellent sensitivity and a low theoretical LoD of 18 ppb, which was related to higher V_O observed in the *in-situ* PL and EPR analyses. While the p-type CuO based sensors displayed low response, sensitivity and selectivity towards BTEX, including ethanol and NO_2. The XPS analyses also confirmed that the ZnO-NaOH possessed higher V_O, which contributed to higher sensing performance. Moreover, the ZnO-NaOH sensor, which was stored for 36 months under ambient conditions, revealed

reliable repeatability and long-term operation stability of 22 hour exposure to xylene. Temperature modulated-dual selectivity for the detection of benzene and xylene is an attractive approach for indoor air quality monitoring.

The xylene sensor was successfully fabricated with CuO-ZnO heterostructures as sensing materials. The CuO-ZnO (1.0 wt. %) based sensor demonstrated superior selectivity towards 100 ppm of xylene at 100 °C. Furthermore, insignificant cross-sensitivity towards toluene, benzene and other interference gases was witnessed. An ultra-low LOD of 9.5 ppb and higher sensitivity of 0.063 ppm^{-1} were observed towards xylene vapour, which showed that the CuO-ZnO (1.0 wt. %) heterostructure-based sensor can achieve sub-ppb-level xylene concentration, which basically shows extended detection range of 9.5 ppb-100 ppm. The improved performance of the sensor to xylene can be linked to:

(1) The addition of ZnO in CuO-ZnO heterostructure, which had a significant influence on the dislocation density, lattice strain, as well as on crystalline size, resulted in improved surface defects (i.e., V_O). Therefore, superior sensing performance of CuO-ZnO (1.0 wt. %) heterostructure based sensor could be anticipated.

(2) The reduced band gap, which provides more xylene adsorption sites and makes it easier for xylene to capture electrons in the conduction band.

(3) A higher number of heterojunctions for the CuO-ZnO (1.0 wt. %.), compared to those with lower ZnO wt. %. led to more p-n heterojunctions, and as a result, enhanced sensing response was observed.

(4) The robust chemical affinity and catalytic performance of p-type CuO on xylene vapour.

Moreover, the long-term stability test disclosed that the CuO-ZnO (1.0 wt. %) sensor is very stable towards 100 ppm xylene in dry and under 40% RH. Thus, this approach offers an active way for fabricating a highly sensitive and selective xylene based derived from CuO-ZnO (1.0 wt. %) heterostructure-based sensor for indoor xylene detection.

For detection of NO_2, the sensors showed a room temperature gas sensing performance. Additionally, with respect to other gases, the sensor could not respond at room temperature. While at higher temperatures, the sensors showed better selectivity towards xylene. Thus, these findings showed that while the sensors could detect xylene at high temperatures, nonetheless, the room temperature sensitivity of the CuO-ZnO (0.5 wt. %)-based sensor towards NO_2 denoted that the sensor could be used for low power consumption.

Future work will focus on incorporation of CuO on ZnO matrix and the possible loading of noble metals on the CuO-ZnO and ZnO-CuO surface. The samples will be further tested towards various analytes at various operational temperatures.

APPENDIX SECTION

Appendix A related to Chapter 5:

LOW-OPERATIONAL TEMPERATURE FOR SELECTIVE DETECTION OF XYLENE AND NO_2 GASES USING A p-n CuO-ZnO HETEROSTRUCTURE-BASED SENSOR

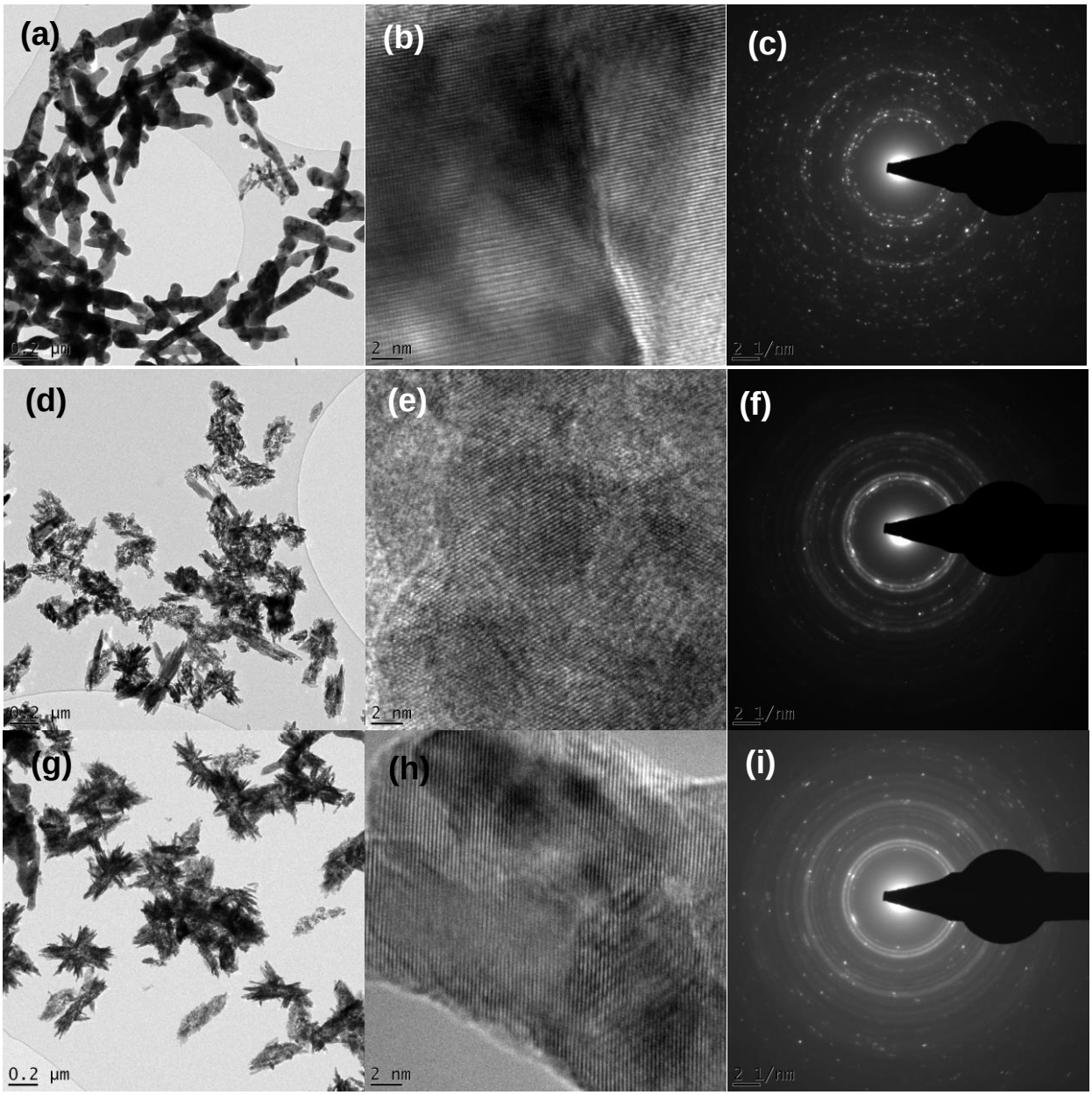

Appendix A1: Low- and high-resolution TEM images of (a-b) CuO-ZnO (0.1 wt. %), (d-e) CuO-ZnO (0.1 wt. %), (g-h) CuO-ZnO (0.1 wt. %). Note that (c, f and i) correspond to SAED patterns.

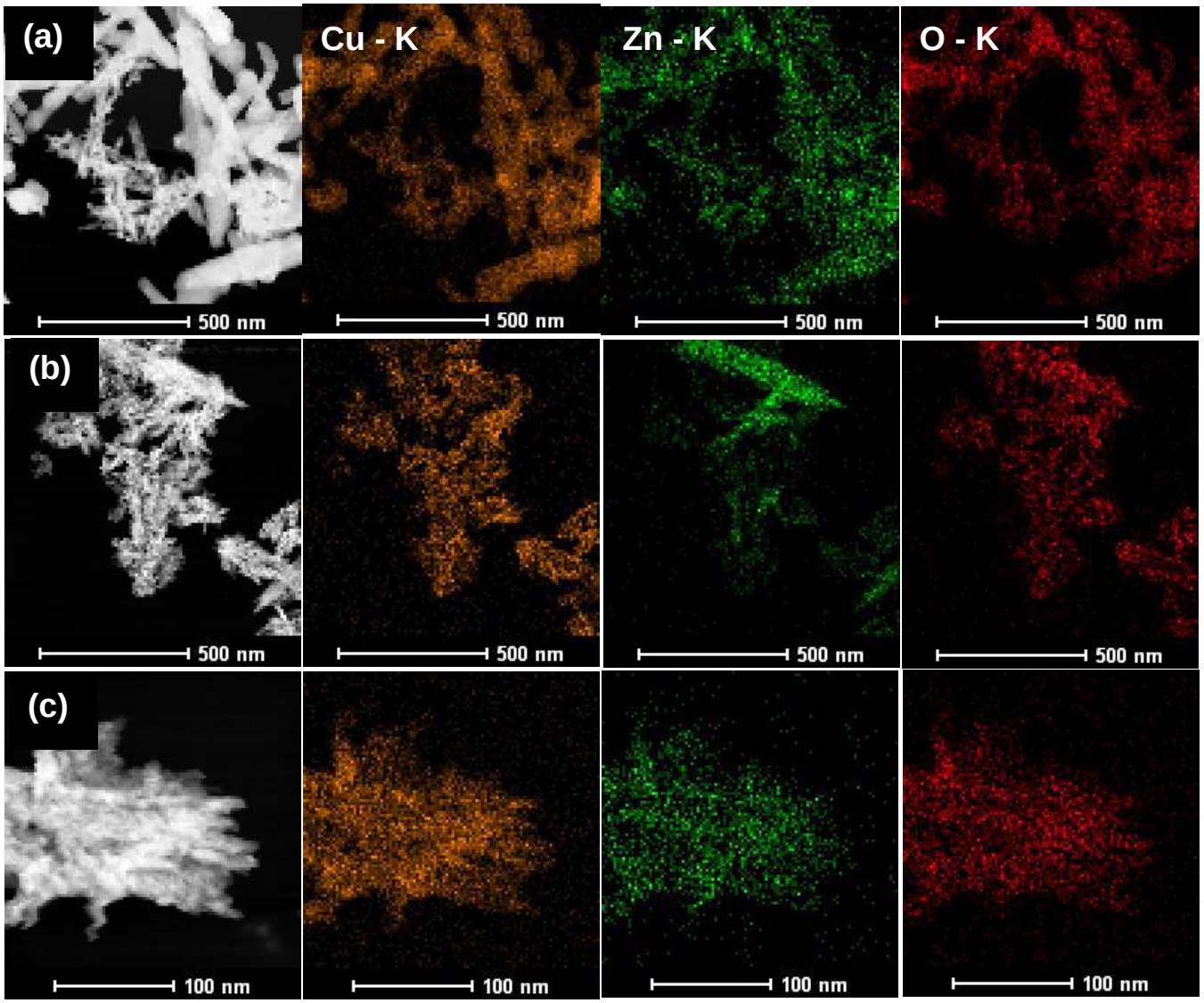

Appendix A2: (a) STEM- EDS SI maps of (a) CuO-ZnO (0.1 wt. %), (b) CuO-ZnO (0.25 wt. %), and (c) CuO-ZnO (0.5 wt. %).

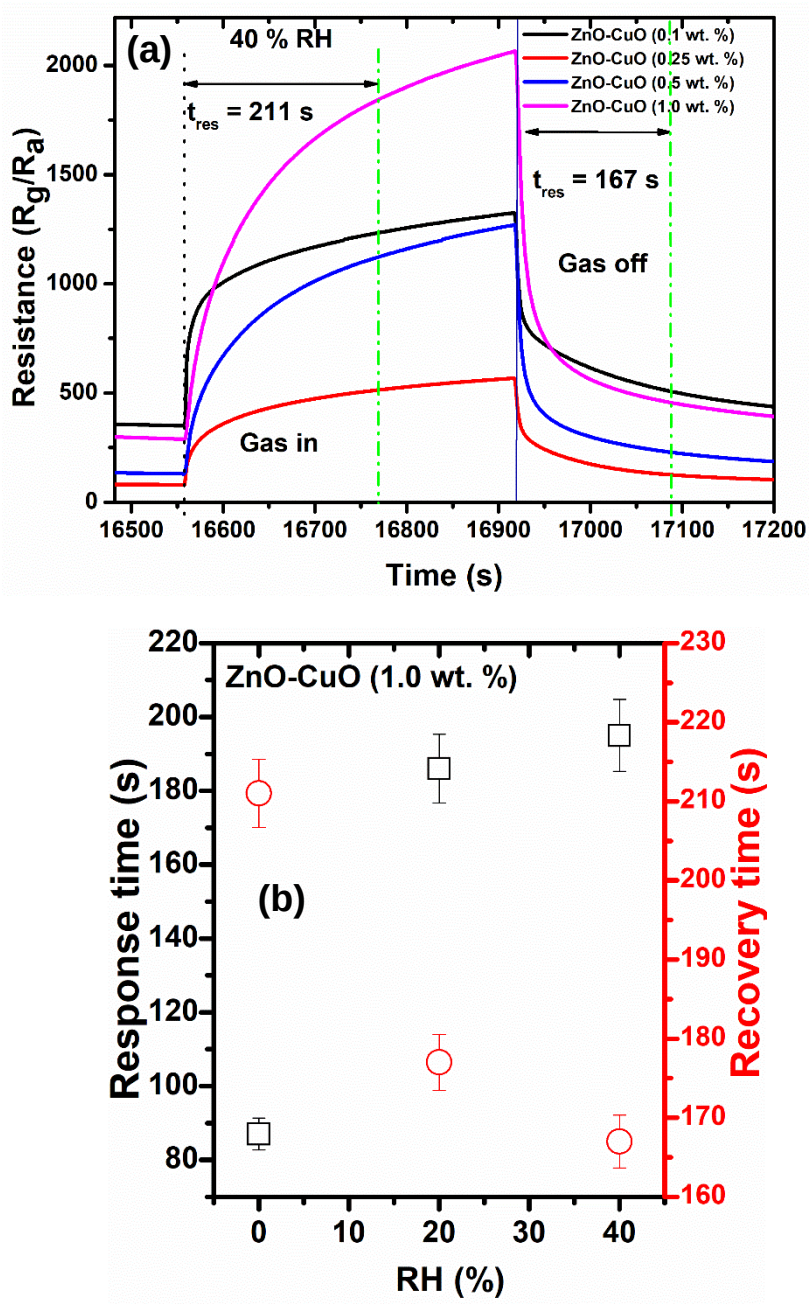

Appendix A3: Real-time resistance plot showing the response and recovery times of various CuO-ZnO nanostructures towards 100 ppm xylene under 40% RH, and (b) response and recovery times versus RH percentage.

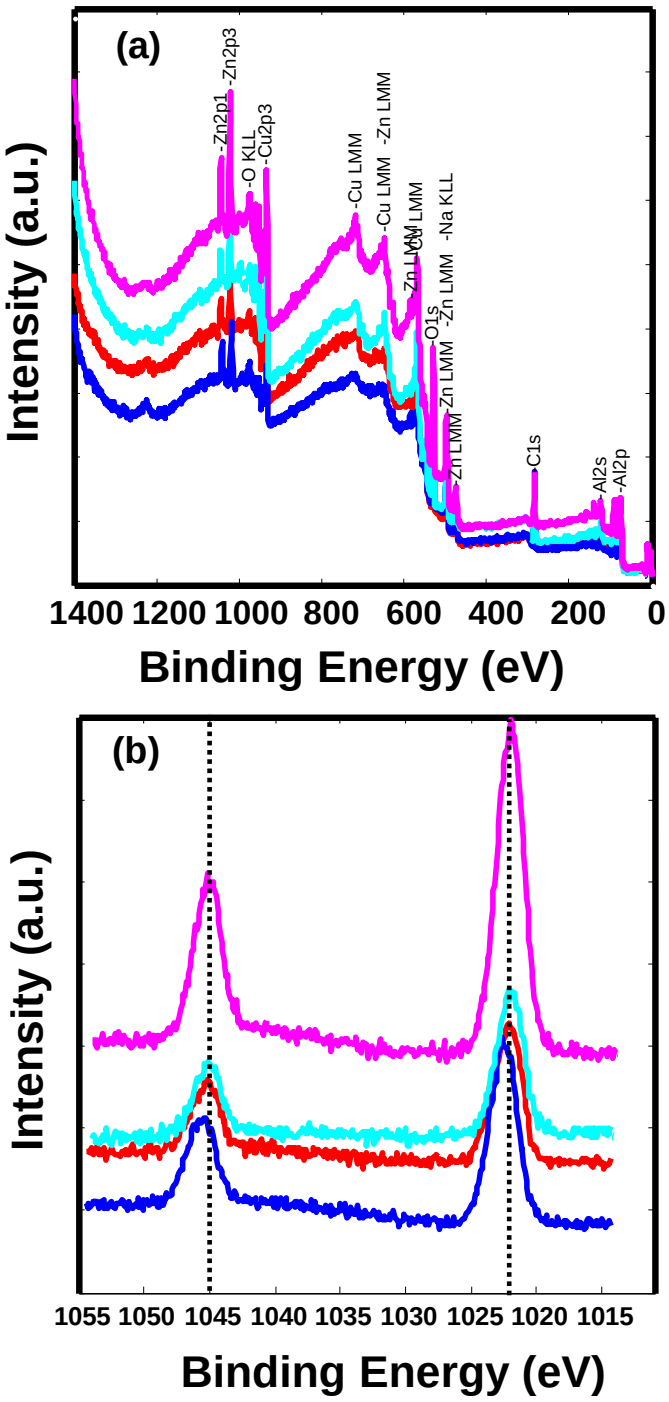

Appendix A4: (a) XPS survey spectra and (b) Zn2p spectra of various CuO-ZnO nanostructures. Note that red, blue, cyan, and magenta colours correspond to CuO-ZnO (0.1 wt. %) CuO-ZnO (0.25 wt. %) CuO-ZnO (0.5 wt. %) CuO-ZnO (1.0 wt. %), respectively.

Table A1: Summary of XPS O 1s peaks.

Samples	O 1s				
	529 eV	530 eV	531 eV	532 eV	533 eV
	O_L	O^{2-} in CuO	V_O		
CuO-ZnO (0.1 wt. %)	27.5	29.12	32.41		
CuO-ZnO (0.25 wt. %)	28.1	42.0	29.9		
CuO-ZnO (0.5 wt. %)	17.5	43.9	38.6		
CuO-ZnO (1.0 wt. %)	14.5	10.1	54.2	21.2	20.3

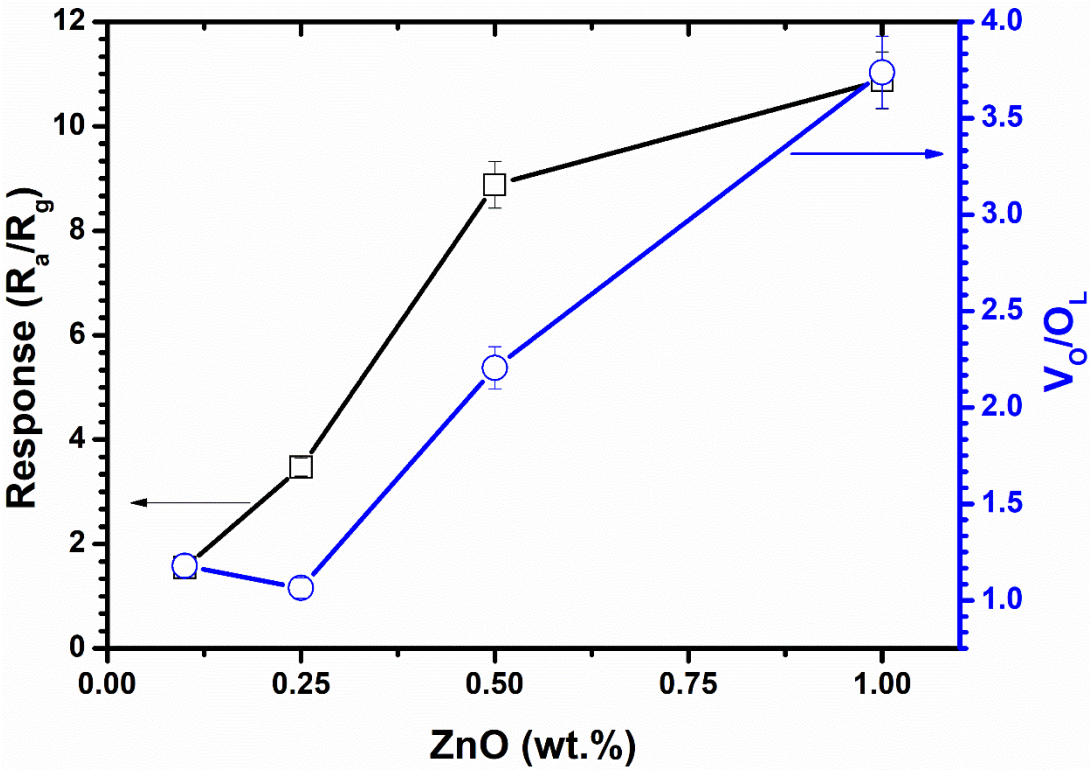

Appendix A5: Correlation between the responses of the sensors tested towards 100 ppm xylene and V_O/O_L ratio.